Delocalization transitions in disordered media

Spring, H.

DOI
10.4233/uuid:40f2a4ef-2080-4cb1-b14a-f0981aeb0cc9

Publication date
2023

Document Version
Final published version

Citation (APA)
Spring, H. (2023). *Delocalization transitions in disordered media*. [Dissertation (TU Delft), Delft University of Technology]. https://doi.org/10.4233/uuid:40f2a4ef-2080-4cb1-b14a-f0981aeb0cc9

DELOCALIZATION TRANSITIONS IN DISORDERED MEDIA

DELOCALIZATION TRANSITIONS IN DISORDERED MEDIA

Dissertation

for the purpose of obtaining the degree of doctor
at Delft University of Technology
by the authority of the Rector Magnificus prof. dr. ir. T.H.J.J. van der Hagen,
chair of the Board for Doctorates,
to be defended publicly on
Wednesday, 29 November 2023 at 10:00 o'clock

by

Hélène SPRING

Master of Science in Applied Physics, Delft University of Technology, the Netherlands
born in Châtel-Saint-Denis, Switzerland

This dissertation has been approved by the

promotor: Dr. A. R. Akhmerov
copromotor: Dr. M. T. Wimmer

Composition of the doctoral committee:

Rector Magnificus,	chairperson
Dr. A. R. Akhmerov	Delft University of Technology, promotor
Dr. M. T. Wimmer	Delft University of Technology, copromotor

Independent members:

Prof.dr. L. Kuipers	Delft University of Technology
Prof.dr. G. A. Steele	Delft University of Technology
Prof.dr. F. Hassler	RWTH Aachen University, Germany
Dr. J. van Wezel	University of Amsterdam, NL
Dr. T. van der Sar	Delft University of Technology, reserve member

This work was supported by the Netherlands Organization for Scientific Research (NWO/OCW) as part of an NWO VIDI grant 016.Vidi.189.180.

Printed by: Proefschriftenprinten.nl

Front & Back: *Untitled, Untitled*, Hélène Spring via Midjourney

ISBN 978-94-6366-771-5

An electronic version of this dissertation is available at
http://repository.tudelft.nl/.

CONTENTS

SUMMARY

The study of crystalline solids and condensed matter physics at large concerns itself with the new behaviors and phases of matter exhibited by elementary particles, atoms, and molecules by virtue of being assembled into a structure. These phases arise from complex microscopic behaviors, which makes it is difficult to establish rigorous quantitative models. The analysis of certain phases is greatly simplified in the presence of symmetries. These symmetries can be non-spatial (time-reversal, particle-hole) or spatial (rotation, inversion, reflection). For example, topological phases of matter are easily characterized and classified by the symmetries of the system. Symmetries constrain the band structure of a system, and as a result produce certain quantized responses, such as surface modes on an otherwise insulating bulk. Since these surface modes are related to the symmetry of the bulk, this phenomenon is known as bulk-edge correspondence. So long as the symmetries protecting the topological phase are respected and the energy gap of the insulating bulk remains open, bulk-edge correspondence persists in the presence of disorder. This disorder can be non-structural (applied magnetic field), involve part of the structure (impurities) or the entire structure, such as in amorphous systems.

Amorphous systems appear to possess no spatial symmetries, but they are isotropic on average: they possess average reflection and average continuous rotation symmetry. These average spatial symmetries protect topological phases. I present 2D and 3D amorphous systems that host topological insulator phases and have delocalized gapless edge modes on any surface orientation. Since the symmetries protecting the phase are only present on average, the topological phases are statistical topological insulator phases. I demonstrate this by presenting topological invariants and transport statistics consistent with statistical topological insulator phases.

In the same way that the presence or absence of a symmetry can alter the phase of matter hosted by a system, the presence or absence of energy conservation radically changes the physics of the system. For instance, systems that conserve energy obey the principle of near-sightedness, whereas systems that don't conserve energy, also known as non-Hermitian systems, do not. This principle dictates that a perturbation can only affect the electronic states in its vicinity, and states arbitrarily far from the perturbation are unaffected by it. The absence of this principle in non-Hermitian systems is exemplified by an extreme sensitivity to boundary conditions — the spectrum of a translationally invariant, periodic non-Hermitian system is completely different from the spectrum of the corresponding open system. In non-Hermitian systems with non-reciprocal hopping, all of the modes of the system localize at the system boundary (or boundaries). This was considered to be bulk-edge correspondence — a bulk property (non-reciprocal hopping) leads to a response at the system surface. However, since non-Hermitian systems are globally sensitive to local details, bulk-edge correspondence is not guaranteed to exist. I demonstrate this by showing that a single impurity with sufficiently large non-reciprocal hopping asymmetry is capable of attracting all of the modes of the system away from the

system boundary. Therefore, a bulk index cannot predict the position of the modes, which means there is no bulk-edge correspondence in the absence of translation invariance.

Further breaking translation invariance in non-Hermitian systems from a single impurity to disorder everywhere in the system, has an important impact on the system dynamics. In a clean non-Hermitian system, the various components of a wave packet injected into the system will be amplified or suppressed at rates that are determined by the imaginary parts of the corresponding eigenvalues, until the fastest-amplified component of that initial wave packet dominates. In a disordered non-Hermitian system, a wave packet scatters inelastically and acquires various new components. As the wave packet evolves, it is dominated by the component that is amplified the fastest. This process continues until the wave packet acquires the fastest amplified component possible in the system, and this state will dominate all future dynamics of the system. I demonstrate that this phenomenon leads to the existence of a transition between two propagating phases that is unique to non-Hermitian dynamics, and which is only realizable in the presence of disorder.

SAMENVATTING

Het onderzoek naar kristallijne vaste stoffen en de natuurkunde van gecondenseerde materie richt zich op nieuwe gedragingen en fasen van materie die worden tentoongesteld door elementaire deeltjes, atomen en moleculen doordat ze worden samengevoegd tot een structuur. Deze fasen ontstaan uit complexe microscopische behandelingen, wat het moeilijk maakt om systematische kwantitatieve modellen te creëren. De analyse van bepaalde fasen wordt sterk vereenvoudigd in aanwezigheid van symmetrieën. Deze symmetrieën kunnen niet-ruimtelijk zijn (tijdsomkering, deeltje-gat) of ruimtelijk (rotatie, inversie, reflectie). Bijvoorbeeld, topologische fasen worden gemakkelijk gekenmerkt en geclassificeerd door de symmetrieën van het systeem. Symmetrieën beperken de bandstructuur van een systeem en leiden daardoor tot bepaalde gekwantiseerde consequenties, zoals oppervlaktemodi op een verder isolerende bulk. Aangezien deze oppervlaktemodi gerelateerd zijn aan de symmetrie van de bulk, staat dit fenomeen bekend als bulk-rand correspondentie. Zolang de symmetrieën die de topologische fase beschermen worden gerespecteerd en de energiekloof van de isolerende bulk open blijft, blijft de bulk-rand correspondentie bestaan in aanwezigheid van wanorde. Deze wanorde kan niet-structureel zijn (aangelegd magnetisch veld), betrekking hebben op een deel van de structuur (onzuiverheden) of de gehele structuur betreffen, zoals bij amorfe systemen.

Amorfe systemen lijken geen ruimtelijke symmetrieën te hebben, maar ze zijn gemiddeld isotroop: ze hebben gemiddelde reflectie- en gemiddelde continue rotatiesymmetrie. Deze gemiddelde ruimtelijke symmetrieën beschermen topologische fasen. Ik presenteer 2D- en 3D-amorfe systemen die topologische isolerende fasen herbergen en gedelokaliseerde energie continue randmodi hebben voor elke oppervlakteoriëntatie. Omdat de symmetrieën die de fase beschermen alleen gemiddeld aanwezig zijn, zijn de topologische fasen statistische topologische isolatorfasen. Ik toon dit aan door topologische invarianten en transportstatistieken te presenteren die consistent zijn met statistische topologische isolatorfasen.

Op dezelfde manier waarop de aanwezigheid of afwezigheid van een symmetrie de fase van materie in een systeem kan veranderen, verandert de aanwezigheid of afwezigheid van energiebehoud radicaal de natuurkunde van een systeem. Bijvoorbeeld, systemen met energiebehoud volgen het principe van kortzichtigheid, terwijl systemen die geen energie behouden, ook wel bekend als niet-Hermitische systemen, dat niet doen. Dit principe betekent dat een verstoring alleen de elektronische toestanden in de nabijheid ervan kan beïnvloeden, en toestanden die zich willekeurig ver van de verstoring bevinden, niet beïnvloed worden. De afwezigheid van dit principe in niet-Hermitische systemen wordt geïllustreerd door een extreme gevoeligheid voor randvoorwaarden - het spectrum van een translationeel invariabel, periodiek niet-Hermitisch systeem is volledig verschillend van het spectrum van het overeenkomstige open systeem. In niet-Hermitische systemen met niet-wederzijdig gelijke overgangen lokaliseren alle modi van het systeem zich aan de systeemgrens (of systeemgrenzen). Dit werd beschouwd als bulk-

rand correspondentie - een bulk eigenschap (niet-wederzijdig gelijke overgangen) leidt tot een reactie aan het oppervlak van het systeem. Echter, aangezien niet-Hermitische systemen overal gevoelig zijn voor lokale details, is bulk-rand correspondentie niet gegarandeerd om te bestaan. Ik toon dit aan door te laten zien dat een enkele onzuiverheid met voldoende grote asymmetrie in niet-wederzijdig gelijke overgangen in staat is om alle modi van het systeem weg te trekken van de systeemgrens. Daarom kan een bulk-index de positie van de modi niet voorspellen, wat betekent dat er geen bulk-rand correspondentie is in de afwezigheid van translationele invariant.

Het verder verbreken van translationeel invariant in niet-Hermitische systemen, van een enkele onzuiverheid tot wanorde overal in het systeem, heeft een belangrijke invloed op de systeemdynamiek. In een schoon niet-Hermitisch systeem zullen de verschillende componenten van een golfpakket dat in het systeem wordt geïnjecteerd, worden versterkt of onderdrukt met snelheden die worden bepaald door de imaginaire delen van de overeenkomstige eigenwaarden, totdat de snelst versterkte component van dat initiële golfpakket domineert. In een verstoord niet-Hermitisch systeem verspreidt een golfpakket onelastisch en verkrijgt het verschillende nieuwe componenten. Naarmate het golfpakket evolueert, wordt het gedomineerd door de component die het snelst wordt versterkt. Dit proces gaat door totdat het golfpakket de snelst versterkte componenten die mogelijk zijn in het systeem heeft, en deze staat zal alle toekomstige dynamiek van het systeem domineren. Ik toon aan dat dit fenomeen leidt tot het bestaan van een overgang tussen twee voortplantende fasen die uniek zijn voor niet-Hermitische dynamica, en die alleen realiseerbaar is in aanwezigheid van wanorde.

1

INTRODUCTION

1

1.1. PREFACE

An object in motion will remain unchanged if no force acts on it — this is a well-known law of classical physics. It is true even for very small objects, like a single electron propagating in a vacuum. Applying a force to a moving electron may redirect, accelerate or stop it. If the applied force is a random time-dependent force, the electron reacts by diffusing in a random walk. So long as the diffusing electron retains a finite velocity, it will eventually travel arbitrarily far from its starting point.

The situation changes if the electron propagates in a crystalline solid instead of a vacuum. In crystals, quantum mechanical effects become important and a purely classical description of electron motion is insufficient. The initial picture is the same: if a crystal is disordered, the disorder acts like a random force and makes the electron scatter and diffuse. However, quantum mechanical interference between the different electron trajectories can inhibit the electron from travelling arbitrarily far. If the disorder in the crystal is sufficiently strong, the electron wave function may become completely localized to a certain region of the material — this phenomenon is known as Anderson localization [1, 2]. In one- and two-dimensional systems, even a small amount of disorder may localize the electron. In higher dimensions electrons may take many different paths through a material and thus are able to resist localization for weak enough disorder, but as disorder strength increases, eventually all electron wave functions become localized.

However, particle excitations in solids do not always have to localize in the presence of disorder. Crystalline solids tend to be symmetric: along with translation invariance by lattice vectors, they may have reflection planes or discrete rotation axes that leave the structure invariant. The symmetries of the system may protect symmetry-protected topological insulator phases. Topological insulators in dimension 2 and higher are characterized by surface channels in which excitations are able to travel ballistically. If disorder in the crystal does not break the symmetries protecting the topological phase or close the energy gap in the bulk of the crystal, then it cannot localize the excitations propagating in the surface channels.

Another mechanism by which electronic states overcome Anderson localization is the creation of a preferred transmission direction in systems that allow amplification and suppression. Energy can be injected into these systems, which makes states delocalize and overcome the disorder potentials in the system. As long as a sufficient amount of energy is provided to the system, the modes of the system resist localization from disorder of an arbitrary magnitude.

These two cases, in which transport persists in the presence of disorder, are the main subjects of this thesis. I present topological phases where symmetries protect propagating modes from localization. Rather than considering disorder which leaves the relevant symmetries intact, I present systems where disorder breaks these symmetries locally, but leave the system ensemble invariant. The topological protection of these symmetries is weakened, but excitations still resist localization on average — some disorder configurations will localize the modes, and some allow the particles to be perfectly transmitted. I then present systems where the injection of energy delocalizes all of the modes of the system. Since these systems do not conserve energy, the dynamics of the particles in the system have unique characteristics that go beyond traditional quantum mechanics.

1.2. TOPOLOGY AND SYMMETRIES

1.2.1. TOPOLOGICAL PHASES OF MATTER

The term 'phase of matter' brings to mind the different forms in which matter can exist, like solids, liquids, gases and plasmas. These phases are distinguished by their properties (such as density and structure), and a phase transition (melting, boiling etc.) is required to move between them. Similarly, topological phases of matter are differentiated by their properties and separated by phase transitions. Topological phases are characterized by quantized observables - some output of the system, be it a current or the winding of an electronic phase, only takes integer values. These integers are known as topological invariants because they can only change at the phase transition point, and different topological phases are identified by different values of this invariant. Topological phases of matter arise from the collective behavior of electrons in a solid, and this outwardly simple behavior is the result of a complex set of interactions. This section serves as an introduction of topological phases, how they are created and what their characteristics are.

A clue as to why topological phases produce quantized observables with fixed values is in their namesake. Topology is a branch of mathematics, which studies the properties of shapes and spaces that remain unchanged under continuous deformations such as stretching, bending, or twisting, but not tearing or gluing. The classic example of a continuous deformation is a donut being deformed into a mug. The donut cannot be deformed into a mug with two handles, without an additional hole being punched into it - these two objects are therefore not connected by a continuous deformation. Applying this to condensed matter systems, the electronic band structure can be thought of as a 'shape' that electrons occupy. Systems with different band structure shapes that cannot be continuously deformed into each other constitute different topological phases. A vacuum is the simplest topological phase, because it has no energy bands. Any observable of the system will be 0, any way you look at it (no current, no phase winding, etc.), so the topological invariant characterizing this phase is 0. This phase is referred to as the trivial insulator phase.

The vacuum is continuously connected to an atomic insulator whose valence band is fully occupied and whose conduction band is empty, and therefore they are topologically equivalent. Upon closing the bulk gap, the shape of the band structure is allowed to change and undergo a topological phase transition. This is due to the possibility of valence and conduction bands hybridizing when the gap closes, known as a band inversion. When a band inversion occurs, the coupling between the bands may lead to the re-formation of a gap and a topological phase transition. A topological phase transition separates phases with different topological characteristics - it corresponds to a 'tearing or gluing' non-continuous change. During this phase transition the band topology changes, and a trivial insulating state becomes a topological insulator or vice-versa. A topological insulator differentiates itself from a trivial insulator by the presence of surface states that cannot be removed as long as the bulk gap remains open.

A well-known example of a topological phase is the Chern insulator, also known as the quantum anomalous Hall phase. This phase shares some similarities with the integer quantum Hall effect (IQHE) but arises without an external magnetic field. Similarly to the IQHE, the Chern insulator has unidirectionally propagating, or chiral, modes at its edges,

shown schematically in Fig. 1.1 (a). The number of chiral modes at the edge only changes when the bulk gap closes. An invariant quantity of the Chern insulator is therefore the number of chiral modes at the edge of the system, known as the Chern number C. The topological invariant, a quantized observable of the system, is the Hall conductivity σ_{xy}, which is proportional to the Chern number, $\sigma_{xy} = e^2/hC$ (e is the elementary charge and h is the Planck constant). A trivial Chern number $C = 0$ therefore results in $\sigma_{xy} = 0$. The energies of the edge modes lie within the bulk energy gap: disorder that preserves the gap cannot couple the edge states to bulk states and localize them. Therefore the edge states are protected from localization due to the topology of the energy bands; this phenomenon is known as topological protection. Topologically protected edge modes remain robust against disorder and scattering, so long as the gap remains open.

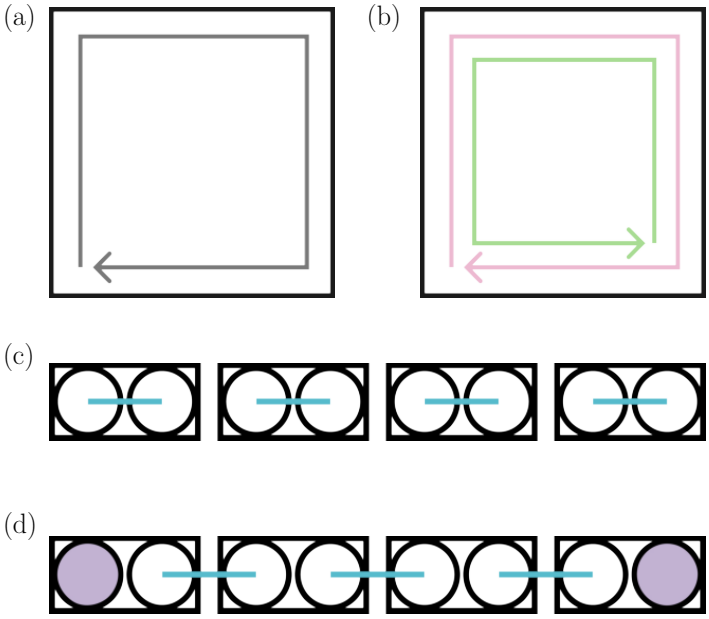

Figuur 1.1: Visualization of the effect of symmetry on topological phases. (a) Schematic of the Chern insulator (black square) with a single protected chiral edge mode circulating (gray arrow). (b) Schematic of the quantum spin Hall insulator (black square) with a single pair of counter-propagating edge spin channels. Different colors indicate different spin species. (c)-(d) Coupling of neighboring Majorana states (particle-hole symmetry case) or lattice sites (chiral symmetry case) which produce (c) a trivial insulator (d) a topological insulator with zero-energy states (in purple).

1.2.2. TOPOLOGICAL CLASSIFICATION

Topological phases manifest independently of symmetries, as exemplified by the Chern insulator. However, topological phases are characterized by the shape of their band structure, which are in turn constrained by symmetries. The presence or absence of symmetries therefore leads to the existence of different topological phases. Therefore, in addition to their topological invariants, topological phases can be classified and identified

by the symmetries that leave them invariant. Moreover, the formulation of the topological invariant of a symmetry-protected topological phase is informed by its symmetries, as bulk invariants are most simply expressed in terms of these symmetries [3].

The spatial symmetries of a lattice are the simplest to visualize: these are the reflection through a plane, the inversion around a point, and the rotation around an axis. Beyond spatial symmetries, a system is time-reversal symmetric if the dynamics of the system are the same whether time goes forwards or backwards. Time-reversal also reverses the direction of pseudo-vectors such as spins. Because of this, in time-reversal invariant materials, states must come in pairs of opposite momentum and spin orientation. The action of the unitary part of the time-reversal operator $U_{\mathcal{T}}$ on a Bloch Hamiltonian $H(k)$, with k the crystal momentum, is:

$$U_{\mathcal{T}} H^*(\mathbf{k}) U_{\mathcal{T}}^{-1} = H(-\mathbf{k}), \tag{1.1}$$

and when this operation leaves the Hamiltonian invariant, $H^*(-k) = H(k)$, the Hamiltonian is said to be time-reversal symmetric. Upon squaring $U_{\mathcal{T}}$, its diagonal elements are either all equal to 1 or to -1. In the latter case, each eigenvalue of the system is doubly degenerate, known as Kramers degeneracy [4]. The 2D Chern insulator discussed above clearly is not time-reversal symmetric, since its edge modes propagate in one direction: upon applying time-reversal, the modes propagate in the opposite direction and the system is equivalent to a Chern insulator with a Chern number of opposite sign. In order to obtain a time-reversal symmetric system, we consider two Chern insulators, with equal and opposite Chern numbers. This system is time-reversal symmetric, since reversing counter-propagating modes yields the same system. However, the total system has a total Chern number of 0, and so the system is trivial - in the presence of even mild disorder, electrons in one channel scatter into the counter-propagating channel, and the system localizes. In order to prevent the electrons from back-scattering, we can set one copy of the Chern insulator to only have spins of one type, and the other copy to only have spins of the opposite type. In this case, only magnetic impurities that can flip the sign of the spin can back-scatter the modes, which are forbidden in time-reversal symmetric systems. Now the system is time-reversal symmetric and corresponds to the quantum spin Hall topological phase, shown schematically in Fig. 1.1 (b) [5]. Unlike the Chern insulator, the edge modes do not carry a charge current, but instead carry a spin current.

Spatial and temporal symmetries act on particle position, momentum, and spin, but particles have more properties that are subject to reversal, such as electric charge. Particle-hole symmetry relates electron-like quasi-particles and electron vacancies or 'holes', which have equal and opposite charge. Specifically, the particle-hole operator reverses the momentum and spin of electrons while also changing their electric charge. In high-energy physics, this relates a particle to its anti-particle - for example, an electron propagating in a given direction is equivalent to a positron propagating in the opposite direction. In condensed matter systems, this symmetry requires the energies of particle-like states (above the Fermi level) to be mirrored by the corresponding hole-like states (below the Fermi level) with opposite crystal momentum k. The action of the unitary part of the particle-hole operator on a given Bloch Hamiltonian $H(k)$ is:

$$U_{\mathcal{P}} H^*(\mathbf{k}) U_{\mathcal{P}}^{-1} = -H(-\mathbf{k}). \tag{1.2}$$

Like $U_{\mathscr{T}}$, $U_{\mathscr{P}}$ also squares to either 1 or -1 [4]. Close to the $E = 0$ point, the band structure above the Fermi level has a predominantly electron-like character, and predominantly hole-like below the Fermi level. The $E = 0$ point is special because it requires the bands to have an equal superposition of electron-like and hole-like states, which is reminiscent of Bogoliubov quasi-particles in superconductors, also known as Majorana modes. Majorana modes are quasi-particles that are their own anti-particles, that appear in the presence of and are topologically protected by particle-hole symmetry. A widely discussed example of a system hosting Majorana modes is the Kitaev chain [6]. Simply put, the electron creation and annihilation operators can be written in terms of the Majorana operator, and an electron can therefore be viewed as a composite particle formed by two Majoranas. By tailoring the pairing of the Majoranas in a chain of electrons, the system is either made trivial (all states are electrons, no states at $E = 0$) or topological. This is illustrated in Fig. 1.1 (c) and (d), where rectangles represent electron states, and circles represent the Majorana states that compose each electron. When Majorana states are coupled as in Fig. 1.1 (d), two isolated Majoranas at $E = 0$ are located on either end of the chain. Since they are separated by a chain of unoccupied states, so long as the states are sufficiently spatially separated, they cannot hybridize to re-form an electron state.

The product of time-reversal symmetry and particle-hole symmetry in itself is a symmetry that can protect topological phases, in the absence of either individual symmetry that forms the product. This symmetry, known as chiral symmetry, is thus named because it is closely related to the concept of chirality, which refers to an asymmetry between an object and its mirror image. In condensed matter systems, chiral symmetry typically arises from the arrangement of atoms or molecules in the material's crystal lattice. Chiral symmetry is also known as sublattice symmetry, since a key example of this symmetry is a bi-atomic lattice composed of two identical lattices, with each sublattice hosting one type of atom. One key manifestation of chiral symmetry is the emergence of robust chiral edge states at the boundaries of the material. These chiral edge states propagate in a single direction along the edge of the material. The action of the unitary part of the chiral operator on a given Bloch Hamiltonian $H(k)$ is:

$$U_{\mathscr{C}} H(\mathbf{k}) U_{\mathscr{C}}^{-1} = -H(\mathbf{k}). \tag{1.3}$$

$U_{\mathscr{C}}$ only squares to 1 [4]. A chiral symmetric band structure is symmetric around the $E = 0$ line ($H(k) = -H(k)$) - this makes states at $E = 0$ special. A widely discussed example of a topological phase protected by chiral symmetry is the Su-Schrieffer-Heeger (SSH) chain [7]. Its working principle is similar to the Kitaev chain, but instead of coupling Majorana states, neighboring sites of the lattice are coupled with alternating strengths, similar to a dimerized polymer. The schematic of the SSH lattice is the same as for the Kitaev chain, shown in Fig. 1.1 (c) and (d), but here the rectangles represent a unit cell containing two atoms. When inter-unit cell coupling is strong and intra-unit cell is weak [Fig. 1.1 (c)], the system is trivial. In the opposite case [Fig. 1.1 (d)], the system enters a topological phase and zero energy states at the end of the chain appear.

Time-reversal, particle-hole, and chiral symmetry are used to define and categorize strong topological insulator phases into 10 different symmetry classes, based on all of the combinations of these symmetries, both the combinations of their presence and to what value their unitary parts square to [8, 9] [Table 1.1, Fig. 1.2].

Symmetry class	$\mathscr{T}$	$\mathscr{P}$	$\mathscr{C}$
A	0	0	0
AI	1	0	0
AII	-1	0	0
AIII	0	0	1
BDI	1	1	1
C	0	-1	0
CI	1	-1	1
CII	-1	-1	1
D	0	1	0
DIII	-1	1	0

Tabel 1.1: Symmetry classes and the symmetries they possess [8].

This classification reveals an underlying structure. The 'complex' classes A and AIII form an alternating pattern in dimension space, and the remaining 'real' classes are periodic in dimension with a period of 8 dimensions. The classification also reveals that for the 'real' classes, the number of values topological invariants can assume, either 2 (denoted by $\mathbb{Z}_2$), any integer ($\mathbb{Z}$), or any even integer ($2\mathbb{Z}$), depends on both the dimension and the symmetry class. Comparing neighboring columns of the table reveals that this dependence is related to a dimensional shift [4].

Spatial symmetries such as rotation, reflection or inversion are also capable of protecting and classifying topological phases, known as weak or crystalline topological phases [10–12]. The action of the unitary part of the reflection, inversion and rotation operators on a given Bloch Hamiltonian $H(k)$ is:

$$U_M H(\mathbf{k}) U_M^{-1} = H(R_M \cdot \mathbf{k}) \tag{1.4}$$

$$U_I H(\mathbf{k}) U_I^{-1} = H(-\mathbf{k}) \tag{1.5}$$

$$U(\phi) H(\mathbf{k}) U(\phi)^{-1} = H(R(\phi) \cdot \mathbf{k}) \tag{1.6}$$

where $R_{M_{\hat{\mathbf{n}}}} = \mathbb{1} - 2\hat{\mathbf{n}}\hat{\mathbf{n}}^T$ is the real space orthogonal action reversing the component in the $\hat{\mathbf{n}}$ direction, $U(\phi) = \exp\left(i\phi S_z\right)$, S_z is the onsite spin-z operator, and $R(\phi) = \exp\left(i\phi L_z\right)$, $L_z = \sigma_y$. A continuous, isotropic medium has the highest degree of spatial symmetry: continuous rotation symmetry around any axis and inversion or reflection along any axis. Condensed matter systems are composed of discretely spaced atoms, which reduces the degree of spatial symmetry. Crystals tend to be translationally invariant, typically are rotation-symmetric with a discrete angle of rotation, and commonly possess reflection axes. These symmetries refine the topological classification of strong topological insulators and modify or often simplify the formulation of the topological invariant [3].

1.2.3. BULK-EDGE CORRESPONDENCE

Topological phases are special because they are robust to disorder - as long as the bulk gap and system boundaries remain open, the surface modes of a topological phase cannot be removed or gapped out. This is due to the fact that the boundaries of a topological

	d												
Cartan	0	1	2	3	4	5	6	7	8	9	10	11	...
Complex case:													
A	$\mathbb{Z}$	0	$\mathbb{Z}$	0	$\mathbb{Z}$	0	$\mathbb{Z}$	0	$\mathbb{Z}$	0	$\mathbb{Z}$	0	...
AIII	0	$\mathbb{Z}$	0	$\mathbb{Z}$	0	$\mathbb{Z}$	0	$\mathbb{Z}$	0	$\mathbb{Z}$	0	$\mathbb{Z}$	...
Real case:													
AI	$\mathbb{Z}$	0	0	0	$2\mathbb{Z}$	0	$\mathbb{Z}_2$	$\mathbb{Z}_2$	$\mathbb{Z}$	0	0	0	...
BDI	$\mathbb{Z}_2$	$\mathbb{Z}$	0	0	0	$2\mathbb{Z}$	0	$\mathbb{Z}_2$	$\mathbb{Z}_2$	$\mathbb{Z}$	0	0	...
D	$\mathbb{Z}_2$	$\mathbb{Z}_2$	$\mathbb{Z}$	0	0	0	$2\mathbb{Z}$	0	$\mathbb{Z}_2$	$\mathbb{Z}_2$	$\mathbb{Z}$	0	...
DIII	0	$\mathbb{Z}_2$	$\mathbb{Z}_2$	$\mathbb{Z}$	0	0	0	$2\mathbb{Z}$	0	$\mathbb{Z}_2$	$\mathbb{Z}_2$	$\mathbb{Z}$	...
AII	$2\mathbb{Z}$	0	$\mathbb{Z}_2$	$\mathbb{Z}_2$	$\mathbb{Z}$	0	0	0	$2\mathbb{Z}$	0	$\mathbb{Z}_2$	$\mathbb{Z}_2$	...
CII	0	$2\mathbb{Z}$	0	$\mathbb{Z}_2$	$\mathbb{Z}_2$	$\mathbb{Z}$	0	0	0	$2\mathbb{Z}$	0	$\mathbb{Z}_2$	...
C	0	0	$2\mathbb{Z}$	0	$\mathbb{Z}_2$	$\mathbb{Z}_2$	$\mathbb{Z}$	0	0	0	$2\mathbb{Z}$	0	...
CI	0	0	0	$2\mathbb{Z}$	0	$\mathbb{Z}_2$	$\mathbb{Z}_2$	$\mathbb{Z}$	0	0	0	$2\mathbb{Z}$	...

Figuur 1.2: Classification of strong topological phases as a function of spatial dimension d and symmetry class. The entries of the table indicate whether the topological invariant can assume 2 values ($\mathbb{Z}$) or any number of integer values ($\mathbb{Z}$) A 0 entry denotes the case where the combination of dimension and symmetries yields a trivial phase. Table reproduced from [8].

material interface with a vacuum or with another material. At these interfaces, the topological invariant must either change to 0 or to another integer, which means the bulk gap has to close. Therefore, due to the topological properties of the bulk, modes must be present on the surface of topological insulators [13]. This phenomenon is known as bulk-edge correspondence (BEC), a fundamental principle stating that the bulk topological invariants determine the presence and properties of protected boundary states.

The surface states of crystalline topological insulators are present at every boundary that globally preserves the symmetry protecting the topological phase. However, topological surface states of a crystalline topological insulator are gapped out on surfaces that systematically break the spatial symmetries protecting the phase, e.g. on a crystal plane that is not a mirror-symmetric plane [Fig. 1.3].

When the entire system undergoes a topological phase transition, the bulk gap closes, and the system is said to be in its critical phase. In the critical phase, there is a finite density of states in the bulk, composed of either localized or delocalized modes, or a mix of the two. The bulk invariant no longer assumes quantized values at the critical point.

1.3. TOPOLOGY IN DISORDERED SYSTEMS

As simple or elegant the theoretical formulations of topological phases may be, synthesizing topological phases proves to be more challenging due to the presence of disorder. Taking the example of the Kitaev chain, there exist proposals to create it in heterostructures using two-dimensional electron gases [14], proximitized semiconductor nanowires [15–18], and in quantum dot arrays [19–23]. Due to disorder and/or distance dependence of the chemical potential, bound states appear that mimic certain effects of Majorana bound states [24–27]. These make the interpretation of experimental results difficult,

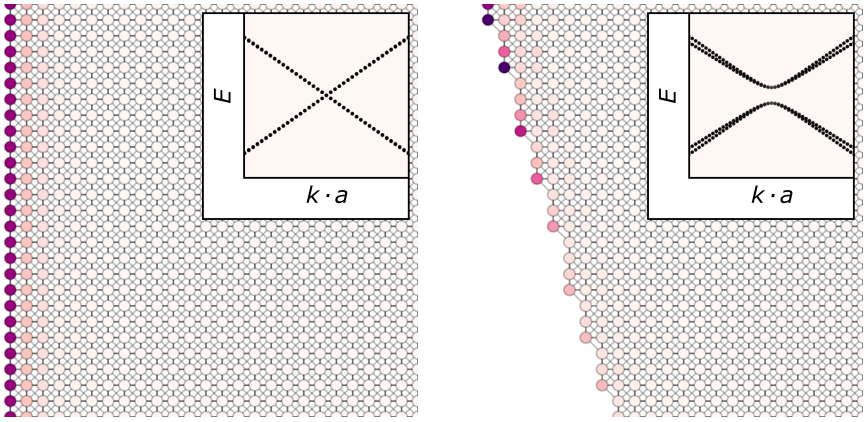

Figuur 1.3: Zero-energy local density of propagating modes in a crystal system; darker site color indicates higher density. Insets: boundary dispersion relation corresponding to straight and tilted edge terminations. Figure adapted from Chapter 2.

since certain experimental signatures of Majorana modes (in-gap state close to zero energy, non-local conductance) can be replicated with trivial states [28].

Despite these difficulties, not all disorder is capable of destroying topological phases. Strong topological insulators are agnostic to the details of the medium that do not affect the symmetries that protect them. For this reason, strong topological insulator phases are realizable even in the presence of maximal structural disorder, as in amorphous systems [29]. Widespread surface disorder that systematically violates non-spatial symmetries, such as magnetic fields or a distribution of magnetic impurities, may push the topological surface modes away from the surface into the bulk, but will not destroy them. The disorder must affect the entire bulk and therefore destroy the bulk topological phase, in order to remove the surface modes. Spatial symmetries are closely tied to the structural details of the lattice, and therefore crystalline topological phases are susceptible to structural disorder. Like strong topological phases, if the bulk of a crystalline topological insulator is free from disorder, boundary modes are likely to persist on planes that preserve the spatial symmetries protecting the topological phase.

While disorder is capable of breaking symmetries, it does not necessarily break average symmetries. For instance, a random magnetic field will locally break time-reversal symmetry, but when averaging over an entire system, time-reversal symmetry is present on average [30]. Average symmetries are capable of protecting topological phases [31]; however, the quality of the topological protection is modified. Disordered systems that support topological insulating phases with one or more average symmetries are called statistical topological insulators [30]. The surface modes of these systems behave like they would in a lower-dimensional critical topological phase. For 2D statistical topological insulators, this translates to bimodal behavior where a certain disorder configuration either yields perfect transmission or localization. Averaging over disorder configurations, the conductance scales as $1/\sqrt{L}$ as if the modes were propagating in a disordered, critical 1D chain [32, 33]. This is in contrast to the unit transmission of translationally-invariant

topological phases, independent of system size. The surface modes of 3D statistical topological insulators propagate as though they were in a 2D critical phase and the conductance on their surfaces scales like a 2D critical phase, and so on for higher dimensions [30].

The reason why statistical topological insulators bear similar transport characteristics to $d-1$-dimensional critical topological phases is because they inherit their topology from these phases [30]. The bulk invariant of a statistical topological insulator in a given symmetry class is constructed from the invariant of the $d-1$ topological phase in the same symmetry class. Therefore, if no $d-1$ topological phase exists in a given symmetry class, there will be no corresponding d-dimensional statistical topological insulator. Due to disorder, the invariants of statistical topological insulators are conjectured to be $\mathbb{Z}_2$ [30], in contrast to the invariants of systems without disorder [Fig. 1.2].

1.4. NON-HERMITIAN DELOCALIZATION

So far I have presented topological phases in systems where energy is conserved. However, realistic systems tend to have some degree of loss or dissipation. Despite the ubiquity of dissipation, relaxing the constraint of energy conservation has far-reaching consequences on the physics of the system. Systems that don't conserve energy are called non-Hermitian, and in this section I will define them, explain the link between non-Hermiticity and topology, and exposit their unique characteristics and responses.

1.4.1. NON-HERMITIAN SYSTEMS

In conventional quantum mechanics, Hamiltonians (which represent the energy operator of a quantum system) are typically Hermitian, meaning they are equal to their adjoint or Hermitian conjugate $H = H^\dagger$. Hermitian Hamiltonians have real eigenvalues [Fig. 1.4 (a)], which correspond to the energy levels of the system. Hermitian Hamiltonians also preserve the norm of the wave function, guaranteeing unitary time evolution and energy conservation.

Breaking the Hermiticity constraint $H \neq H^\dagger$ results in a non-Hermitian system. Energy conservation is no longer guaranteed, and therefore non-Hermitian operators typically describe systems that perform non-conservative processes, like gain and loss. Non-Hermitian Hamiltonians have complex eigenvalues, and their imaginary components determine the behavior of the corresponding eigenstate in the system. If a given eigenvalue has a positive imaginary component, the corresponding eigenstate will be amplified at a rate proportional to the magnitude of this imaginary part. Conversely, an eigenstate whose associated eigenvalue has a negative imaginary component will be suppressed.

At the quantum-mechanical level, non-Hermitian operators are typically only suitable for phenomenological descriptions of physical processes. This is because observables are given by Hermitian operators acting on the Hilbert space of the system, whose eigenvalues are real, and the time evolution of the system is unitary, preserving the probability density. By definition, the eigenvalues of non-Hermitian system are generically complex, its time evolution is not unitary, and therefore the measurement probabilities increase or decrease with time, which makes a physical interpretation difficult or even meaningless [34]. Physical implementations of non-Hermitian quantum mechanics are restricted to

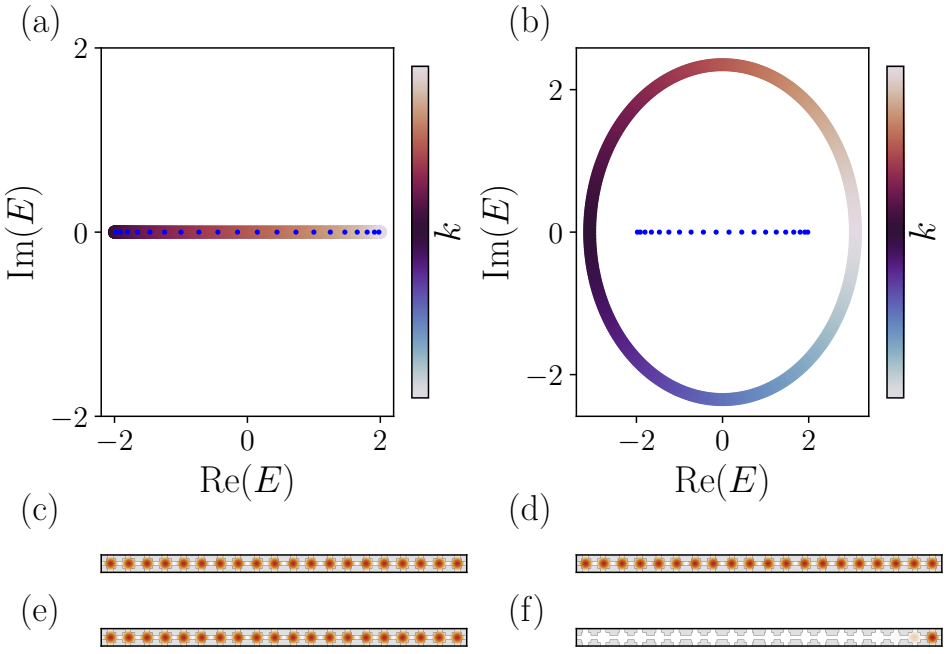

Figuur 1.4: Illustration of the sensitivity of non-Hermitian systems to boundary conditions, and comparison to Hermitian systems. (a) Spectrum of a Hermitian system with periodic boundary conditions as a function of k, and with open boundary conditions (blue dots). (b) Same as (a) but for a non-Hermitian system with left hopping $t_L = e^{-1}$ different from right hopping $t_R = e^1$. In (a) and (b), $k \in [0, 2\pi)$. (c) Spatial distribution of all the system eigenvectors in a periodic Hermitian system. Darker color indicates higher density. (d) Same as (c) but for a non-Hermitian system ($t_L = e^{-1}$, $t_R = e^1$). (e) Spatial distribution of all the system eigenvectors in a Hermitian system with open boundary conditions. (f) Same as (e) but for a non-Hermitian system ($t_L = e^{-1}$, $t_R = e^1$).

the cases where the spectra of the non-Hermitian Hamiltonian are real and the time-evolution is unitary, which occurs in the presence of $\mathscr{PT}$ symmetry, the combination of spatial parity ($\mathscr{P}$) and time-reversal symmetry ($\mathscr{T}$). When a non-Hermitian Hamiltonian H and $\mathscr{PT}$ share a finite number of eigenvectors, the spectrum of H is real. $\mathscr{PT}$-symmetric non-Hermitian systems are realizable in classical optical frameworks with non-Hermitian potentials, due to the correspondence between the Schrödinger equation and the wave equation in optics [35]. Experimental realizations of $\mathscr{PT}$-symmetric non-Hermitian optical systems include waveguide and cavity setups [36–38], fiber optical setups [39], meta-materials [35] and microwave systems [40]. Electronic circuits also lend themselves to the realization of $\mathscr{PT}$-symmetric non-Hermitian models with the use of amplifying and attenuating *LRC* components [41]. More recently, circuits were also used to simulate non-Hermitian models without $\mathscr{PT}$ symmetry [42–46], in light of the properties unique to non-Hermitian Hamiltonians.

One such phenomenon unique to non-Hermitian systems is the radical difference between the spectrum of an infinite or periodic system and the spectrum of a finite, open

system. In Hermitian systems, whether a system has periodic or open boundaries has little effect on its spectrum [Fig. 1.4 (a)] or on the spatial distribution of its modes [Fig. 1.4 (c) and (e)]. In non-Hermitian systems, both the spectrum and spatial distribution strongly depend on the boundary conditions [47]. The eigenvalues of periodic 1D non-Hermitian Hamiltonians are complex and form closed loops on the complex plane [Fig. 1.4 (b)]. The eigenvalues of a finite non-Hermitian chain are also complex, but form a 1D line entirely enclosed in the spectrum of the corresponding periodic system [Fig. 1.4 (b)] [48]. This extreme sensitivity to boundary conditions demonstrates that non-Hermitian systems do not follow the near-sightedness principle, which requires electronic states to only react to changes in their local environment [49]. The absence of the near-sightedness principle results in non-Hermitian responses differing greatly from Hermitian responses, the most well-known example of which is the non-Hermitian skin effect.

1.4.2. THE NON-HERMITIAN SKIN EFFECT AND NON-HERMITIAN TOPOLOGY

Consider a non-Hermitian Hamiltonian modeling a tight-binding 1D chain whose hopping to the right is larger than its hopping to the left, resulting in a preferred hopping direction. This preferred hopping direction has a profound consequence for the distribution of modes of the system. If the system is periodic, the modes of the system have a tendency to spread out evenly over the sites of the chain [Fig. 1.4 (d)]. If the system has open boundaries, then all of the modes of the system at any energy will accumulate at the boundary that lies in the preferred hopping direction [Fig. 1.4 (f)]. This phenomenon is known as the non-Hermitian skin effect (NHSE). The NHSE occurs generically in non-Hermitian systems with a preferred hopping direction in 1D, 2D, 3D, and potentially systems of arbitrary dimension [50, 51].

Both the surface modes of topological systems and the NHSE only exist in the presence of open boundaries or impurities. This similarity prompted the question as to whether the NHSE was a topological phenomenon, whether a quantized bulk invariant could predict which boundary would host the NHSE, and whether it could provide a topological explanation for why all of the modes of the system were delocalized to the edge. The spectrum of a periodic 1D chain winds around each of the open system eigenvalues an integer number of times [Fig. 1.4 (b)]. The winding number of a non-Hermitian Hamiltonian $H(k)$ evaluated at an energy E is given by [48]:

$$W(E) = \int_0^{2\pi} \frac{dk}{2\pi i} \frac{d}{dk} \log(\det(H(k) - E)). \tag{1.7}$$

Taking E to be each eigenvalue of the open system, the winding number has a given sign for each eigenvalue. The sign of the winding number dictates at which boundary of the open 1D chain that eigenstate will accumulate. Since a bulk quantity predicts the position and quantity of modes at each boundary, the NHSE was deemed topological and fulfilled a modified bulk-edge correspondence, where all of the bulk modes are delocalized to the edges of the system .

1.4.3. LOCALIZATION PROPERTIES

The transition of non-Hermitian systems from periodic to open boundary conditions involves the delocalization of all of the modes in the bulk to the system boundaries [Fig. 1.4

(d) and (f)]. The transition between a Hermitian and non-Hermitian system with open boundaries is also accompanied by the same delocalization of the bulk modes to the edge [Fig. 1.4 (e) and (f)]. This delocalization of all bulk modes is robust to disorder, so long as the non-Hermiticity of the bulk and the preferred direction of propagation is globally preserved [52–54]. This is in direct contrast to one-dimensional disordered Hermitian systems, where localization is generally expected to occur even in the presence of weak disorder [1]. Even when the disorder is sufficient to stop ballistic propagation of modes in a non-Hermitian system, transport through the disordered material persists through hopping between localized resonances [55, 56]. As long as the non-Hermitian system is capable of amplifying the signal, the system is able to delocalize in any dimension [57].

Due to the difference in Anderson localization properties disorder between Hermitian and non-Hermitian systems, a separate scaling theory of localization was devised [57], which relies on two-parameter scaling as opposed to one-parameter scaling (dependence of conductance on length scale L). The second parameter involved in non-Hermitian scaling is the hopping asymmetry γ. For γ sufficiently large, the scaling flow of conductance as a function of L is modified and diverges away from 0 to ∞ [Fig. 1.5].

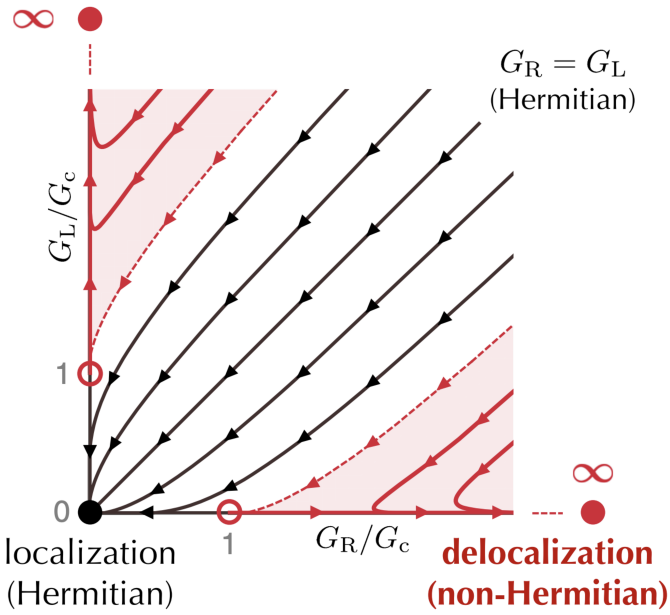

Figuur 1.5: Two-parameter scaling of non-Hermitian localization. The renormalization-group flow is shown according to the conductance G_R from the left to the right and the conductance G_L from the right to the left. The system size L increases along with the arrows. Figure reproduced with permission from [57].

1.5. THIS THESIS

The study of topological systems is closely tied to symmetry analysis. A 2D regular crystal structure possesses exact spatial symmetries, and such symmetries have been found to

protect topological phases of matter, giving rise to protected propagating edge modes. Crystal surfaces that break the bulk spatial symmetries protecting the topological phase will not host topological edge modes. Amorphous systems appear to possess no spatial symmetries at face value, but they are not so far removed from an isotropic continuum: amorphous systems are isotropic on average, having average reflection and continuous rotation symmetry in 2D. The combination of these average spatial symmetries, if they could protect a topological phase, would therefore result in a phase that is insensitive to surface orientation. In Chapter 2, I present 2D amorphous systems which host topological insulator phases and have delocalized gapless edge modes on any surface orientation. Since the symmetries protecting the phase are only present on average, the topological phases are statistical topological insulator phases. This means that 2D amorphous topological phases protected by spatial symmetries exist in all symmetry classes that possess a 1D topological phase.

Extending the study of amorphous topological phases to 3D is as simple as searching for statistical topological insulator phases. Similarly to the approach explained in Chapter 2, one searches for strong or statistical topological insulator phases in 2D. These correspond to the gapless surfaces of 3D statistical topological insulators. However, one rather quickly encounters conceptual difficulties even for the class with the least amount of constraints, class A (no non-spatial symmetries, see Table 1.1). While it is possible to generate a Hamiltonian from any given set of constraints, difficulties arise in the interpretation and realization of the physical system it represents. Until now, it was an open question whether a 3D inversion-symmetric system could exist without time-reversal symmetry. Although it was not guaranteed that these symmetries should only appear together, common ingredients for breaking time-reversal symmetry like magnetic fields, magnetic moments or currents also break inversion symmetry, since they are axial vectors. The realization of an inversion-symmetric medium without time-reversal symmetry therefore cannot rely on conventional time-reversal symmetry breaking methods. In Chapter 3, we present an isotropic system with scalar time-reversal symmetry breaking. The time-reversal symmetry breaking mechanism relies on virtual hopping processes through states forming a chiral magnetic texture perpendicular to the atomic bond. Time-reversal symmetry is broken independently of the orientation of the bond, while inversion symmetry is preserved. This means that this system is realizable not only as a crystal with a regular structure, but also as amorphous systems. The surface of the amorphous system is akin to a disordered critical mirror Chern insulator, whose transport properties have been the subject of debate. In particular, there have been contradictory numerical and analytical results as to whether the doubled disordered Chern insulator model localizes in the critical phase [58–64]. Using network model analysis and investigating large system sizes to resolve this long-standing question, the doubled disordered Chern insulator is found to localize, with a large localization length. A natural question arises: are the average spatial symmetries of the amorphous system capable of protecting the modes from localization? The results of the amorphous network and the regular network coincide, and in both cases the doubled model localizes, which demonstrates that the spatial symmetries do not affect the scaling properties of the system.

While general disorder in Hermitian systems can be used to stabilize topological edge modes, in non-Hermitian systems disorder has the power to disrupt the very notion of

bulk-edge correspondence. The modes of the non-Hermitian skin effect (NHSE), that is to say all of the modes of a 1D non-Hermitian system with a point gap, have been considered topological modes due to their appearance at the boundaries of the system and the identification of a bulk topological index predicting their appearance. Further, in the presence of moderate Hermitian disorder, the NHSE persists, similar to how a Hermitian topological phase is robust to disorder that does not exceed the magnitude of the bulk gap. However, non-Hermitian systems differ from Hermitian systems in the fact that they do not obey the near-sightedness principle. This principle states that areas of a system sufficiently far from a perturbation are not affected by it. Hermitian topological phases exemplify this principle, as topological edge modes can be locally shifted or destroyed (in the case of crystalline topological insulators), but the edge modes far from that perturbation will remain affected. Non-Hermitian systems demonstrate the violation of the near-sightedness principle by the very phenomenon of the NHSE, which is tantamount to the sensitivity of all of the modes in the system to a local change in the boundary conditions, not just the modes close to the boundary. Following the existence of this sensitivity, in Chapter 4 I demonstrate that a single non-Hermitian impurity in the bulk of 1D and 2D systems has the ability to attract all of the skin modes from the boundary to itself. This violates bulk-edge correspondence, since the bulk topological marker predicting the presence of the skin modes at the boundaries of the system is not affected by the presence of the impurity. Therefore, the characterization of the NHSE as a topological phase is made more tenuous, since it is only valid in the translationally invariant case where disorder is absent.

The extreme sensitivity of non-Hermitian modes to all local system details makes the study of non-Hermitian disorder extend beyond conventional Anderson localization, and yields new delocalization phase transitions that have no Hermitian counterpart. In Chapter 5 I further investigate non-Hermitian systems beyond a topological framework and explore dynamic phase transitions of non-Hermitian in systems with general disorder. In a non-Hermitian disorder landscape, a wave packet scatters inelastically and acquires various components that are eigenstates of the disordered system. These eigenstates are amplified or suppressed at rates that are dictated by the imaginary parts of the corresponding eigenvalues. As the wave packet evolves in time, the fastest amplified modes will dominate the dynamics of the system. The convergence of the initial wave packet to the maximally amplified wave packet is universal in the presence of moderate disorder. As a result of this phenomenon, non-Hermitian dynamic phase transitions differ from those observed in static studies of non-Hermitian systems. I demonstrate the existence of a transition between two propagating phases that is unique to non-Hermitian dynamics, and which is only realizable in the presence of disorder.

BIBLIOGRAFIE

[1] P. W. Anderson, *Absence of diffusion in certain random lattices,* Phys. Rev. **109**, 1492 (1958).

[2] F. Evers and A. D. Mirlin, *Anderson transitions,* Rev. Mod. Phys. **80**, 1355 (2008).

[3] A. G. Grushin, *Topological phases of amorphous matter,* (2020), arXiv:2010.02851 .

[4] C.-K. Chiu, J. C. Y. Teo, A. P. Schnyder, and S. Ryu, *Classification of topological quantum matter with symmetries,* Rev. Mod. Phys. **88**, 035005 (2016).

[5] C. L. Kane and E. J. Mele, *Quantum spin hall effect in graphene,* Phys. Rev. Lett. **95**, 226801 (2005).

[6] A. Y. Kitaev, *Unpaired majorana fermions in quantum wires,* Physics-Uspekhi **44**, 131 (2001).

[7] W. P. Su, J. R. Schrieffer, and A. J. Heeger, *Solitons in polyacetylene,* Phys. Rev. Lett. **42**, 1698 (1979).

[8] S. Ryu, A. P. Schnyder, A. Furusaki, and A. W. W. Ludwig, *Topological insulators and superconductors: tenfold way and dimensional hierarchy,* New Journal of Physics **12**, 065010 (2010).

[9] A. Kitaev, V. Lebedev, and M. Feigelman, *Periodic table for topological insulators and superconductors,* in *AIP Conference Proceedings* (AIP, 2009).

[10] L. Fu, *Topological crystalline insulators,* Phys. Rev. Lett. **106**, 106802 (2011).

[11] J. Kruthoff, J. de Boer, J. van Wezel, C. L. Kane, and R.-J. Slager, *Topological classification of crystalline insulators through band structure combinatorics,* Phys. Rev. X **7**, 041069 (2017).

[12] K. Shiozaki and M. Sato, *Topology of crystalline insulators and superconductors,* Phys. Rev. B **90**, 165114 (2014).

[13] M. Z. Hasan and C. L. Kane, *Colloquium: Topological insulators,* Reviews of Modern Physics **82**, 3045 (2010).

[14] M. Hell, M. Leijnse, and K. Flensberg, *Two-dimensional platform for networks of majorana bound states,* Phys. Rev. Lett. **118**, 107701 (2017).

[15] H. Zhang, O. Gul, S. Conesa-Boj, M. P. Nowak, M. Wimmer, K. Zuo, V. Mourik, F. K. de Vries, J. van Veen, M. W. A. de Moor, J. D. S. Bommer, D. J. van Woerkom, D. Car, S. R. Plissard, E. P. Bakkers, M. Quintero-Pérez, M. C. Cassidy, S. Koelling, S. Goswami, K. Watanabe, T. Taniguchi, and L. P. Kouwenhoven, *Ballistic superconductivity in semiconductor nanowires,* Nat. Commun. **8**, 16025 (2017).

[16] F. Nichele, A. C. C. Drachmann, A. M. Whiticar, E. C. T. O'Farrell, H. J. Suominen, A. Fornieri, T. Wang, G. C. Gardner, C. Thomas, A. T. Hatke, P. Krogstrup, M. J. Manfra, K. Flensberg, and C. M. Marcus, *Scaling of majorana zero-bias conductance peaks,* Phys. Rev. Lett. **119**, 136803 (2017).

[17] J. D. Sau, S. Tewari, R. M. Lutchyn, T. D. Stanescu, and S. Das Sarma, *Non-abelian quantum order in spin-orbit-coupled semiconductors: Search for topological majorana particles in solid-state systems,* Phys. Rev. B **82**, 214509 (2010).

[18] Y. Oreg, G. Refael, and F. von Oppen, *Helical liquids and majorana bound states in quantum wires,* Phys. Rev. Lett. **105**, 177002 (2010).

[19] A. Tsintzis, R. S. Souto, and M. Leijnse, *Creating and detecting poor man's majorana bound states in interacting quantum dots,* Physical Review B **106** (2022), 10.1103/physrevb.106.l201404.

[20] J. D. Sau and S. D. Sarma, *Realizing a robust practical majorana chain in a quantum-dot-superconductor linear array,* Nat. Commun. **3** (2012), 10.1038/ncomms1966.

[21] M. Leijnse and K. Flensberg, *Parity qubits and poor man's majorana bound states in double quantum dots,* Phys. Rev. B **86**, 134528 (2012).

[22] I. C. Fulga, A. Haim, A. R. Akhmerov, and Y. Oreg, *Adaptive tuning of majorana fermions in a quantum dot chain,* New Journal of Physics **15**, 045020 (2013).

[23] T. Dvir, G. Wang, N. van Loo, C.-X. Liu, G. P. Mazur, A. Bordin, S. L. D. ten Haaf, J.-Y. Wang, D. van Driel, F. Zatelli, X. Li, F. K. Malinowski, S. Gazibegovic, G. Badawy, E. P. A. M. Bakkers, M. Wimmer, and L. P. Kouwenhoven, *Realization of a minimal kitaev chain in coupled quantum dots,* Nature **614**, 445 (2023).

[24] C.-X. Liu, J. D. Sau, T. D. Stanescu, and S. Das Sarma, *Andreev bound states versus majorana bound states in quantum dot-nanowire-superconductor hybrid structures: Trivial versus topological zero-bias conductance peaks,* Phys. Rev. B **96**, 075161 (2017).

[25] S. Ahn, H. Pan, B. Woods, T. D. Stanescu, and S. D. Sarma, *Estimating disorder and its adverse effects in semiconductor majorana nanowires,* Physical Review Materials **5** (2021), 10.1103/physrevmaterials.5.124602.

[26] H. Kim, A. Palacio-Morales, T. Posske, L. Rózsa, K. Palotás, L. Szunyogh, M. Thorwart, and R. Wiesendanger, *Toward tailoring majorana bound states in artificially constructed magnetic atom chains on elemental superconductors,* Science Advances **4**, eaar5251 (2018), https://www.science.org/doi/pdf/10.1126/sciadv.aar5251 .

[27] H. Pan and S. D. Sarma, *Disorder effects on majorana zero modes: Kitaev chain versus semiconductor nanowire,* Physical Review B **103** (2021), 10.1103/physrevb.103.224505.

[28] S. Das Sarma and H. Pan, *Disorder-induced zero-bias peaks in majorana nanowires,* Phys. Rev. B **103**, 195158 (2021).

[29] A. Agarwala and V. B. Shenoy, *Topological Insulators in Amorphous Systems,* Phys. Rev. Lett. **118**, 236402 (2017).

[30] I. C. Fulga, B. van Heck, J. M. Edge, and A. R. Akhmerov, *Statistical topological insulators,* Phys. Rev. B **89**, 155424 (2014).

[31] L. Fu and C. L. Kane, *Topology, delocalization via average symmetry and the symplectic anderson transition,* Phys. Rev. Lett. **109**, 246605 (2012).

[32] K. Muttalib, P. Wölfle, and V. Gopar, *Conductance distribution in quasi-one-dimensional disordered quantum wires,* Annals of Physics **308**, 156 (2003).

[33] M. Diez, I. C. Fulga, D. I. Pikulin, J. Tworzydło, and C. W. J. Beenakker, *Bimodal conductance distribution of kitaev edge modes in topological superconductors,* New Journal of Physics **16**, 063049 (2014).

[34] C. M. Bender, *Making sense of non-hermitian hamiltonians,* Reports on Progress in Physics **70**, 947 (2007).

[35] L. Feng, Y.-L. Xu, W. S. Fegadolli, M.-H. Lu, J. B. Oliveira, V. R. Almeida, Y.-F. Chen, and A. Scherer, *Experimental demonstration of a unidirectional reflectionless parity-time metamaterial at optical frequencies,* Nature Mater. **12**, 108 (2013).

[36] C. E. Rüter, K. G. Makris, R. El-Ganainy, D. N. Christodoulides, M. Segev, and D. Kip, *Observation of parity–time symmetry in optics,* Nature Phys. **6**, 192 (2010).

[37] H. Hodaei, M.-A. Miri, M. Heinrich, D. N. Christodoulides, and M. Khajavikhan, *Parity-time–symmetric microring lasers,* Science **346**, 975 (2014).

[38] L. Chang, X. Jiang, S. Hua, C. Yang, J. Wen, L. Jiang, G. Li, G. Wang, and M. Xiao, *Parity–time symmetry and variable optical isolation in active–passive-coupled microresonators,* Nature Photon. **8**, 524 (2014).

[39] A. Regensburger, C. Bersch, M.-A. Miri, G. Onishchukov, D. N. Christodoulides, and U. Peschel, *Parity–time synthetic photonic lattices,* Nature **488**, 167 (2012).

[40] Y. Liu, T. Hao, W. Li, J. Capmany, N. Zhu, and M. Li, *Observation of parity-time symmetry in microwave photonics,* Light: Science and Applications **7** (2018), 10.1038/s41377-018-0035-8.

[41] J. Schindler, A. Li, M. C. Zheng, F. M. Ellis, and T. Kottos, *Experimental study of active lrc circuits with $\mathscr{PT}$ symmetries,* Phys. Rev. A **84**, 040101 (2011).

[42] D.-A. Galeano, X.-X. Zhang, and J. Mahecha, *Topological circuit of a versatile non-hermitian quantum system,* Science China Physics, Mechanics and Astronomy **65** (2021), 10.1007/s11433-021-1783-3.

[43] S. Liu, R. Shao, S. Ma, L. Zhang, O. You, H. Wu, Y. J. Xiang, T. J. Cui, and S. Zhang, *Non-hermitian skin effect in a non-hermitian electrical circuit,* Research **2021** (2021), 10.34133/2021/5608038.

[44] H. Yuan, W. Zhang, Z. Zhou, W. Wang, N. Pan, Y. Feng, H. Sun, and X. Zhang, *Non-hermitian topolectrical circuit sensor with high sensitivity,* Advanced Science **10**, 2301128 (2023).

[45] L. Su, H. Jiang, Z. Wang, S. Chen, and D. Zheng, *Simulation of non-hermitian disordered systems in linear circuits,* Phys. Rev. B **107**, 184108 (2023).

[46] H. Zhang, T. Chen, L. Li, C. H. Lee, and X. Zhang, *Electrical circuit realization of topological switching for the non-hermitian skin effect,* Phys. Rev. B **107**, 085426 (2023).

[47] E. Edvardsson and E. Ardonne, *Sensitivity of non-hermitian systems,* Phys. Rev. B **106**, 115107 (2022).

[48] N. Okuma, K. Kawabata, K. Shiozaki, and M. Sato, *Topological origin of non-hermitian skin effects,* Physical Review Letters **124** (2020), 10.1103/physrevlett.124.086801.

[49] E. Prodan and W. Kohn, *Nearsightedness of electronic matter,* Proceedings of the National Academy of Sciences **102**, 11635 (2005).

[50] N. Okuma and M. Sato, *Non-hermitian topological phenomena: A review,* Annual Review of Condensed Matter Physics **14**, 83 (2023).

[51] X. Zhang, T. Zhang, M.-H. Lu, and Y.-F. Chen, *A review on non-hermitian skin effect,* Advances in Physics: X **7**, 2109431 (2022).

[52] P. W. Brouwer, P. G. Silvestrov, and C. W. J. Beenakker, *Theory of directed localization in one dimension,* Phys. Rev. B **56**, R4333 (1997).

[53] N. Hatano and D. R. Nelson, *Localization transitions in non-hermitian quantum mechanics,* Phys. Rev. Lett. **77**, 570 (1996).

[54] J. Feinberg and A. Zee, *Non-hermitian localization and delocalization,* Phys. Rev. E **59**, 6433 (1999).

[55] H. Sahoo, R. Vijay, and S. Mujumdar, *Anomalous transport regime in non-hermitian, anderson-localizing hybrid systems,* (2022).

[56] S. Weidemann, M. Kremer, S. Longhi, and A. Szameit, *Non-hermitian anderson transport,* (2020).

[57] K. Kawabata and S. Ryu, *Nonunitary scaling theory of non-hermitian localization,* Phys. Rev. Lett. **126**, 166801 (2021).

[58] D. K. K. Lee and J. T. Chalker, *Unified model for two localization problems: Electron states in spin-degenerate landau levels and in a random magnetic field,* Phys. Rev. Lett. **72**, 1510 (1994).

[59] M. R. Zirnbauer, *Toward a theory of the integer quantum hall transition: Continuum limit of the chalker–coddington model,* Journal of Mathematical Physics **38**, 2007 (1997).

[60] G. Xiong, S.-D. Wang, Q. Niu, Y. Wang, X. C. Xie, D.-C. Tian, and X. R. Wang, *Possible existence of a band of extended states induced by inter-landau-band mixing in a quantum hall system,* J. Phys.: Condens. Matter **18** (2006), 10.1088/0953-8984/18/6/017.

[61] K. Minakuchi and S. Hikami, *Numerical study of localization in the two-state landau level,* Phys. Rev. B **53**, 10898 (1996).

[62] G. Xiong, S.-D. Wang, Q. Niu, D.-C. Tian, and X. R. Wang, *Metallic phase in quantum hall systems due to inter-landau-band mixing,* Phys. Rev. Lett. **87**, 216802 (2001).

[63] D. G. Polyakov, *Spin-flip scattering in the quantum hall regime,* Phys. Rev. B **53**, 15777 (1996).

[64] V. Kagalovsky, B. Horovitz, and Y. Avishai, *Landau-level mixing and spin degeneracy in the quantum hall effect,* Phys. Rev. B **55**, 7761 (1997).

2

AMORPHOUS TOPOLOGICAL PHASES PROTECTED BY CONTINUOUS ROTATION SYMMETRY

Innovation requires, above all else, a willingness to embrace chaos.

Tim Brown

This chapter has been previously published as Helene Spring, Anton R. Akhmerov, Dániel Varjas, *Amorphous topological phases protected by continuous rotation symmetry*, SciPost Phys. 11, 022 (2021).
Own contribution to work: I contributed to refining the initial project goal. I performed the numerical and computer algebra calculations with assistance from co-authors. I wrote the initial manuscript and contributed to refining of the manuscript to its final version.

2.1. INTRODUCTION

Materials with a quasiparticle band gap in the bulk host protected edge states if they have a nontrivial topology. To determine whether an insulator or a superconductor is topological, one first determines the symmetry class of the quasiparticle Hamiltonian in this material, and then evaluates the topological invariant of the Hamiltonian's symmetry class [1, 2]. The topological invariant stays constant as long as the symmetry is preserved and the bulk stays gapped. While the specific properties of the surface states depend on details of the edge, they may not be removed by any symmetry-preserving surface perturbation due to the bulk-boundary correspondence.

The classification of topological phases started with the Altland-Zirnbauer classes, based on discrete onsite symmetries: particle-hole, time-reversal, and chiral symmetry [3, 4]. Topological crystalline phases were also classified [5–8], protected by crystal symmetries. The bulk-boundary correspondence, however, does not apply to all edges in this case: spatial symmetries such as reflection are broken by certain edge orientations [9] and the edge states may become gapped, as seen in the top panels of Fig. 2.1.

When perturbations are introduced to a system with nontrivial topology, the topological phases may be destroyed if the symmetries are affected. Perturbed symmetries present on average are able to provide topological protection [10]. Disordered systems that support topological insulating phases with one exact symmetry and one or more average symmetries are called statistical topological insulators [11]. The surfaces of statistical topological insulators are delocalized and pinned to the midpoint of a topological phase transition, or critical point. A crystal surface that respects a crystalline symmetry on average is still able to host crystalline topological phases.

Unlike crystals, which break continuous rotation symmetry even on average, amorphous systems lack long-range order and are therefore on average compatible with continuous rotations. Strong topological, metallic and insulating phases as well as topological superconductivity have been studied in amorphous systems both theoretically [12–18] and experimentally [19–21].

In this work, we devise topological insulator (TI) phases in amorphous systems that rely on the presence of two average spatial symmetries: reflection symmetry and continuous rotation symmetry. The presence of both reflection symmetry and average continuous rotation symmetry promotes the protection of a crystalline topological phase to every edge orientation. We thus demonstrate that even though the topological phases presented here have crystalline or quasi-crystalline counterparts, only amorphous systems have guaranteed protection for all edge terminations. This study exposes the potential for realizing topological phases protected by average spatial symmetries that don't rely on macroscopic edge details.

The structure of the manuscript is as follows. In Sec. 2.2 we define the basic premise of spatial symmetries in amorphous systems. In Sec. 2.3 we study isotropic continuum systems and identify the symmetry groups containing reflection symmetry that protect gapless edge states. In Sec. 2.4 we construct amorphous tight-binding models, numerically demonstrate critical edge transport, and compare with a similar system on a regular square lattice. Finally, we formulate bulk topological invariants of our systems in Sec. 2.5. We conclude in Sec. 2.6 that amorphous models relying on spatial symmetries as well as one or more exact onsite symmetry to protect a topological phase are statistical topologi-

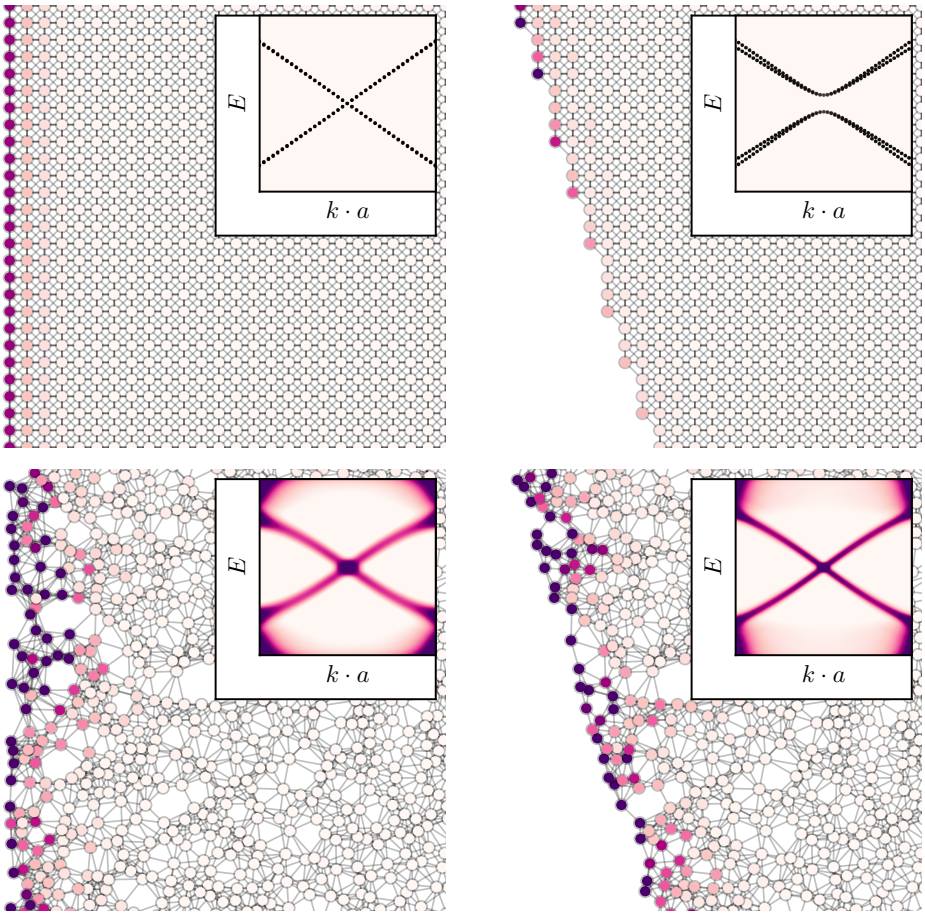

Figuur 2.1: The zero-energy local density of propagating modes of the class D 8-band model in crystal and amorphous systems; darker site color indicates higher density. Insets: dispersion relation (top) and momentum-resolved spectral function (bottom) corresponding to straight and tilted edge terminations. The effective lattice constant of the amorphous system a is given by $a = 1/\sqrt{\rho}$, where ρ is the density of sites in the system. Plot details in App. 2.A.

cal insulators, provided the disorder of the amorphous system does not close the bulk gap.

2.2. SPATIAL SYMMETRIES IN AMORPHOUS MATTER

Despite locally breaking all spatial symmetries, amorphous matter is generated by a highly symmetric ensemble of Hamiltonians. Specifically, the occurrence probability of any configuration is invariant under the action of any element of the Euclidean group. Furthermore, all structural correlations must decay sufficiently fast with distance. These conditions require care to satisfy and cannot be fulfilled by gradually moving sites from

their crystalline positions. While there are several ways to simulate amorphous matter, we focus on tight-binding models defined on random graphs. The simplest way to create an amorphous array of site positions is choosing a sample of uncorrelated points in space. In order to reduce the fluctuations of the coordination number, we use a sphere-packing algorithm described in App. 5.B instead.

The physics of amorphous systems obeys locality and homogeneity in the sense that the bulk Hamiltonian is generated by a local rule [22, 23]. We require that the onsite and hopping terms only depend on the local environment: the configuration of atoms within a finite radius of the site or bond in question. For our toy models we take an even simpler case, where terms in the Hamiltonian only depend on the relative spatial positions of the orbitals:

$$\langle \mathbf{r}, n| \hat{H} |\mathbf{r}', m\rangle = H_{nm}(\mathbf{r}-\mathbf{r}'), \tag{2.1}$$

where $|\mathbf{r}, n\rangle$ is the n'th orbital on the site at position $\mathbf{r}$. While this restriction is not essential, it makes defining the models easier. Onsite terms have $\mathbf{r}-\mathbf{r}' \equiv \mathbf{d} = 0$, meaning all onsite terms in the bulk are identical. More generally, we allow $H(\mathbf{d})$ to be a random matrix whose distribution only depends on the hopping vector $\mathbf{d}$ to account for sources of disorder not captured by the underlying random graph or the simplified local rule. In this case we demand that the disordered ensemble is invariant under each spatial symmetry, whereas the onsite symmetries are obeyed exactly by each ensemble element.

An isotropic amorphous system has average continuous rotation symmetry under simultaneous rotation in spin and real space, meaning that terms in the Hamiltonian with a rotated local environment are related as:

$$U(\phi)H(\mathbf{d})U(\phi)^{-1} = H(R(\phi)\cdot\mathbf{d}) \tag{2.2}$$

with $U(\phi) = \exp(i\phi S_z)$, S_z the onsite spin-z operator, $R(\phi) = \exp(i\phi L_z)$, $L_z = \sigma_y$ the generator of two-dimensional real space rotations. Simultaneous invariance under continuous rotation and one reflection symmetry implies reflection invariance with any normal vector. The symmetry constraint imposed by a reflection operator with normal $\hat{\mathbf{n}}$ is:

$$U_{M_{\hat{\mathbf{n}}}} H(\mathbf{d}) U_{M_{\hat{\mathbf{n}}}}^{-1} = H(R_{M_{\hat{\mathbf{n}}}}\cdot\mathbf{d}) \tag{2.3}$$

where $R_{M_{\hat{\mathbf{n}}}} = \mathbb{1} - 2\hat{\mathbf{n}}\hat{\mathbf{n}}^T$ is the real space orthogonal action reversing the component in the $\hat{\mathbf{n}}$ direction. Commutation relations of S_z, U_M and onsite symmetries are listed in App. 2.C.

All previous considerations of this section apply to homogeneous and isotropic systems deep in the bulk. The vicinity of the edges of the system are, however, distinguishable from the bulk through the local environment, and have lower symmetry. Hence we allow the Hamiltonian to depend on the distance from the edge and the orientation of the edge. For example, near an infinite edge along the y direction such that the system terminates for $x < 0$ we let

$$\langle \mathbf{r}, n| \hat{H} |\mathbf{r}', m\rangle = H^{\text{edge}}_{nm}\left(\mathbf{r}-\mathbf{r}', \hat{x}\cdot\frac{\mathbf{r}+\mathbf{r}'}{2}\right). \tag{2.4}$$

such that $\lim_{x\to\infty} H^{\text{edge}}(\mathbf{d}, x) = H(\mathbf{d})$. This local rule preserves average translation invariance along the edge, but may break the continuous rotation symmetry (2.2) of the bulk. A straight edge still preserves average reflection symmetry with normal parallel to the edge, so we demand that H^{edge} satisfies (2.3) with fixed x and $\hat{\mathbf{n}} = \hat{y}$.

2.3. CONTINUUM SYSTEMS

In the long wavelength limit an amorphous system is homogeneous and isotropic, resembling a continuum. We therefore start our analysis by studying continuum models with reflection and continuous rotation invariance. First we study the 1D edge theory to identify symmetry groups capable of protecting gapless edge modes. Next we construct 2D bulk models in these symmetry classes, and finally we demonstrate that straight domain walls host gapless modes as expected.

2.3.1. SYMMETRY GROUPS PROTECTING GAPLESS EDGES

In order to find continuum models with gapless edges protected by reflection symmetry, we perform a systematic search of the Altland-Zirnbauer symmetry classes. For each class, we start with a minimal 1D Dirac Hamiltonian that respects the onsite symmetries. If mass terms are allowed in this Hamiltonian, *i.e.* it is trivial with only the onsite symmetries, we add a reflection symmetry. The Hamiltonian is a candidate model if the reflection symmetry protects the gapless edge by removing all mass terms.

Consider for example the edge of a class D system, the minimal two-band edge theory can always be written as $H_{\text{edge}}(k) = k\tau_x + m\tau_y$ with particle-hole symmetry acting as complex conjugation, $\mathscr{P} = \mathscr{K}$. In the absence of additional symmetries this model describes the edge of a trivial system because it is gapped for any nonzero m. Choosing a unitary reflection symmetry with $U_M = \tau_z$ the symmetry constraint $U_M H_{\text{edge}}(k) U_M^\dagger = H_{\text{edge}}(-k)$ forces $m = 0$. Hence this choice of reflection symmetry protects a single pair of counterpropagating gapless edge modes, and serves as a candidate for the edge theory of a topologically nontrivial bulk protected by reflection.

We perform the search of the Altland-Zirnbauer classes using the software package Qsymm [24]. In classes AII, DIII, CII and C the minimal model of a gappable edge is 4×4, in the rest of the classes it is 2×2. We fix a canonical form of the onsite symmetries, then vary the reflection-like symmetry using different products of Pauli matrices σ and τ for its unitary part, also allowing it to act as an antiunitarity (with complex conjugation) and as antisymmetry (reversing the sign of the Hamiltonian). This approach tests every possible reflection-like symmetry up to basis transformations. In this basis, we have $U_M^2 = +\mathbb{1}$. The conventional fermionic reflection operator that obeys $U_M^2 = -\mathbb{1}$ is recovered by multiplying U_M with i. This change of the overall phase does not affect the symmetry constraints on the Hamiltonian and only reverses commutation and anticommutation of U_M with the antiunitary symmetries. For each choice of the symmetry group, we generate the most general k-linear Hamiltonian. If it does not contain k-independent mass terms capable of opening a gap at half-filling, we note it as a candidate. When presenting the results in Table 2.1 we only list one representative of various reflection operators related by unitary basis transformations. In the rest of the manuscript we focus on the more natural symmetry groups with unitary reflection symmetry, see App. 2.D for symmetry groups with reflection antisymmetries.

Because we are searching for phases whose surfaces are driven to a critical point by spatial disorder, we expect to find protected gapless phases in the presence of strong disorder in symmetry classes that host nontrivial topological phases in 1D. This requires the disorder to respect all non-spatial symmetries in a given class exactly, and the spatial symmetries on average [11]. In this case the additional reflection symmetry forces the edge

Symmetry class	U_M	$U_{\mathscr{P}}$	$U_{\mathscr{T}}$	$U_{\mathscr{C}}$
AIII	τ_x	-	-	τ_x
BDI	τ_x	τ_0	τ_x	τ_x
D	τ_z	τ_0	-	-
DIII$_+$	$\sigma_x\tau_z$	$\sigma_0\tau_z$	$i\sigma_z\tau_y$	$\sigma_z\tau_x$
DIII$_-$	$\sigma_z\tau_x$			
CII	$\sigma_y\tau_y$	$i\sigma_y\tau_0$	$i\sigma_0\tau_y$	$\sigma_y\tau_y$

Tabel 2.1: Symmetry representations of 1D models where a unitary reflection symmetry U_M protects gapless edges. σ and τ are Pauli matrices. Only unitary-inequivalent symmetry representations are listed.

to the critical point of a topological phase transition. The result of our search confirms this expectation, we find unitary reflection symmetries in classes AIII, BDI, CII, D and DIII. We observe that in all the chiral classes $[U_M,\mathscr{C}]=0$, and in all cases $[U_M,\mathscr{P}]=[U_M,\mathscr{T}]=0$ except for one of the choices for class DIII where $\{U_M,\mathscr{P}\}=\{U_M,\mathscr{T}\}=0$. We denote the case with commuting reflection DIII$_+$ and the case with anticommuting reflection DIII$_-$ in the following.

When attempting to extend these symmetries to the 2D bulk, we find that these symmetry representations do not admit a consistent continuous rotation symmetry with $S_z=\pm 1/2$ (see App. 2.C) in a way that allows a gapped bulk, so we double the Hilbert-space. We perform a systematic search for symmetry representations by taking the tensor product of each edge symmetry operator with a Pauli matrix, taking S_z as $1/2$ times the product of Pauli matrices and ensuring that the appropriate commutation relations are maintained. While this search is not exhaustive, it produces gapped bulk models realizing all the edge symmetry classes. The exact forms of the onsite and spatial symmetries in the bulk are listed in App. 2.D.

2.3.2. BULK MODELS

We use Qsymm to obtain continuum models in reciprocal space (k-space) compatible with the bulk symmetry representations found in the previous subsection. The symmetry constraints have the following form in k-space:

$$U(\phi)H(\mathbf{k})U(\phi)^{-1}=H(R(\phi)\cdot\mathbf{k}) \tag{2.5}$$

$$U_M H(\mathbf{k})U_M^{-1}=H(R_M\cdot\mathbf{k}) \tag{2.6}$$

$$U_{\mathscr{C}} H(\mathbf{k})U_{\mathscr{C}}^{-1}=-H(\mathbf{k}) \tag{2.7}$$

$$U_{\mathscr{P}} H^*(\mathbf{k})U_{\mathscr{P}}^{-1}=-H(-\mathbf{k}) \tag{2.8}$$

$$U_{\mathscr{T}} H^*(\mathbf{k})U_{\mathscr{T}}^{-1}=H(-\mathbf{k}). \tag{2.9}$$

We generate all symmetry allowed terms up to linear order in k in 4-band models for classes AIII, BDI and D, and 8-band models in classes DIII and CII. We also include one $\mathbf{k}^2$ term to ensure proper regularization in the large k limit (see Sec. 2.5.1). We split the Hamiltonian into k-independent onsite (or mass) terms and k-dependent hopping terms as $H(\mathbf{k})=H^{\text{os}}+H^{\text{hop}}(\mathbf{k})$, see the explicit enumeration of all the terms in App. 2.E.1.

For classes AIII, BDI and D, while the minimal 4-band models have gapped bulk, we

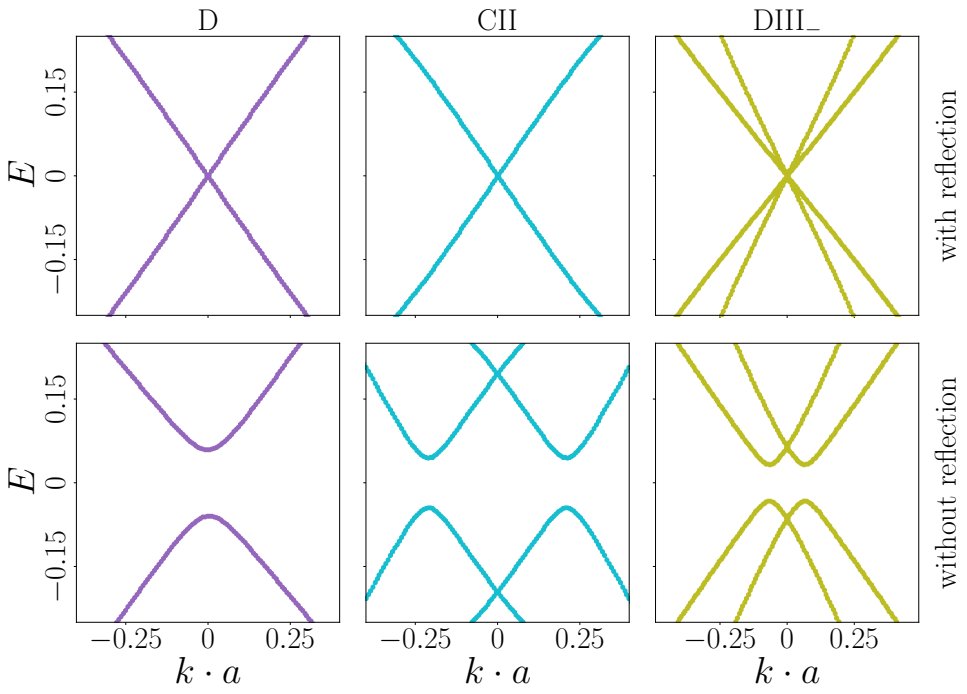

Figuur 2.2: Domain wall spectra of the continuum models in classes D, CII and class DIII obtained numerically. For class DIII, the anticommuting case DIII_ is represented. With reflection symmetry the boundary spectrum is gapless (top row), while reflection-breaking terms open a gap (bottom row).

find that these systems are non-generic for the prescribed symmetries. The minimal class BDI model consists of two decoupled blocks resulting in an additional onsite unitary symmetry, the class AIII model has an additional time-reversal symmetry, and the class D model remains decoupled at $\mathbf{k} = 0$ resulting in extra protection for the edge modes. To get rid of the additional symmetries, we consider a doubled Hamiltonian:

$$H_{8\times 8}(\mathbf{k}) = \begin{pmatrix} H(\mathbf{k}) & H^{c}(\mathbf{k}) \\ H^{c}(\mathbf{k})^{\dagger} & H'(\mathbf{k}) \end{pmatrix} \tag{2.10}$$

where H is topological, H' is trivial, and H^{c} is weak. The forms of the coupling between the two copies, H^{c}, are listed in App. 2.E.1. We then confirm that the resulting doubled model remains topological, and the additional symmetries are removed. The 8-band CII and DIII models have no unwanted symmetries, so they are not doubled.

2.3.3. GAPLESS DOMAIN WALL MODES

To show that the bulk models have the expected edge physics, we obtain the continuum edge spectra of our models by considering an infinite 2D system with a domain wall. We assign a spatial dependence to the chemical potential, such that at $x = 0$ its sign is flipped, making the system topological for $x > 0$ and trivial for $x < 0$. Topological edge modes are confined to the interface and decay exponentially into the bulk.

The continuum model $H_{\text{cont}}(k)$ is obtained from (2.10) by replacing k_y with a free parameter k and k_x with its real-space form $-i\partial_x$. We cast the eigenvalue problem $H_{\text{cont}}\Psi = E\Psi$ into the form of a system of linear differential equations $A(k)\partial_x\Psi + B(k,x,E)\Psi = 0$. We find all the solutions on the left and right side of the domain wall separately, using the ansatz $\Psi_{\text{L/R}}(x) = \psi_{\text{L/R}}\exp(-\lambda_{\text{L/R}}|x|)$ to obtain $(A-\lambda_{\text{L/R}}B)\psi_{\text{L/R}} = 0$. We solve this generalized eigenvalue problem and concatenate the solutions for $\psi^i_{\text{L/R}}$ into a single matrix W. A global solution needs to be continuous at $x = 0$, and it exists if there is a nonzero linear combination of the left mode vectors ψ^i_{L} that is also a linear combination of right mode vectors ψ^i_{R}. We therefore obtain the edge spectrum by numerically finding points in the (E,k) plane where W is singular [25].

This analysis shows that all the continuum models we consider have gapless modes at the boundary between topologically trivial and non-trivial regions protected by mirror symmetry, as shown in Fig. 2.2. Any perturbation that breaks the reflection symmetry opens a gap, even if it preserves all the onsite symmetries. The class D spectrum is representative of the AIII and BDI spectra. The edge modes of the CII model are doubly degenerate due to the combination of its reflection and time-reversal symmetries.

2.4. AMORPHOUS SYSTEMS

In this section we demote the exact spatial symmetries of the continuum models to average symmetries by using tight-binding Hamiltonians on an amorphous graph, and demonstrate that the topological protection by reflection and continuous rotation symmetry persists.

2.4.1. AMORPHOUS TIGHT-BINDING HAMILTONIANS

In order to extract the scaling behaviour of the edges of an amorphous system, we construct real space tight-binding models using the symmetry considerations outlined in Sec. 2.2. While the problem formally looks very similar to the k-space case replacing $\mathbf{k}$ with $\mathbf{d}$, onsite symmetries behave differently in real space:

$$U_{\mathscr{C}}H(\mathbf{d})U_{\mathscr{C}}^{-1} = -H(\mathbf{d}) \tag{2.11}$$

$$U_{\mathscr{P}}H^*(\mathbf{d})U_{\mathscr{P}}^{-1} = -H(\mathbf{d}) \tag{2.12}$$

$$U_{\mathscr{T}}H^*(\mathbf{d})U_{\mathscr{T}}^{-1} = H(\mathbf{d}). \tag{2.13}$$

Hermitian adjoint reverses hoppings, so $H(\mathbf{d})$ is generally nonhermitian, but obeys a modified hermiticity condition:

$$H(-\mathbf{d}) = H(\mathbf{d})^\dagger. \tag{2.14}$$

With these modifications, we use Qsymm to generate all symmetry-allowed hopping terms $H^{\text{hop}}(\hat{\mathbf{d}})$ as first order polynomials of the components of $\hat{\mathbf{d}}$. The hopping terms obtained in this way have a sufficiently general dependence on the bond direction for our purposes. The onsite terms obey the same symmetry conditions as in k-space, so we use the same H^{os} as in the previous section. In order to make the Hamiltonian short-ranged without changing its symmetries, we make the hoppings decay exponentially with bond length, see App. 2.F. Again we consider doubled models in classes AIII, BDI and D, the results are listed in App. 2.E.2.

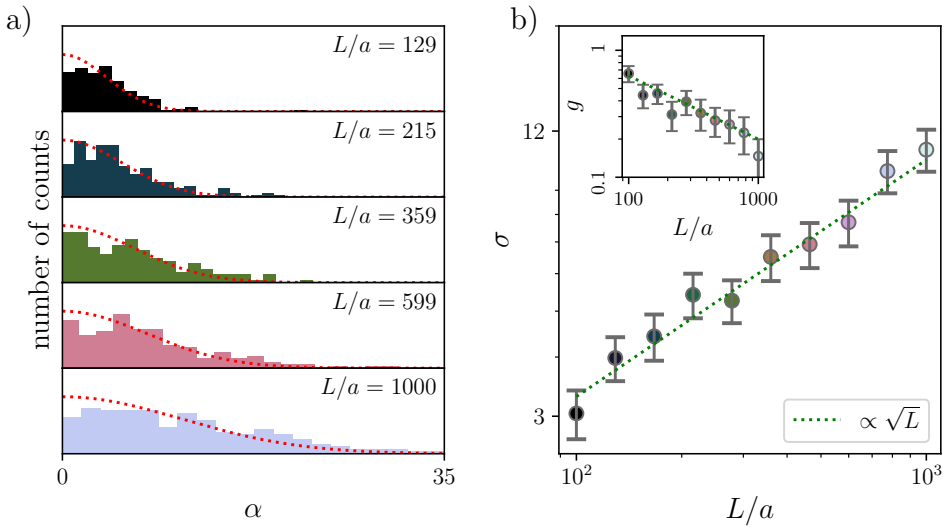

Figuur 2.3: Critical transport scaling for the 8-band class D amorphous system with onsite disorder. a) histogram of α for various system sizes L from 93 different amorphous system realizations. In red: maximum likelihood estimate fit of a half-normal distribution to the data. b) length dependence of σ, the scale parameter of the half-normal fits. Inset: average conductance g as a function of system size. The dashed lines are the $L^{\pm 1/2}$ fit to the scaling data.

2.4.2. TRANSPORT PROPERTIES OF THE AMORPHOUS EDGE

To demonstrate that our amorphous systems are statistical topological insulators, we show that their transport signatures match those of 1D disordered systems at the critical point of a topological phase transition. The transmission amplitudes t_i are random variables that depend on the disorder configuration of the system and the conductivity is given by $g = \sum_i |t_i|^2$ [26]. At the critical point the transmission amplitude distribution universally obeys $\alpha = \text{arccosh}(1/|t|)$ such that α has half-normal distribution with scale parameter σ that grows with the edge length L as $\sigma \propto \sqrt{L}$ [27, 28]. The resulting disorder-averaged conductance has power-law decay $g \propto L^{-1/2}$.

We fit the α_i obtained from numerical transport calculations on edges of the class D amorphous model with various edge lengths for several random realizations of the amorphous system to half-normal distributions (see App. 5.B). The top panel of Fig. 2.3 shows the histograms of α, and the bottom panel shows that we recover the relation $\sigma \propto \sqrt{L}$ for the standard deviation of α and $g \propto L^{-1/2}$ for the conductance. Here we use a model with Gaussian distributed onsite disorder only respecting particle-hole symmetry to show the critical scaling of the conductance g. We expect that allowing the onsite terms to depend on the local environment, as is the case for more detailed models of amorphous matter, would have a similar effect. While we recover the scaling of σ without onsite disorder, we find that the intrinsic disorder from the underlying random graph is too weak to detect the conductance scaling at numerically feasible system sizes, see App. 2.G.

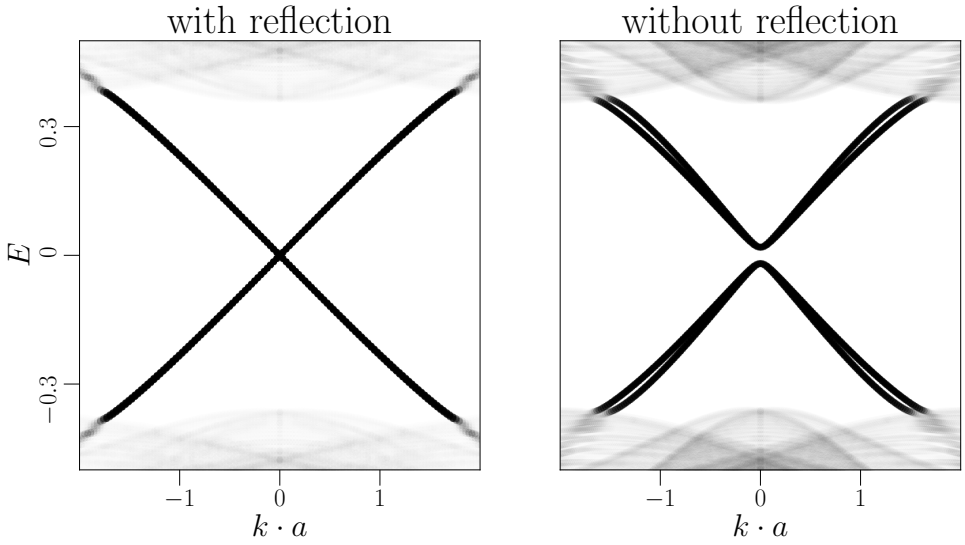

Figuur 2.4: Band structures of the class D model on periodic crystal strips for different edge terminations and distance dependences. The left panel shows bands along the reflection symmetric [1 0] edge, and the right panel shows bands along the [2 1] edge, that breaks reflection symmetry. Transparency of the dispersion bands is directly proportional to their participation ratio. Plot details in App. 2.A and App. 2.F.

2.4.3. ANALOGOUS MODEL ON THE SQUARE LATTICE

The way we defined our hopping Hamiltonians allows us to use them on any graph, including regular crystal lattices. This lets us demonstrate that breaking the rotation and reflection symmetries to a discrete subgroup opens a gap on reflection asymmetric edges. We calculate the band structures of periodic crystal strips whose edges are terminated along different directions and inspect the dispersion of the edge modes spanning the bulk gap.

Using a sufficiently general model on the square lattice that breaks all additional symmetries beyond the onsite and spatial symmetries we prescribe (see App. 2.F) we find that reflection-breaking edges on the square lattice are gapped. Fig. 2.4 compares edges oriented along $[1,0]$ and $[2,1]$, in the first case reflection symmetry of the edge protects gapless modes, while in the second case it does not.

2.5. BULK INVARIANT

We have demonstrated the robustness of gapless edge modes protected by reflection symmetry in both continuum and amorphous systems. In this section we give an explicit invariant characterizing the topological phase without referring to edge properties.

2.5.1. CONTINUUM MODELS

We construct the 2D bulk invariants of the rotation symmetric continuum Hamiltonians from the 1D invariants of the same symmetry class. This is motivated by the fact that the Hamiltonian on any 1D line in k-space specifies the Hamiltonian everywhere in the

2D k-space through rotation symmetry. To relate to 1D invariants defined on a finite Brillouin zone, we require the Hamiltonian to be sufficiently regularized: the eigenvectors of $H(\mathbf{k})$ must become independent of the direction of $\mathbf{k}$ for the limit $|\mathbf{k}| \to \infty$. For example, the quadratic terms of (2.29) dominate the k-space Hamiltonian in this limit, making it insensitive to the signs of k_x and k_y. This allows compactification of the $\mathbb{R}^2$ momentum space of the continuum to a sphere S^2 by identifying all infinitely far points to a single point, which we denote $\mathbf{k} = \boldsymbol{\infty}$. We use a stereographic projection to construct this mapping from $\mathbb{R}^2$ to S^2. The Hamiltonian at $\mathbf{k} = \mathbf{0}$, $\boldsymbol{\infty}$ is invariant under continuous rotations [29, 30] as well as under all reflection symmetries. Furthermore, the Hamiltonian on any line connecting these two points determines the Hamiltonian everywhere on the k-space sphere. Therefore it is natural to think of the momentum space of an amorphous material as a spherical Brillouin zone with North and South poles at $\mathbf{k} = \mathbf{0}, \boldsymbol{\infty}$, an axis of rotation along the $\hat{z}$ axis, and mirror lines on every meridian.

The invariant in 1D class D is $\nu_{\mathrm{D1}} = \mathrm{sign}\left[\mathrm{pf}\, H(k=0) \cdot \mathrm{pf}\, H(k=\pi)\right]$ where pf denotes the Pfaffian and $H(k) = -H(k)^*$ is the class D Hamiltonian in the Majorana basis. This generalizes to the 2D continuum as $\nu_{\mathrm{D2}} = \mathrm{sign}\left[\mathrm{pf}\, H(\mathbf{0}) \cdot \mathrm{pf}\, H(\boldsymbol{\infty})\right]$. This invariant, however, is only nontrivial if the system has nonzero Chern number, because $\exp(i\pi C) = \nu_{\mathrm{D2}}$ [23], which is not possible with mirror symmetry. To define a new invariant in the presence of a unitary mirror symmetry whose eigenvalues are invariant under particle-hole conjugation ($U_M \mathscr{P} = \mathscr{P} U_M$ for $U_M^2 = +\mathbb{1}$, as is the case for the model studied in the manuscript) we apply the above formula to the two reflection sectors separately:

$$\nu_{\mathrm{M}} = \mathrm{sign}\left[\mathrm{pf}\, H_{\pm}(\mathbf{0}) \cdot \mathrm{pf}\, H_{\pm}(\boldsymbol{\infty})\right] \tag{2.15}$$

where $H_{\pm}$ is the Hamiltonian restricted to the ± 1 eigensubspace of U_M. The choice of the reflection sector is arbitrary, as the product of the invariants for the two sectors equals $\nu_{\mathrm{D2}} = +1$.

To prove that a nontrivial bulk invariant corresponds to gapless edge states, we consider a system with a straight edge in the y direction preserving M_y. Restricting to zero momentum along the edge ($k_y = 0$) we get a half-infinite 1D system, whose bulk is described by $H(k_x, 0)$ that is invariant under M_y for every k_x. The bulk invariant derived above is exactly the reflection-resolved strong invariant of the 1D system, indicating zero modes at a real space boundary for each mirror sector in the nontrivial phase. These zero modes correspond to the crossing of the edge modes at $k_y = 0$.

To construct the topological invariant in other symmetry classes, we follow a similar procedure. The topological invariants of odd-dimensional systems with chiral symmetry are winding numbers [5]. Therefore, the bulk invariants of the AIII, BDI, and CII classes is the winding number of a single reflection sector modulo 2. In class DIII$_+$ we construct a reflection-resolved $\mathbb{Z}_2$ invariant analogous to the class DIII Pfaffian invariant. We summarize the resulting classification of topological phases protected by unitary reflection and continuous rotation symmetry in continuum and amorphous systems in Table 2.2. Because the topological invariant is an integral along a high-symmetry line in k-space, these expressions coincide with the topological invariants of reflection-protected phases in crystalline materials [31–33].

Symmetry class	continuum	amorphous
AIII	$\mathbb{Z}$	$\mathbb{Z}_2$
BDI	$\mathbb{Z}$	$\mathbb{Z}_2$
D	$\mathbb{Z}_2$	$\mathbb{Z}_2$
DIII$_+$	$\mathbb{Z}_2$	$\mathbb{Z}_2$
DIII$_-$	$2\mathbb{Z}$	0
CII	$2\mathbb{Z}$	$2\mathbb{Z}_2$

Tabel 2.2: Classification of topological phases in continuum and amorphous systems protected by continuous rotation and unitary reflection symmetry. The classification does not include the strong 2D invariant that is an independent $\mathbb{Z}_2$ invariant in class DIII$_-$. In all other classes reflection symmetry enforces a trivial strong invariant. For details on how disorder leads to the distinction between the continuum and amorphous classification, see App. 2.H.

2.5.2. EFFECTIVE HAMILTONIAN OF AMORPHOUS MODELS

Without translation invariance it is still possible to detect the bulk gap closings that accompany topological phase transitions through the density of states $\rho(E) = N^{-1}\,\mathrm{tr}\,\delta(\hat{H}-E)$ of a large finite system with N sites. Fig. 2.5 (a) shows the density of states of the class D amorphous model as the chemical potential μ is tuned across two phase transitions. We observe two bulk gap closings, and a small constant density of states in the bulk gap due to edge states in the topological phase. To gain even more insight, we introduce the momentum-resolved spectral function

$$A(\mathbf{k},E) = \sum_n \langle \mathbf{k},n|\,\delta\big(\hat{H}-E\big)\,|\mathbf{k},n\rangle\,,\ \text{with}\ \langle \mathbf{r},n|\mathbf{k},m|\mathbf{r},n|\mathbf{k},m\rangle = N^{-1/2}\exp(i\mathbf{k}\mathbf{r})\delta_{nm}, \quad (2.16)$$

so that $|\mathbf{k},n\rangle$ is a plane-wave state localized in the n'th orbital. We use the spectral function with momentum parallel to the edge to detect edge states in finite samples, as shown in Fig. 2.1. It is also well defined in the $\mathbf{k}\to\boldsymbol{\infty}$ limit: because our amorphous samples are isotropic and the sites are always separated by a finite distance (see App. 5.B), the relative phase on each bond in the plane wave converges to a uniform independent random phase. Fig. 2.5 (b) and (c) show that the two gap closings observed earlier are different: one occurs at $\mathbf{k}=\mathbf{0}$ and the other at $\mathbf{k}=\boldsymbol{\infty}$.

In order to apply the construction of bulk invariants to amorphous systems, we introduce the effective k-space Hamiltonian [17, 23] $H_{\mathrm{eff}}(\mathbf{k}) = G_{\mathrm{eff}}(\mathbf{k})^{-1}$ through the projection of the single-particle Green's function onto plane-wave states:

$$G_{\mathrm{eff}}(\mathbf{k})_{m,n} = \langle \mathbf{k},m|\,\hat{G}\,|\mathbf{k},n\rangle\,, \quad (2.17)$$

where $\hat{G} = \lim_{\eta\to 0}(\hat{H}+i\eta)^{-1}$ is the Green's function of the full real space Hamiltonian $\hat{H}$. Fig. 2.5 shows the relation to $A(\mathbf{k},E)$. The spectrum of $H_{\mathrm{eff}}(\mathbf{k})$ closely follows the peaks of the spectral function, especially near the gap closing points. The key properties of H_{eff} are that it transforms the same way under symmetries as continuum Hamiltonians discussed before, its gap only closes when the gap in the bulk $\hat{H}$ closes [23], and it is properly regularized in the $\mathbf{k}\to\boldsymbol{\infty}$ limit [17]. Hence, the bulk invariants defined for continuum systems are directly applicable to detecting topological phase transitions in amorphous systems. We show in Fig. 2.5 (d) for the class D amorphous model that the bulk invariant is non-trivial ($\nu_M = -1$) for intermediate values of the chemical potential.

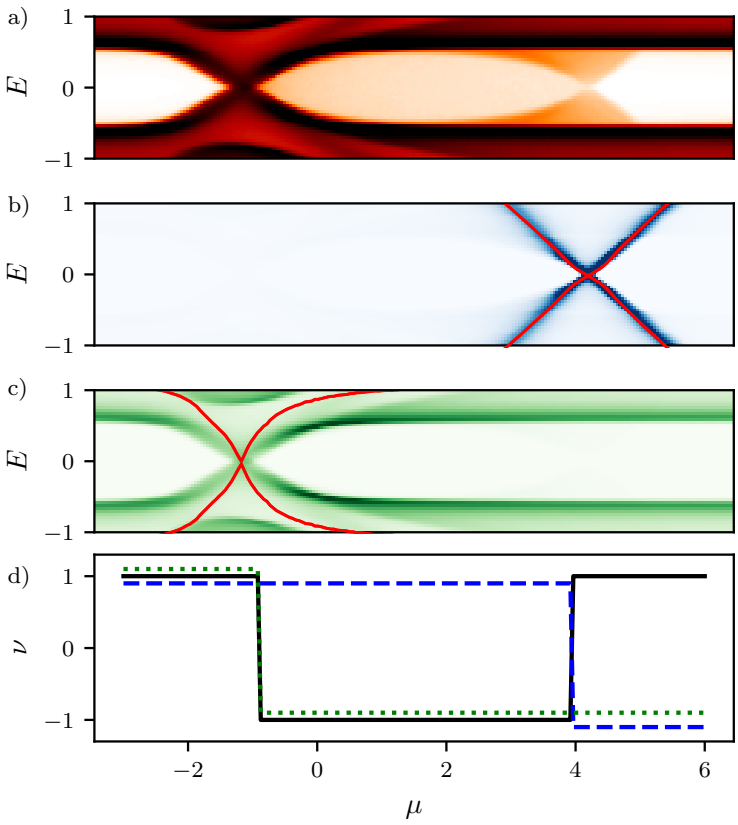

Figuur 2.5: Topological phase transitions of the amorphous class D model as a function of the chemical potential. (a) Density of states of a finite amorphous sample. Darker color indicates higher density. (b) Spectral function at $\mathbf{k} = \mathbf{0}$ of a finite amorphous sample. The spectrum of the effective Hamiltonian is overlaid in red. (c) Same as (b) but at $\mathbf{k} = \boldsymbol{\infty}$. (d) Topological invariant ν_M (solid line). The dashed and dotted lines correspond to $\text{sign}[\text{pf}\, H_+^{\text{eff}}(\mathbf{0})]$ and $\text{sign}[\text{pf}\, H_+^{\text{eff}}(\boldsymbol{\infty})]$ respectively, offset along the vertical axis for visual clarity.

2.6. CONCLUSIONS AND DISCUSSION

We introduced statistical topological insulator phases in two-dimensional amorphous systems that rely on average spatial symmetries for protection. We demonstrated that in the non-trivial phase the edge behaves as a 1D critical system of the same symmetry class by observing power-law scaling of the transport properties. We found topological invariants characterizing the bulk, and showed that the critical edge physics is not a result of fine-tuning, but is protected by the average reflection symmetry that is present on all straight edges of amorphous samples.

Comparing our results to similar work on higher-order topological insulators in quasicrystals protected by eight and twelvefold rotation symmetry [23, 34, 35] raises a natural question: can the amorphous phases protected by continuous rotation symmetry be described as a limit of systems with increasingly fine discrete rotation symmetry? It also

remains an open question how to extend the topological classification to materials with multiple atom species.

Superconductivity is known to exist in amorphous thin films [36]. In the cases where we found new amorphous topological phases, however, the reflection symmetry commutes with time-reversal and particle-hole symmetry, while the physical reflection symmetry of s-wave superconductors anticommutes with onsite unitary symmetries. Hence condensed matter realizations of these symmetry classes are only feasible in the presence of reflection-odd (e.g. p-wave) pairing. It is possible that favourable energetics can result in an effective chiral symmetry, but such materials would be highly fine-tuned. Shiba glass systems consisting of atoms randomly deposited on surfaces have also been proposed as a platform for two-dimensional amorphous topological superconductivity [14]. Engineered systems, so called "topological simulators", can serve as an experimental demonstration of the phenomena studied in this work: the amorphous class BDI model could be naturally realized in disordered acoustic and mechanical meta-materials [37–39], while the other symmetry classes may be realized in a variety of systems including ultracold atoms [40], photonic crystals [41, 42], or coupled electronic circuit elements [43].

Our findings pave the way for a new classification of amorphous systems. Because the symmetry groups generated by continuous rotations are non-abelian in dimensions $d > 2$, we expect even richer topological classification in higher dimensions.

2.A. MODEL AND PLOTTING PARAMETERS

The data shown in the figures, as well as the code generating all of the data is available at [44]. In this section additional details of the plots are listed, if any, in order of appearance.

For Fig. 2.1, f from (2.47) is set to 0.2 for o_1 and o_4 of (2.44). The data was obtained for systems containing 2500 sites.

The bottom panels of Fig. 2.2 are obtained by adding mirror-breaking terms to the continuum Hamiltonian models.

Fig. 2.3 is obtained from the class D model with added Gaussian noise terms that conserve particle-hole symmetry exactly. The amplitude of the noise terms γ_i is $\frac{\gamma_i}{\mu} = 0.3 * x_i$ with x_i a random number from a normal distribution with mean 0 and standard deviation 1, and μ the chemical potential of the topological sector of the model. The number of sites in the system vary from 5000 to 50000.

The data presented in Fig. 2.4 and 2.6 is obtained with $f = 0.2$ or $f = 1$ (as indicated) for the hopping terms o_1 and o_4 of (2.44). The periodic strips all have a width of 100 sites in the non-periodic direction.

Fig. 2.5 was obtained from a system with 40000 sites.

Fig. 2.7 is obtained with $f = 1.5$ for the hopping terms t and d of (2.39) of the non-trivial and trivial sectors of the AIII model respectively, and o_4 of (2.40). The class BDI data is obtained with $f = 0.7$ for t of (2.41) of the non-trivial sector, and o_2 from (2.42). The class CII data is obtained with $f = 0.7$ for t_1 and t_4 of (2.45). The class DIII data is obtained with $f = 2$ for o_1 and o_4 of (2.46). The periodic strips all have a width of 100 sites in the non-periodic direction.

Fig. 2.8 was obtained from the class D model by setting $f = 0.7$ for hopping terms t_1, d_2 and o_4 of (2.43) and (2.44). The number of sites in the system vary from 5000 to 50000.

Fig. 2.9 was obtained from systems with 100 sites and Fig. 2.10 was obtained from systems with 2500 sites.

2.B. NUMERICAL METHODS

In the numerical calculations we use hard-disk amorphous structures [21]. To generate a structure, we randomly add atomic sites in a fixed volume from an uncorrelated uniform distribution. Treating atoms as hard disks, we reject new sites closer than a fixed distance to existing sites, and this procedure is performed until the goal density is reached. This procedure reduces density fluctuations and avoids sites that are very close to each other, matching the distance distribution function of a realistic amorphous system more closely than independent uniformly distributed points. We include hopping terms in the Hamiltonian for bonds connecting each site to a maximum number of N neighbours falling within a maximum bond length R. The values of N and R are chosen such that the exponentially decaying hopping amplitudes to further neighbours can be safely neglected, resulting in a sparse Hamiltonian.

We use the software package Kwant [45] to generate the lattice Hamiltonians and for transport calculations. The transmission eigenvalues are obtained via the calculation of the scattering matrix using Kwant. The transmission amplitudes t_i are given by the singular values of the transmission block of the scattering matrix. Pfaffians are calculated using Pfapack [46]. The numerical density of states, momentum-resolved spectral function, and effective Hamiltonian calculations are performed using the kernel polynomial method [17, 23, 47, 48].

2.C. COMMUTATION RELATIONS OF THE SYMMETRY OPERATORS

In real space, conjugating a rotation with a mirror results in a rotation in the opposite direction:

$$MR(\phi)M^{-1} = R(-\phi). \tag{2.18}$$

Demanding that there are no nontrivial onsite unitary symmetries, this implies for the unitary parts that

$$U_M e^{i\phi S_z} U_M^{-1} e^{i\phi S_z} = e^{i\alpha(\phi)}\,\mathbb{1}. \tag{2.19}$$

Differentiating with respect to ϕ and setting $\phi = 0$ yields

$$U_M S_z U_M^{-1} = -S_z + \alpha'\,\mathbb{1} \tag{2.20}$$

where $\alpha' = d\alpha/d\phi|_{\phi=0}$. As the spectra of the two sides need to be equal, and the spectrum of S_z consists of only integer or half-integer values, we find that $\alpha' \in \mathbb{Z}$. Redefining $S_z \to S_z - (\alpha'/2)\,\mathbb{1}$ the symmetry constraint on the Hamiltonian does not change, and we find that S_z and U_M anticommute. This also implies that the spectrum of S_z is symmetric and $\operatorname{tr} S_z = 0$, which is also a sufficient condition for the anticommutation with U_M, hence we assume $\operatorname{tr} S_z = 0$ in the rest of the manuscript without loss of generality. Similar calculation shows that discrete onsite antiunitary (anti)symmetries (particle-hole and time-reversal) anticommute with S_z, and chiral symmetry commutes with S_z in the absence of unitary symmetries.

Symmetry class	U_M	$U_{\mathscr{P}}$	$U_{\mathscr{T}}$
A	τ_0	-	-
AI	τ_0	-	τ_x
D	τ_0	τ_0	-
AII	$\sigma_0\tau_0$	-	$\sigma_0\tau_y$
C	$\sigma_0\tau_0$	$\sigma_0\tau_y$	0

Tabel 2.3: Symmetry representations of 1D models where a reflection antisymmetry (that anticommutes with the Hamiltonian) with unitary part U_M protects gapless edges. σ and τ are Pauli matrices. Only unitary-inequivalent symmetry representations are listed.

Symmetry class	U_M	$U_{\mathscr{P}}$	$U_{\mathscr{T}}$	$U_{\mathscr{C}}$	S_z
AIII	$\sigma_x\tau_y$	-	-	$\sigma_x\tau_0$	$\frac{1}{2}\sigma_0\tau_z$
BDI	$\sigma_x\tau_x$	$\sigma_0\tau_x$	$\sigma_x\tau_x$	$\sigma_x\tau_0$	$\frac{1}{2}\sigma_0\tau_z$
CII	$\rho_y\sigma_y\tau_y$	$i\rho_z\sigma_y\tau_0$	$i\rho_z\sigma_0\tau_y$	$\rho_0\sigma_y\tau_y$	$\frac{1}{2}\rho_z\sigma_0\tau_y$
D	$\sigma_x\tau_x$	$\sigma_0\tau_x$	-	-	$\frac{1}{2}\sigma_0\tau_z$
DIII_	$\rho_z\sigma_x\tau_z$	$\rho_x\sigma_0\tau_z$	$i\rho_x\sigma_z\tau_y$	$\rho_0\sigma_z\tau_x$	$\frac{1}{2}\rho_0\sigma_y\tau_z$

Tabel 2.4: Symmetry representations of 2D bulk models with unitary reflection and rotation symmetry. ρ, σ and τ are Pauli matrices. The chemical potential terms are $\mu\sigma_z\tau_z$ for the 4-band models, $\mu\rho_z\sigma_z\tau_0$ for CII and $\mu\rho_z\sigma_0\tau_z$ for DIII.

2.D. DETAILS OF SYMMETRY REPRESENTATIONS

Besides the unitary mirror symmetries listed in the main text, we find several cases where a reflection antisymmetry (an operator that reverses k and the energy) protects gapless edge states in continuum models. Since combinations of the reflection-like symmetry with any of the onsite symmetries is also a reflection-like symmetry providing the same protection, we omit such repetitions when listing the results in Table 2.3. We consider the results in classes A, AI and AII an artefact of using continuum models with perfect translation invariance, and expect that these are not viable for an amorphous system since they localize in the presence of disorder that makes the reflection antisymmetry only an average symmetry [49].

The result of the search for 2D symmetry representations compatible with the edge symmetries is not unique: we pick one of several unitary equivalent choices for each Altland-Zirnbauer symmetry class. The specific forms of the symmetry representations that define the models in App. 2.E are listed in Table 2.4.

For the 4-band models, we define the basis space of the unitary parts of the symmetry operators as the direct product $\sigma \otimes \tau$, with σ and τ as Pauli matrices in sublattice and spin space respectively, such that the chemical potential terms of the models are $\mu\sigma_z\tau_z$. For the 8-band models, the basis space is extended to $\rho \otimes \sigma \otimes \tau$, where ρ is also a Pauli matrix. For the doubled AIII, BDI and D models we extend the symmetries by multiplying with $\rho_0 = \mathbb{1}_2$.

2.E. MODEL HAMILTONIANS

2.E.1. CONTINUUM HAMILTONIANS

The onsite Hamiltonians in both the continuum and amorphous bulk models are given by:

$$H^{\text{os}}_{\text{AIII}} = \mu\sigma_z\tau_z + \lambda\sigma_y\tau_z \tag{2.21}$$
$$H^{\text{os,c}}_{\text{AIII}} = \lambda_1\sigma_z\tau_z + i\lambda_2\sigma_y\tau_z \tag{2.22}$$
$$H^{\text{os}}_{\text{BDI}} = \mu\sigma_z\tau_z \tag{2.23}$$
$$H^{\text{os,c}}_{\text{BDI}} = \lambda_1\sigma_z\tau_z + i\lambda_2\sigma_y\tau_z \tag{2.24}$$
$$H^{\text{os}}_{\text{D}} = \mu\sigma_z\tau_z \tag{2.25}$$
$$H^{\text{os,c}}_{\text{D}} = \lambda_1\sigma_z\tau_z + i\lambda_2\sigma_0\tau_0 \tag{2.26}$$
$$H^{\text{os}}_{\text{CII}} = \mu\rho_z\sigma_z\tau_0 + \lambda_1\rho_z\sigma_x\tau_0 + \rho_x\sigma_0\cdot(\lambda_2\tau_z + \lambda_3\tau_x) \tag{2.27}$$
$$H^{\text{os}}_{\text{DIII}} = \mu\rho_z\sigma_0\tau_z + \lambda_1\rho_y\sigma_y\tau_0 + \lambda_2\rho_x\sigma_x\tau_x + \lambda_3\rho_z\sigma_z\tau_y + \lambda_4\rho_x\sigma_y\tau_0 + \lambda_5\rho_y\sigma_y\tau_y \tag{2.28}$$

where the Pauli matrices σ and τ act on the electron-hole and the angular momentum degrees of freedom respectively. In the doubled models we assign different parameter values in the two diagonal blocks.

The doubled k-space models have the following hopping terms:

$$H^{\text{hop}}_{\text{AIII}}(\mathbf{k}) = t_n\sigma_z\tau_z(k_x^2+k_y^2) + (t1\sigma_z - t_2\sigma_y)\tau_x k_x + (t_1\sigma_z + t_2\sigma_x)\tau_y k_y \tag{2.29}$$
$$H^{\text{hop,c}}_{\text{AIII}}(\mathbf{k}) = (\beta_1\sigma_z + \beta_2\sigma_y)\tau_x k_x + (\beta_1\sigma_z + \beta_2^*\sigma_y)\tau_y k_y \tag{2.30}$$

$$H^{\text{hop}}_{\text{BDI}}(\mathbf{k}) = t_n\sigma_z\tau_z(k_x^2+k_y^2) + t\sigma_z(\tau_x k_x + \sigma_z\tau_y k_y) \tag{2.31}$$
$$H^{\text{hop,c}}_{\text{BDI}}(\mathbf{k}) = o_1\sigma_z(\tau_x k_x + \tau_y k_y) + io_2\sigma_y(\tau_x k_x + \tau_y k_y) \tag{2.32}$$

$$H^{\text{hop}}_{\text{D}}(\mathbf{k}) = t_n\sigma_z\tau_z(k_x^2+k_y^2) + t_1\sigma_z(\tau_x k_x + \tau_y k_y) \tag{2.33}$$
$$+ t_2\sigma_0(-\tau_y k_x + \tau_x k_y)s + d\sigma_x(\tau_x k_x + \tau_y k_y) \tag{2.34}$$
$$H^{\text{hop,c}}_{\text{D}}(\mathbf{k}) = io_1\sigma_y(\tau_x k_x + \tau_y k_y) + o_2\sigma_z(\tau_x k_x + \tau_y k_y) \tag{2.35}$$
$$+ o_3\sigma_x(-\tau_y k_x + \tau_x k_y) + o_4\sigma_0(-\tau_y k_x + \tau_x k_y) \tag{2.36}$$

The k-space CII and DIII models have hopping terms of the form:

$$H^{\text{hop}}_{\text{CII}}(\mathbf{k}) = t_n\rho_z\sigma_z\tau_0(k_x^2+k_y^2) + t_1(\rho_z\sigma_z\tau_z k_x + \rho_0\sigma_0\tau_x k_y) + t_2(\rho_z\sigma_0\tau_x k_x - \rho_0\sigma_0\tau_z k_y) + t_3(\rho_x\sigma_0\tau_0 k_x + \rho_y\sigma_z\tau_y k_y) + t_4(\rho_x\sigma_x\tau_0 k_x + \rho_y\sigma_x\tau_y k_y) \tag{2.37}$$

$$H^{\text{hop}}_{\text{DIII}}(\mathbf{k}) = t_n\rho_z\sigma_0\tau_z(k_x^2+k_y^2) + d\rho_0\sigma_y\tau_x k_x + \rho_0\sigma_0\tau_y k_y) + t(-\rho_0\sigma_x\tau_0 k_x + \rho_0\sigma_z\tau_z k_y) + o_1(\rho_y\sigma_z\tau_z k_x + \rho_y\sigma_0\tau_0 k_y) + o_2(\rho_x\sigma_0\tau_y k_x + \rho_x\sigma_y\tau_0 k_y) + o_3(\rho_x\sigma_z\tau_z k_x + \rho_x\sigma_x\tau_0 k_y) + o_4(\rho_y\sigma_0\tau_y k_x - \rho_y\sigma_y\tau_x k_y). \tag{2.38}$$

2.E.2. REAL SPACE HAMILTONIANS

For the real-space models the onsite Hamiltonian are identical to the onsite terms found in the previous section.

The double model hopping Hamiltonians have the form:

$$H^{\text{hop}}_{\text{AIII}}(\hat{\mathbf{d}}) = t_n\sigma_z\tau_z + it\sigma_z(\tau_x d_x + \tau_y d_y) + id\sigma_y(\tau_x d_x + \tau_y d_y) \tag{2.39}$$

$$\begin{aligned} H^{\text{hop,c}}_{\text{AIII}}(\hat{\mathbf{d}}) = {} & o_1\sigma_z(i\tau_x d_x + i\tau_y d_y) + o_2\sigma_0(i\tau_y d_x + i\tau_x d_y) \\ & + o_3\sigma_y(\tau_x d_x + \tau_y d_y) + o_4\sigma_x(-i\tau_y d_x + i\tau_x d_y) \end{aligned} \tag{2.40}$$

$$H^{\text{hop}}_{\text{BDI}}(\hat{\mathbf{d}}) = t_n\sigma_z\tau_z + it\sigma_z(\tau_x d_x + \tau_y d_y) \tag{2.41}$$

$$H^{\text{hop,c}}_{\text{BDI}}(\hat{\mathbf{d}}) = io_1\sigma_z(\tau_x d_x + \tau_y d_y) + io_2\sigma_y(\tau_x d_x - \tau_y d_y) \tag{2.42}$$

$$\begin{aligned} H^{\text{hop}}_{\text{D}}(\hat{\mathbf{d}}) = {} & t_n\sigma_z\tau_z + it_1\sigma_z(\tau_y d_x - \tau_x d_y) \\ & + it_2\sigma_0(\tau_x d_x + \tau_y d_y) + id\sigma_x(\tau_x d_x + \tau_y d_y) \end{aligned} \tag{2.43}$$

$$\begin{aligned} H^{\text{hop,c}}_{\text{D}}(\hat{\mathbf{d}}) = {} & io_1\sigma_z(\tau_x d_x + \tau_y d_y) + io_2\sigma_y(\tau_x d_x + \tau_y d_y) \\ & + io_3\sigma_x(\tau_y d_x + \tau_x d_y) + io_4\sigma_0(\tau_y d_x - \tau_x d_y). \end{aligned} \tag{2.44}$$

The 8-band CII and DIII models have hopping terms:

$$\begin{aligned} H^{\text{hop}}_{\text{CII}}(\hat{\mathbf{d}}) = {} & t_n\rho_z\sigma_z\tau_0 + it_1(\rho_z\sigma_0\tau_z d_x + \rho_0\sigma_0\tau_x d_y) \\ & + it_2(\rho_z\sigma_0\tau_x d_x - \rho_0\sigma_0\tau_z d_y) + it_3(\rho_x\sigma_z\tau_0 d_x + \rho_y\sigma_z\tau_y d_y) \\ & + it_4(\rho_x\sigma_x\tau_0 d_x + \rho_y\sigma_x\tau_y d_y) \end{aligned} \tag{2.45}$$

$$\begin{aligned} H^{\text{hop}}_{\text{DIII}}(\hat{\mathbf{d}}) = {} & t_n\rho_z\sigma_0\tau_z + id(\rho_0\sigma_y\tau_x d_x + \rho_0\sigma_0\tau_y d_y) \\ & + it(-\rho_0\sigma_x\tau_0 d_x + \rho_0\sigma_z\tau_z d_y) + io_1(\rho_y\sigma_z\tau_z d_x + \rho_y\sigma_0\tau_0 d_y) \\ & + io_2(\rho_x\sigma_0\tau_y d_x + \rho_x\sigma_y\tau_0 d_y) + io_3(\rho_x\sigma_z\tau_z d_x + \rho_x\sigma_x\tau_0 d_y) \\ & + io_4(\rho_y\sigma_0\tau_y d_x - \rho_y\sigma_y\tau_x d_y). \end{aligned} \tag{2.46}$$

2.F. REMOVING ADDITIONAL SYMMETRIES OF SQUARE LATTICE MODELS

We find that because the nearest-neighbour square lattice is bipartite, it has inherent sublattice (chiral) symmetry that stabilizes an additional pair of counter-propagating edge modes at $k = \pi$. When studying models on the square lattice, we include second and third nearest-neighbour bonds to remove this chiral symmetry and the additional modes.

We find that if every hopping decays the same way with the bond length, even the edges of a crystalline sample that break reflection behave like the edge of a fully isotropic continuum sample that has protected modes for every orientation close to $k = 0$. Hence without changing the symmetry properties we include a different decay constant in the prefactor for each term:

$$H^{\text{hop}}(\mathbf{d}) = \sum_i e^{-f_i\cdot|\mathbf{d}|}\alpha_i H^{\text{hop}}_i(\hat{\mathbf{d}}) \tag{2.47}$$

where i runs over the linearly independent hopping terms [24] in $H^{\text{hop}}(\hat{\mathbf{d}}) = \sum_i \alpha_i H^{\text{hop}}_i(\hat{\mathbf{d}})$. Fig. 2.6 and Fig. 2.7 illustrate the importance of this consideration.

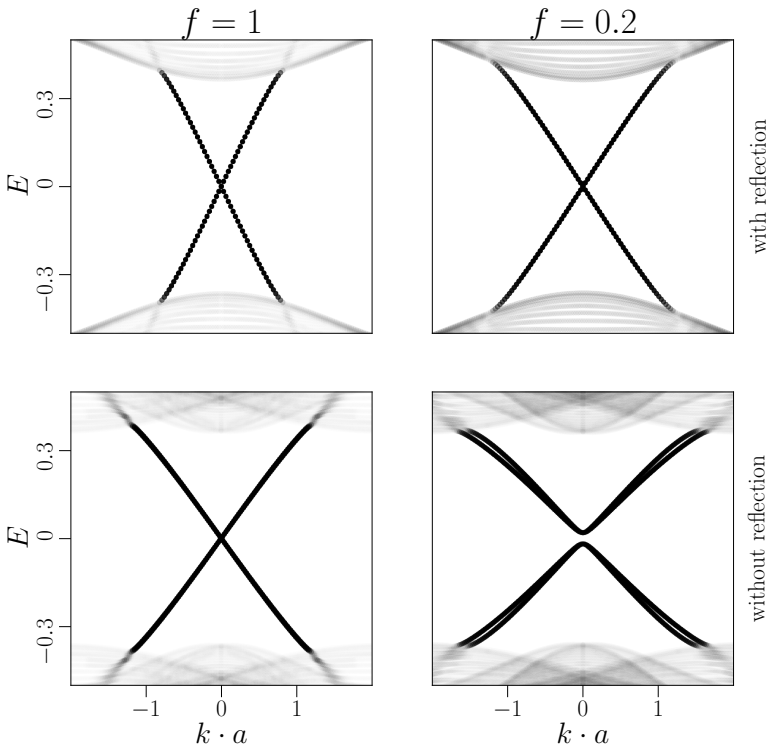

Figuur 2.6: Band structures of the class D model on periodic crystal strips for different edge terminations and distance dependences. Top panels are bands along the reflection symmetric [1 0] edge, and bottom panels are bands along the reflection asymmetric [2 1] edge. Transparency of the dispersion bands is directly proportional to their participation ratio $\sum_i |\psi_i|^4$, where ψ_i is the real space wavefunction of site i of the system. Plot details in App. 2.A.

The band structures of the chiral class models are all gapped for edge orientations that break reflection symmetry, as seen in Fig. 2.7. For the class AIII model, Fig. 2.7 shows that the case is similar to the class D crystal bands: the more general distance dependence (absence of a global prefactor related to the bond lengths before each of the hopping terms) is required to open the gap along reflection asymmetric edges. For the class BDI model, the reflection asymmetric edges are gapped even without the more general distance dependence, as seen in Fig. 2.7, but it does increase the size of the gap. The situation is similar for the CII model, where the more general distance dependence of the hopping opens a gap only on reflection asymmetric edges.

2.G. TRANSPORT SCALING

Fig. 2.8 shows the transport scaling of the class D amorphous model without onsite disorder. The scaling arises from the intrinsic noise of the random graph. The bottom panel shows that we recover the relation $\sigma \propto \sqrt{L}$ for the standard deviation of α. The conductance data in the inset shows that the noise due to the physical randomness of the

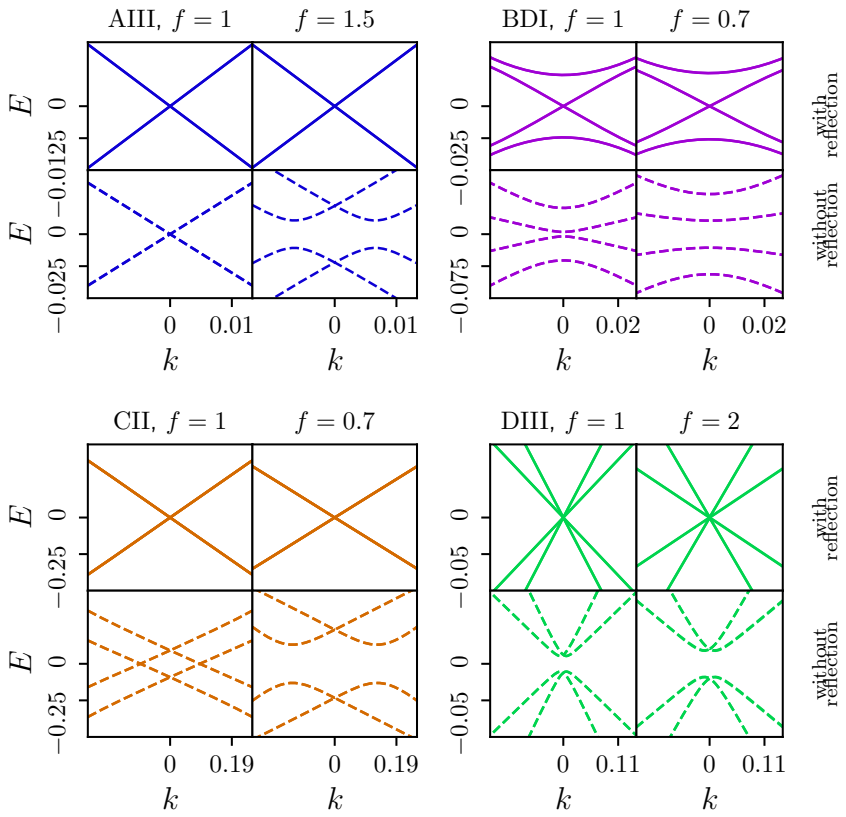

Figuur 2.7: Band structures of the chiral models on periodic crystal strips for different edge terminations and hopping relations. Solid lines indicate bands recorded along the reflection symmetric [1 0] edge, and dashed lines along the reflection asymmetric [2 1] edge. The different hopping relations are distinguished by different values of f from (2.47), see App. 2.F.

amorphous system has a much weaker effect on localizing the modes compared to the noise originating from terms added to the model as in Fig. 2.3. The conductance relation $g \propto L^{-1/2}$ is not recoverable with the numerically accessible edge lengths, as it is only valid for $g \ll 1$.

2.H. BULK INVARIANT FOR CHIRAL CLASSES

In this section we construct invariants classifying continuum and amorphous systems protected by continuous rotation and unitary reflection symmetry.

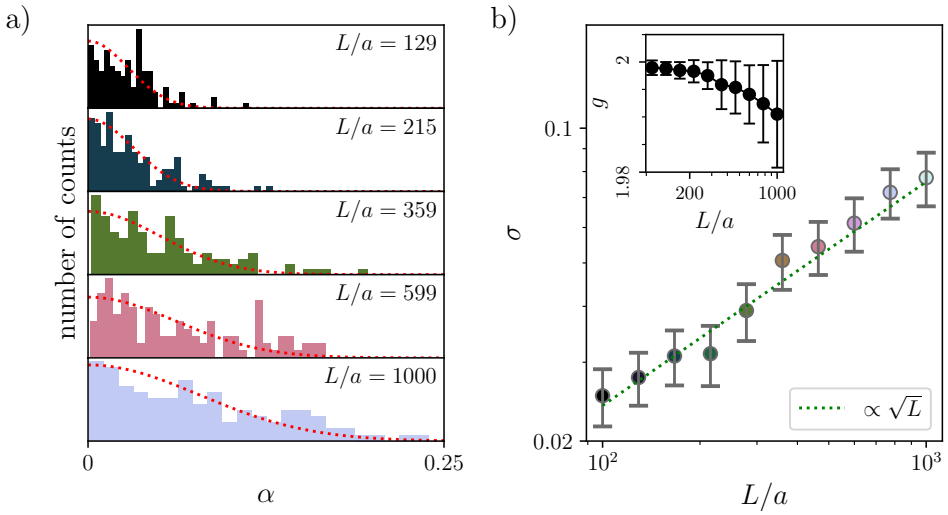

Figuur 2.8: Critical transport scaling for the 8-band class D amorphous system without onsite disorder. Top panel: histogram of α for various system sizes L from 59 different amorphous system realizations. In red: maximum likelihood estimate fit of a half-normal distribution to the data. Bottom panel: length dependence of σ, the square root of the scale factors of the half-normal fits. Inset: average conductance g as a function of system size. The dashed line indicates the $L^{1/2}$ fit to the data.

2.H.1. CLASSES AIII, BDI AND CII

In the presence of chiral symmetry, the band-flattened Hamiltonian $Q(\mathbf{k})$ can be rearranged into two off-diagonal blocks in the basis where $\mathscr{C} = \tau_z$ [3, 5]:

$$Q(\mathbf{k}) = \begin{pmatrix} 0 & q(\mathbf{k}) \\ q^\dagger(\mathbf{k}) & 0 \end{pmatrix}. \tag{2.48}$$

As $[S_z, \mathscr{C}] = 0$ we can simultaneously diagonalize the two operators and choose $S_z = s_z \tau_z$ where s_z is diagonal. A mirror operator U_M anticommutes with S_z and we fix $U_M^2 = +\mathbb{1}$ in the following, this can always be achieved by choosing its overall phase. A mirror either commutes or anticommutes with $\mathscr{C}$, here we assume $[U_M, \mathscr{C}] = 0$ as we found in Sec. 2.3.1 that all symmetry groups protecting gapless edges have this property. In this case U_M takes a block-diagonal form with diagonal blocks m and m', both of which square to $+\mathbb{1}$ and anticommute with s_z, guaranteeing that the spectrum of s_z is symmetric. Because of this, m (also m') is only nonzero between opposite s_z eigenvalues, an appropriately chosen block-diagonal basis transformation that preserves the form of $\mathscr{C}$ and S_z makes it proportional to σ_x in each $|s_z|$ sector. Hence there is always a basis where $m = m' = \sigma_x \otimes \mathbb{1}$ and the symmetry constraint is $m\, q(\mathbf{k})\, m^{-1} = q(R_M \mathbf{k})$.

This allows to decompose $q(\mathbf{k})$ into even/odd mirror sectors $q_\pm(\mathbf{k})$ with respect to a mirror operator that leaves $\mathbf{k}$ invariant [50], and to assign an individual winding number along a mirror-invariant line:

$$n_\pm = -\frac{1}{2\pi} \int_{-\infty}^{\infty} dk \frac{d}{dk} \arg\det q_\pm(k\hat{\mathbf{n}}) \tag{2.49}$$

where the sectors are with respect to the reflection operator with normal orthogonal to $\hat{\mathbf{n}}$. Due to the regularization of the Hamiltonian the integral is along a closed loop, hence quantized to integers, $n_\pm \in \mathbb{Z}$. The twofold rotation symmetry $C_2 = \exp\left(i\frac{\pi}{2}S_z\right)$ reverses $\mathbf{k}$ and for integer or half-integer spin commutes or anticommutes with U_M respectively. For the integer case this means for the winding numbers that $n_+ = n_- = 0$ making the invariant trivial, while in the half-integer case $n_+ = -n_-$ meaning that the total winding n vanishes. So in the half-integer S_z case we can select either one of the reflection-resolved windings to define a nontrivial topological invariant $n_M = \pm n_\pm$. As argued in Sec. 2.5.1 this implies the presence of n_M zero modes in each mirror sector at $k = 0$ on any straight edge. In class CII time reversal symmetry imposes Kramers-degeneracy making n_M even.

The winding number invariant we found for continuum systems is integer valued, suggesting that it is possible for the edge to host more than one pair of counter-propagating modes. In the presence of disorder, however, an even multiple of the minimum number of symmetry-allowed counter-propagating mode pairs always localizes [11]. In classes AIII and BDI (CII) this renders edges of systems with even n_M ($n_M/2$) insulating, and those with odd n_M ($n_M/2$) indistingushable through transport probes. Therefore, rather than the winding number $n_M \in \mathbb{Z}$ itself being our invariant for amorphous systems, we identify its parity $\nu_M \in \mathbb{Z}_2$ as the mirror invariant in classes AIII and BDI:

$$\nu_M = n_M \bmod 2, \tag{2.50}$$

and the parity of half of $n_M \in 2\mathbb{Z}$ in class CII:

$$\nu_M = \frac{n_M}{2} \bmod 2. \tag{2.51}$$

We calculate the $\mathbb{Z}_2$ invariant for the effective Hamiltonian of the amorphous models in all the chiral symmetry classes as the chemical potential μ is tuned across two topological phase transitions, the result is shown in Fig. 2.9. For the numerical calculation we discretize the integral in equation (2.49) as

$$n_M \approx -\frac{1}{2\pi}\sum_i \operatorname{Im}\log\left(\frac{\det q_\pm(k_{i+1}\hat{\mathbf{n}})}{\det q_\pm(k_i\hat{\mathbf{n}})}\right) \tag{2.52}$$

where k_i is a discrete set of k-values in increasing order and with cyclic indexing. To address numerical integration to infinity, we choose the parametrization $k = \tan(\phi/2)$ where ϕ corresponds to the latitude in stereographic projection ranging from $-\pi$ to π. We use 10 evenly spaced values for ϕ in the numerical calculations, we show the results in Fig. 2.9.

2.H.2. CLASS DIII

In this section we show that the above invariant, while well defined in classes $\mathrm{DIII}_\pm$, in class DIII_+ it always vanishes, and in class DIII_- its parity is determined by the strong $\mathbb{Z}_2$ invariant of class DIII. For class DIII_+ we introduce a different $\mathbb{Z}_2$ invariant that is independent of the strong invariant.

We start by deriving general symmetry constraints. We choose the onsite symmetry representation as $\mathscr{C} = \tau_z$, $\mathscr{T} = \tau_y\mathscr{K}$ and $\mathscr{P} = \tau_x\mathscr{K}$, in this basis the Hamiltonian has

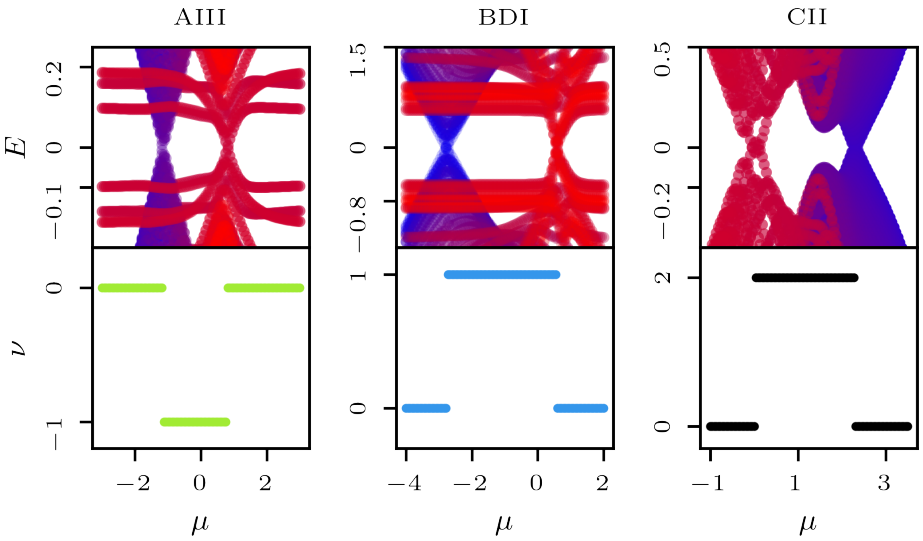

Figuur 2.9: The bulk invariant ν as a function of the chemical potential μ calculated using the effective Hamiltonian for chiral models AIII, BDI, and CII. Top panels: the bulk spectra of the effective Hamiltonians. States at $k = 0$ are in red, states at $k = \infty$ are in blue, and states at intermediate k are in varying shades of purple. Bottom panels: winding number invariants (2.52) obtained by dividing the integration space into 20 (AIII, CII) or 50 (BDI) segments.

the off-diagonal form of (2.48) with $q(\mathbf{k}) = -q(-\mathbf{k})^T$ [5]. This form of the symmetries is invariant under basis transformations of the block-diagonal form $\mathrm{diag}(u, u^*)$ which allows to bring spin operator to the diagonal form $S_z = \mathrm{diag}(s_z, -s_z)$. For half-integer S_z the combination $C_2\mathcal{T}$ leaves $\mathbf{k}$ invariant and acts as $\sigma_z q(\mathbf{k})\sigma_z = q(\mathbf{k})^T$. We find for the mirror operator that it takes a block-diagonal form $M = \mathrm{diag}(m, \pm m^*)$ where the $\pm$ stands for the commuting ($[U_M, \mathscr{P}] = [U_M, \mathcal{T}] = 0$) and anticommuting ($\{U_M, \mathscr{P}\} = \{U_M, \mathcal{T}\} = 0$) case. As m anticommutes with s_z it is only nonzero in the off-diagonal blocks connecting opposite spin eigenvalues. In a single $|s_z| \neq 0$ sector $s_z \propto \sigma_z$, and m has off-diagonal blocks μ and $\mu^\dagger$, these can be diagonalized by a basis transformation that in this sector acts as $\mathrm{diag}(\mathbb{1}, \mu)$. For class DIII$_+$ (DIII$_-$) we bring the reflection operator to the form $m = \sigma_x$ ($m = \sigma_y$) which imposes the constraint $\sigma_x q(\mathbf{k})\sigma_x = q(\mathbf{k})$ ($\sigma_y q(\mathbf{k})\sigma_y = q(\mathbf{k})$). We transform to a basis where $m = \sigma_z$ using $u = \exp(i\pi/2\sigma_y)$ ($u = \exp(i\pi/2\sigma_x)$), in this basis $q_\pm$ are the diagonal (off-diagonal) blocks of q and the $C_2\mathcal{T}$ constraint reads $q_+(\mathbf{k}) = q_-(\mathbf{k})^T$ ($q_\pm(\mathbf{k}) = q_\pm(\mathbf{k})^T$). In DIII$_+$ this implies $\det q_+(\mathbf{k}) = \det q_-(\mathbf{k})^T$, meaning that the winding is the same in both sectors, however, the total winding always vanishes in class DIII, so the reflection-resolved windings also vanish.

We write the 1D class DIII $\mathbb{Z}_2$ strong invariant [5] adapted to the compactified k-space as

$$\nu = \frac{\mathrm{Pf}\, q(\infty)}{\mathrm{Pf}\, q(\mathbf{0})} \exp\left(-\frac{i}{2}\int_0^\infty dk \frac{d}{dk} \arg\det q(k\hat{\mathbf{n}})\right). \tag{2.53}$$

This is also the strong 2D invariant, as the k-space sphere only has two time-reversal

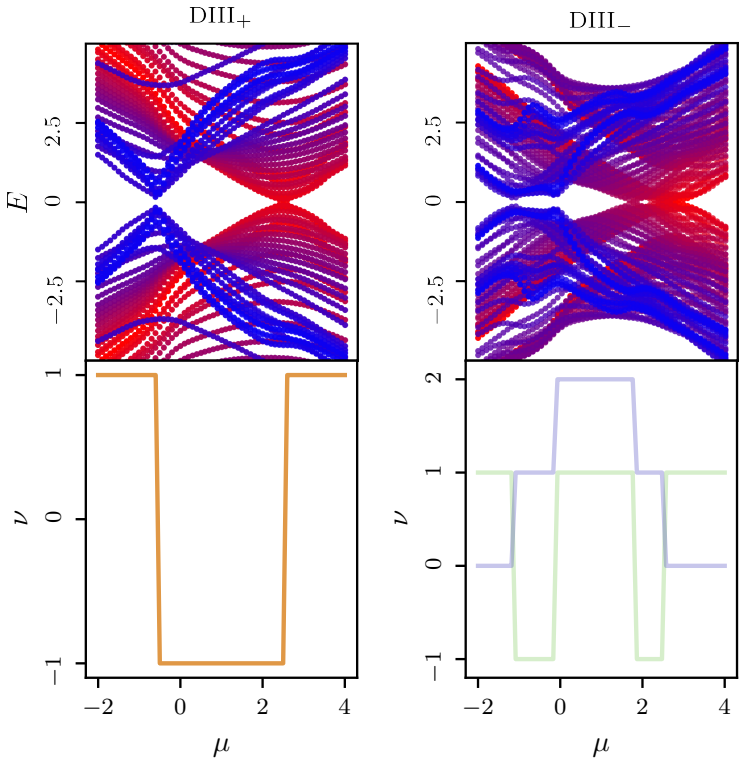

Figuur 2.10: The bulk invariant ν as a function of the chemical potential μ calculated using the effective Hamiltonian for the DIII model in the commuting (DIII$_+$) and anticommuting (DIII$_-$) cases. Top panels: the bulk spectra of the effective Hamiltonians. States at $k = 0$ are in red, states at $k = \infty$ are in blue, and states at intermediate k are in varying shades of purple. Bottom panels: the DIII $\mathbb{Z}_2$ mirror-resolved strong invariant (2.55) shown for the DIII$_+$ case (in orange). For the DIII$_-$ case, the DIII $\mathbb{Z}_2$ strong invariant (2.53) is shown in green, and the winding number invariant is shown in purple.

invariant momenta at $\mathbf{k} = \mathbf{0}$ and $\boldsymbol{\infty}$. In class DIII$_-$ q has off-diagonal blocks $q_\pm$ and $q_+(\mathbf{k}) = -q_-(\mathbf{k})^T$ for $\mathbf{k} = \mathbf{0}$ and $\boldsymbol{\infty}$, meaning $\mathrm{pf}\, q(\mathbf{k}) = (-1)^{n(n-1)/2} \det q_+(\mathbf{k})$ where n is the size of a reflection block. Using that $q_\pm(\mathbf{k}) = -q_\mp(-\mathbf{k})^T$ for all $\mathbf{k}$, adding and subtracting the winding $i\pi n_+$ in the exponential, and noting that the winding of the phase of the determinant between two points can only differ from the difference in the phases at the endpoints by a multiple of 2π, we find

$$\nu = e^{i\pi n_M}, \tag{2.54}$$

showing that the parity of n_M, hence the protection of gapless edges in the presence of disorder, is given by the strong invariant.

We define an invariant for class DIII$_+$ in terms of the reflection-resolved class DIII $\mathbb{Z}_2$ invariant:

$$\nu_\pm = \frac{\mathrm{pf}\; q_\pm(\boldsymbol{\infty})}{\mathrm{pf}\; q_\pm(\mathbf{0})} \exp\left(-\frac{i}{2}\int_0^\infty dk \frac{d}{dk} \arg\det q_\pm(k\hat{\mathbf{n}})\right). \tag{2.55}$$

As follows from the relations derived above, the invariant is the same for both sectors and we define the mirror invariant as $\nu_M = \nu_\pm$. This also shows that in class DIII$_+$ the strong invariant is always trivial in the presence of reflection symmetry.

BIBLIOGRAFIE

[1] M. Z. Hasan and C. L. Kane, *Colloquium: Topological insulators,* Rev. Mod. Phys. **82**, 3045 (2010).

[2] X.-L. Qi and S.-C. Zhang, *Topological insulators and superconductors,* Rev. Mod. Phys. **83**, 1057 (2011).

[3] S. Ryu, A. P. Schnyder, A. Furusaki, and A. W. W. Ludwig, *Topological insulators and superconductors: tenfold way and dimensional hierarchy,* New Journal of Physics **12**, 065010 (2010).

[4] A. Kitaev, V. Lebedev, and M. Feigelman, *Periodic table for topological insulators and superconductors,* in *AIP Conference Proceedings* (AIP, 2009).

[5] C.-K. Chiu, J. C. Y. Teo, A. P. Schnyder, and S. Ryu, *Classification of topological quantum matter with symmetries,* Rev. Mod. Phys. **88**, 035005 (2016).

[6] B. Bradlyn, L. Elcoro, J. Cano, M. G. Vergniory, Z. Wang, C. Felser, M. I. Aroyo, and B. A. Bernevig, *Topological quantum chemistry,* Nature **547**, 298 (2017).

[7] J. Kruthoff, J. de Boer, J. van Wezel, C. L. Kane, and R.-J. Slager, *Topological classification of crystalline insulators through band structure combinatorics,* Phys. Rev. X **7**, 041069 (2017).

[8] H. C. Po, A. Vishwanath, and H. Watanabe, *Symmetry-based indicators of band topology in the 230 space groups,* Nature Communications **8** (2017), 10.1038/s41467-017-00133-2.

[9] L. Fu, *Topological crystalline insulators,* Phys. Rev. Lett. **106**, 106802 (2011).

[10] L. Fu and C. L. Kane, *Topology, delocalization via average symmetry and the symplectic anderson transition,* Phys. Rev. Lett. **109**, 246605 (2012).

[11] I. C. Fulga, B. van Heck, J. M. Edge, and A. R. Akhmerov, *Statistical topological insulators,* Phys. Rev. B **89**, 155424 (2014).

[12] A. Agarwala and V. B. Shenoy, *Topological Insulators in Amorphous Systems,* Phys. Rev. Lett. **118**, 236402 (2017).

[13] Y.-B. Yang, T. Qin, D.-L. Deng, L.-M. Duan, and Y. Xu, *Topological amorphous metals,* Phys. Rev. Lett. **123**, 076401 (2019).

[14] K. Pöyhönen, I. Sahlberg, A. Weststrom, and T. Ojanen, *Amorphous topological superconductivity in a Shiba glass,* Nature Communications **9**, 2103 (2018).

[15] I. Sahlberg, A. Weststrom, K. Pöyhönen, and T. Ojanen, *Topological phase transitions in glassy quantum matter,* Phys. Rev. Research **2**, 013053 (2020).

[16] A. G. Grushin, *Topological phases of amorphous matter,* (2020), arXiv:2010.02851 .

[17] Q. Marsal, D. Varjas, and A. G. Grushin, *Topological weaire–thorpe models of amorphous matter,* Proceedings of the National Academy of Sciences **117**, 30260 (2020).

[18] J.-H. Wang, Y.-B. Yang, N. Dai, and Y. Xu, *Structural disorder induced second-order topological insulators in three dimensions,* arXiv , arXiv (2020).

[19] M. Dc, J.-Y. Chen, T. Peterson, P. Sahu, B. Ma, N. Mousavi, R. Harjani, and J.-P. Wang, *Observation of high spin-to-charge conversion by sputtered bismuth selenide thin films at room temperature,* Nano letters **19**, 4836 (2019).

[20] P. Sahu, Y. Fan, T. Peterson, J.-Y. Chen, X. Devaux, H. Jaffres, S. Migot, H. Dang, J.-M. George, Y. Lu, and J.-P. Wang, *Room temperature mott hopping and spin pumping characterization of amorphous gd-alloyed bi2se3,* (2021), arXiv:1911.03323 .

[21] P. Corbae, S. Ciocys, D. Varjas, S. Zeltmann, C. H. Stansbury, M. Molina-Ruiz, Z. Chen, L.-W. Wang, A. M. Minor, A. G. Grushin, A. Lanzara, and F. Hellman, *Evidence for topological surface states in amorphous Bi_2Se_3,* arXiv.org (2019), 1910.13412v1 .

[22] E. Prodan and W. Kohn, *Nearsightedness of electronic matter,* Proceedings of the National Academy of Sciences **102**, 11635 (2005).

[23] D. Varjas, A. Lau, K. Pöyhönen, A. R. Akhmerov, D. I. Pikulin, and I. C. Fulga, *Topological phases without crystalline counterparts,* Phys. Rev. Lett. **123**, 196401 (2019).

[24] D. Varjas, T. Ö. Rosdahl, and A. R. Akhmerov, *Qsymm: Algorithmic symmetry finding and symmetric Hamiltonian generation,* New J. Phys. **20**, 093026 (2018).

[25] M. Istas, C. Groth, A. R. Akhmerov, M. Wimmer, and X. Waintal, *A general algorithm for computing bound states in infinite tight-binding systems,* SciPost Phys. **4**, 26 (2018).

[26] C. W. J. Beenakker, *Random-matrix theory of quantum transport,* Rev. Mod. Phys. **69**, 731 (1997).

[27] K. Muttalib, P. Wölfle, and V. Gopar, *Conductance distribution in quasi-one-dimensional disordered quantum wires,* Annals of Physics **308**, 156 (2003).

[28] M. Diez, I. C. Fulga, D. I. Pikulin, J. Tworzydło, and C. W. J. Beenakker, *Bimodal conductance distribution of kitaev edge modes in topological superconductors,* New Journal of Physics **16**, 063049 (2014).

[29] T. Van Mechelen and Z. Jacob, *Quantum gyroelectric effect: Photon spin-1 quantization in continuum topological bosonic phases,* Phys. Rev. A **98**, 023842 (2018).

[30] T. Van Mechelen and Z. Jacob, *Nonlocal topological electromagnetic phases of matter,* Physical Review B **99** (2019), 10.1103/physrevb.99.205146.

[31] C.-K. Chiu, H. Yao, and S. Ryu, *Classification of topological insulators and superconductors in the presence of reflection symmetry,* Phys. Rev. B **88**, 075142 (2013).

[32] T. Morimoto and A. Furusaki, *Topological classification with additional symmetries from clifford algebras,* Phys. Rev. B **88**, 125129 (2013).

[33] K. Shiozaki and M. Sato, *Topology of crystalline insulators and superconductors,* Phys. Rev. B **90**, 165114 (2014).

[34] C.-B. Hua, R. Chen, B. Zhou, and D.-H. Xu, *Higher-order topological insulator in a dodecagonal quasicrystal,* Phys. Rev. B **102**, 241102(R) (2020).

[35] S. Spurrier and N. R. Cooper, *Kane-mele with a twist: Quasicrystalline higher-order topological insulators with fractional mass kinks,* Phys. Rev. Research **2**, 033071 (2020).

[36] G. Bergmann, *Amorphous metals and their superconductivity,* Physics Reports **27**, 159 (1976).

[37] C. Kane and T. Lubensky, *Topological boundary modes in isostatic lattices,* Nature Phys **10**, 39 (2014).

[38] R. Süsstrunk and S. D. Huber, *Observation of phononic helical edge states in a mechanical topological insulator,* Science **349**, 47 (2015).

[39] L. M. Nash, D. Kleckner, A. Read, V. Vitelli, A. M. Turner, and W. T. M. Irvine, *Topological mechanics of gyroscopic metamaterials,* Proc. Natl. Acad. Sci. **112**, 14495 (2015).

[40] I. Bloch, J. Dalibard, and S. Nascimbène, *Quantum simulations with ultracold quantum gases,* Nat. Phys. **8**, 267 (2012).

[41] L. Lu, J. D. Joannopoulos, and M. Soljačić, *Topological photonics,* Nat. Photonics **8**, 821 (2014).

[42] T. Ozawa, H. M. Price, A. Amo, N. Goldman, M. Hafezi, L. Lu, M. C. Rechtsman, D. Schuster, J. Simon, O. Zilberberg, and I. Carusotto, *Topological photonics,* Rev. Mod. Phys. **91**, 015006 (2019).

[43] C. H. Lee, S. Imhof, C. Berger, F. Bayer, J. Brehm, L. W. Molenkamp, T. Kiessling, and R. Thomale, *Topolectrical circuits,* Commun. Phys. **1** (2018), 10.1038/s42005-018-0035-2.

[44] H. Spring, A. R. Akhmerov, and D. Varjas, *Amorphous topological phases protected by continuous rotation symmetry,* Zenodo (2020), 10.5281/ZENODO.4382484.

[45] C. W. Groth, M. Wimmer, A. R. Akhmerov, and X. Waintal, *Kwant: a software package for quantum transport,* New Journal of Physics **16**, 063065 (2014).

[46] M. Wimmer, *Algorithm 923: Efficient numerical computation of the pfaffian for dense and banded skew-symmetric matrices,* ACM Trans. Math. Softw. **38**, 30:1 (2012).

[47] A. Weiße, G. Wellein, A. Alvermann, and H. Fehske, *The kernel polynomial method,* Rev. Mod. Phys. **78**, 275 (2006).

[48] D. Varjas, M. Fruchart, A. R. Akhmerov, and P. M. Perez-Piskunow, *Computation of topological phase diagram of disordered* $Pb_{1-x}Sn_xTe$ *using the kernel polynomial method,* Phys. Rev. Research **2**, 013229 (2020).

[49] P. W. Brouwer, C. Mudry, B. D. Simons, and A. Altland, *Delocalization in coupled one-dimensional chains,* Phys. Rev. Lett. **81**, 862 (1998).

[50] F. Zhang, C. L. Kane, and E. J. Mele, *Topological mirror superconductivity,* Phys. Rev. Lett. **111**, 056403 (2013).

3

ISOTROPIC 3D TOPOLOGICAL PHASES WITH BROKEN TIME REVERSAL SYMMETRY

The more chaotic I am, the more complete I am.

Austin Osman Spare

The data shown in the figures, as well as the code generating all of the data is available at [1].

3.1. INTRODUCTION

A three-dimensional (3D) isotropic medium has the highest degree of spatial symmetry. Unless they are explicitly broken, non-spatial symmetries like time-reversal symmetry (TRS) are also present in isotropic systems. Removing TRS typically also breaks isotropy, for example ferromagnets break TRS but also break rotation symmetry along the axes which are not parallel to the magnetization. Antiferromagnets restore some spatial symmetries such as the product of inversion and TRS, but also break rotation symmetry [2]. The spatial symmetries are partially restored in altermagnets [3]—a recently proposed class of materials combining lack of net magnetization with a spin splitting away from away from high-symmetry momenta, however even in these materials the magnetic order is incompatible with full isotropy.

The spatial symmetries of a system are relevant both for defining and protecting topological phases [4–7]. While initially considered to be susceptible to disorder, topological systems relying on spatial symmetries were later shown to be protected from localization as long as the disordered ensemble respects the spatial symmetries [8**?** , 9]. This protection by an 'average' symmetry, a hallmark of statistical topological insulators, is especially powerful in isotropic amorphous media. In an earlier work we demonstrated that unlike their crystalline counterparts—where the spatial symmetry is only preserved by certain crystal terminations—it is possible to utilize the isotropy of a 2D amorphous medium to extend the topological protection to any edge of the system [10].

Motivated by the two above considerations, we ask whether it is possible to find a model hosting a topological phase protected only by spatial symmetries. Because both TRS and average TRS protect topological phases, we additionally require that the desired model also breaks TRS on average. By designing a scalar, rather than a vector TRS breaking order, we answer positively to the above question. Specifically we demonstrate that the spatial symmetries present in 3D isotropic media protect topological phases, and that the amorphous realization of such a system is a statistical topological insulator phase.

The organization of the manuscript is as follows. In Sec. 3.2 we formulate an isotropic continuum model where TRS is systematically broken. We present a microscopic Hamiltonian that replicates this model when assembled into a crystal structure, and we present results for the amorphous realization of this model. In Sec. 3.3 we demonstrate the topological nature of our models by formulating bulk invariants, examining surface dispersions, and analyzing transport of the topologically protected surface modes. As established in the study of statistical topological insulator phases, we show that the model localizes when its degrees of freedom are doubled. We conclude in Sec. 5.5.

3.2. SYMMETRY ANALYSIS

3.2.1. CONTINUUM MODEL

In order to guide the construction of a microscopic model, we begin from developing a minimal continuum model with the desired symmetries using the software package Qsymm [11]. We follow the procedure outlined in Ref. [10]. We start by generating a minimal 2D Dirac Hamiltonian. The mass terms present in this minimal Hamiltonian are capable of gapping out the spectrum. We then search for all of the symmetry representations of inversion and continuous rotation symmetry that remove the mass terms

of the minimal Hamiltonian, thereby ensuring that the spatial symmetries prevent a gap from opening. These 2D Hamiltonians correspond to the surfaces of 3D topological bulk models in the same symmetry class. By utilizing the isotropy, we extend the symmetry representations from 2D to 3D to obtain the 3D bulk phases. The symmetry representations of the spatial symmetries are listed in App. 3.A, Eq. (3.A.1) and (3.A.2). The resulting k-space model is of the form:

$$\begin{aligned} H_{4\times4}(\boldsymbol{k}) = (\mu_1 + t_2 k^2)\sigma_0(\tau_0+\tau_z)/2 + (\mu_2 + t_3 k^2)\sigma_0(\tau_0-\tau_z)/2 \\ + (-t_1 + t_4 k^2)\boldsymbol{\sigma}\cdot\boldsymbol{k}\tau_y + (-t_0 + t_5 k^2)\boldsymbol{\sigma}\cdot\boldsymbol{k}\tau_x, \end{aligned} \tag{3.1}$$

where μ_i are chemical potential terms, t_i are the hopping terms, σ and τ are the Pauli matrices, with τ representing the orbital space and σ representing spin space, $\boldsymbol{k} = (k_x, k_y, k_z)$, and $k^2 = \boldsymbol{k}\cdot\boldsymbol{k}$.

Limiting the model to terms quadratic in k means a k-dependent transformation of the form $\exp(i\sigma_z\phi)$ is capable of removing the relative hopping phases and restoring a TRS-like symmetry. Therefore, the model includes terms up to k^3 in order to remove this residual symmetry.

Despite lacking TRS, the high degree of spatial symmetry of this model protects the twofold spin degeneracy of all bands. For a fixed $\boldsymbol{k}$, the eigenstates of (3.1) are eigenstates of the angular momentum operator in the direction parallel to $\boldsymbol{k}$. Mirror symmetry exchanges states with opposite angular momentum, thereby ensuring the degeneracy of the spin bands.

3.2.2. MICROSCOPIC IMPLEMENTATION

Based on the symmetry-allowed terms of the continuum model (3.1), we now construct a microscopic model that preserves isotropy while breaking TRS. The minimal model contains two orbitals that have opposite inversion eigenvalues, which we choose as an s and a p orbital. We choose the $\boldsymbol{\sigma}$ degree of freedom to correspond to the electron spin, which makes the last four terms of Eq. (3.1) spin-orbit-like, although with an additional k-dependent phase shift necessary to break TRS. In order to realize these spin-orbit-like hoppings in a microscopic model, we therefore consider two separate atoms that host spinful s and $p_{x,y,z}$ orbitals respectively, as illustrated in Fig. 3.1(a). For the purpose of obtaining a minimal model, we separate the p orbitals into $p_{3/2}$ and $p_{1/2}$ orbitals with an atomic spin-orbit coupling, and consider only the lower-energy $p_{1/2,\uparrow\downarrow}$ subspace.

In order to break TRS, we introduce magnetic atoms between the s and p orbitals. Hopping between the two atoms occurs through a virtual process via four s orbitals on a plane perpendicular to the s–p bond axis, located on the middle of the bond [Fig. 3.1(a)]. These intermediate s orbitals each host a magnetic moment, such that together they form a chiral magnetic texture in the plane that contains them. The curl of the magnetic texture defines a TRS-odd vector, that combined with the hopping vector $\boldsymbol{r}$, defines a scalar quantity $(\boldsymbol{\nabla}\times\boldsymbol{M})\cdot\boldsymbol{r}$. This is the desired source of scalar TRS breaking. Tiling the space with such s–p bonds restores spatial symmetries, while keeping TRS broken.

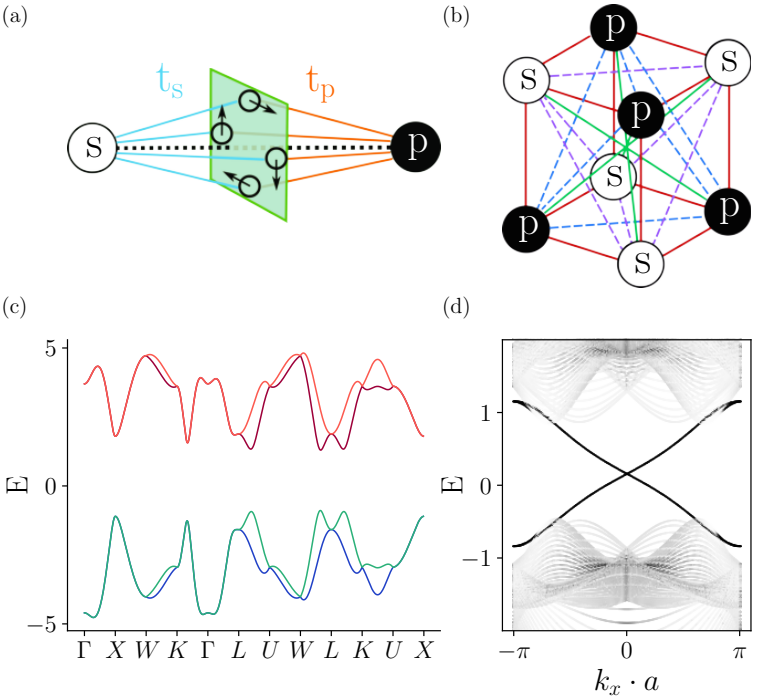

Figuur 3.1: Time-reversal symmetry breaking in a microscopic system with inversion and rotation symmetry. (a) A bond between s and p orbitals hosting four mid-bond s orbitals (on plane shown in green) that host magnetic moments. (b) A section of a rock salt crystal structure made from the bond shown in (a). Red lines indicate nearest-neighbor hopping between s and p orbitals, dashed lines indicate next-nearest neighbor hopping between s (purple) and p (blue) orbitals, green lines indicate next-next-nearest neighbor hopping between s and p orbitals. (c) The bulk dispersion relation obtained from the crystal structure shown in (b) along the high-symmetry points of the face-centered cubic Brillouin zone. Different colors indicate different bands. (d) Bulk and surface dispersion of a 3D slab of the crystal. Darker color indicates a larger participation ratio. Plot details are in App. 3.B.

The Hamiltonian of an x-aligned s–p bond is:

$$\begin{aligned} H_m = E_s \sum_\sigma |s_\sigma\rangle\langle s_\sigma| + E_p \sum_{i,\sigma} |p_{i\sigma}\rangle\langle p_{i\sigma}| + \sum_{n,\sigma} (\Delta |s_{n\sigma}\rangle\langle s_{n\sigma}| + t_s |s_\sigma\rangle\langle s_{n\sigma}| + \text{h.c.}) \\ + \sum_{i,n,\sigma} \left(t_{in} |p_{i\sigma}\rangle\langle s_{n\sigma}| + \text{h.c.}\right) + \alpha \hat{\boldsymbol{L}}_p \cdot \hat{\boldsymbol{\sigma}}_p + \sum_n \boldsymbol{B}_n \cdot \hat{\boldsymbol{\sigma}}_n, \end{aligned} \tag{3.2}$$

where $\sigma \in \{\uparrow, \downarrow\}$, $i \in \{x, y, z\}$, $n \in \{1, 2, 3, 4\}$, $|s_\sigma\rangle$ are the spinful s orbital states, $|s_{n\sigma}\rangle$ are the mid-bond magnetic s_n orbitals, $|p_{i\sigma}\rangle$ are the $p_{x,y,z}$ orbitals, $E_{s/p}$ are the onsite energies of the s and p orbitals, Δ is the onsite energy of the mid-bond s_n orbitals, α is the magnitude of the atomic spin-orbit coupling splitting on the p orbitals, $\hat{\boldsymbol{\sigma}}_{p/n}$ are the spin operators on the p and s_n orbitals, $\hat{\boldsymbol{L}}_p$ are the orbital angular momentum operators on the p-orbitals, $\boldsymbol{B}_n$ are the magnetic moments of the s_n orbitals. Finally, t_{in} are the amplitudes of the s_n– p_i hopping, determined by whether the hopping between the $p_{x,y,z}$ orbitals and the

s_n orbitals takes place via the positive or negative lobes of the p orbitals:

$$t_{in} = t_x \delta_{ix} + t_{yz} \delta_{iy} \mathrm{sgn}(y_n) + t_{yz} \delta_{iz} \mathrm{sgn}(z_n) \tag{3.3}$$

where y_n and z_n are the y and z coordinates of the s_n orbitals and $\mathrm{sgn}(0) = 0$.

We use the Python software package Pymablock [12] to obtain the effective hopping t_{sp} between the s and $p_{1/2}$ orbitals as a second-order perturbation. We find that the resulting terms have the desired symmetries by substituting in arbitrary parameters. We demonstrate this result in a limiting case defined by the set of inequalities $\alpha \gg \Delta + B \gg \Delta - B \gg E_s,\ E_p - \alpha,\ t_s,\ t_{x/y/z}$, which holds when spin-orbit coupling is large, and hopping only occurs via the lower-energy virtual level $\Delta - B$. The resulting expression for the effective hopping amplitude is:

$$t_{sp} = \frac{t_s(2t_x - i\,t_{yz})}{\sqrt{3}(\Delta - B)}\, i\sigma_x. \tag{3.4}$$

This hopping has a complex hopping phase, which breaks TRS. In order to ensure that the hopping phase cannot be removed by a global basis-transformation introducing a relative phase between the s and p wavefunctions, the hopping phase must be distance dependent. This arises naturally due to the different distance dependence of the microscopic hopping amplitudes from the p_x and $p_{y,z}$ orbitals. Hopping terms along directions other than x follow from applying rotation operators, resulting in hopping terms proportional to $\boldsymbol{d} \cdot \boldsymbol{\sigma}$ where $\boldsymbol{d}$ is the hopping vector.

3.2.3. SPIN SPLITTING IN A CRYSTAL

Because the scalar TRS breaking is insufficient to cause a spin splitting in an isotropic medium, we demonstrate the spin splitting in a crystal structure. We use the s and p atoms as the basis of the rock salt crystal structure [Fig. 3.1(b)] with full cubic (O_h) symmetry. In this model, orbitals of the same type are connected by normal hopping, and orbitals of different types are connected by the complex spin-orbit hopping of (3.4), resulting in terms off-diagonal in the orbital (τ) space. Because the symmetry-breaking mechanism relies on the nontrivial distance-dependence of the hopping phase, we include both nearest-neighbor as well as third-nearest-neighbor s–p hopping [Fig. 3.1(b)]. The tight-binding Hamiltonian thus takes the form:

$$\begin{aligned} H_{\mathrm{salt}} = &\left(\mu_1 + t_1 \sum_{\boldsymbol{d}_2} e^{i\boldsymbol{k}\cdot\boldsymbol{d}_2}\right)\sigma_0(\tau_0 + \tau_z)/2 + \left(\mu_2 + t_2 \sum_{\boldsymbol{d}_2} e^{i\boldsymbol{k}\cdot\boldsymbol{d}_2}\right)\sigma_0(\tau_0 - \tau_z)/2 \\ &+ \frac{i}{a}\left(\sum_{\boldsymbol{d}_1} e^{i\boldsymbol{k}\cdot\boldsymbol{d}_1}\boldsymbol{d}_1 \cdot \boldsymbol{\sigma}\right)\left(t_3\tau_+ + t_3^*\tau_-\right) + \frac{i}{a}\left(\sum_{\boldsymbol{d}_3} e^{i\boldsymbol{k}\cdot\boldsymbol{d}_3}\boldsymbol{d}_3 \cdot \boldsymbol{\sigma}\right)\left(t_4\tau_+ + t_4^*\tau_-\right), \end{aligned} \tag{3.5}$$

where a is the cubic cell lattice constant, $\sigma_\pm = \frac{1}{2}(\sigma_x \pm i\sigma_y)$, and similarly for $\tau_\pm$. $\boldsymbol{d}_1$ runs over the six nearest-neighbor bonds symmetry-equivalent to $\frac{a}{2}(1,0,0)$, $\boldsymbol{d}_2$ over the twelve next-nearest neighbor bonds symmetry-equivalent to $\frac{a}{2}(1,1,0)$, and $\boldsymbol{d}_3$ over the eight next-next-nearest neighbor bonds symmetry-equivalent to $\frac{a}{2}(1,1,1)$. The terms of Eq. (3.5) proportional to t_1 and t_2 are the next-nearest neighbor $s-s$ and $p-p$ normal hoppings respectively [dashed lines of Fig. 3.1(b)], where t_1 and t_2 are both real. The

terms proportional to t_3 and t_4 are the nearest and next-next-nearest neighbor s–p hoppings respectively [solid lines of Fig. 3.1(b)], with t_3 and t_4 complex. This Bloch Hamiltonian reproduces the symmetry-allowed terms of the continuum model (3.1) in the long-wavelength limit, aside from an additional cubic anisotropy term and a slight change of parametrization.

The tight-binding model (3.5) preserves the space group of the rock salt crystal structure [see App. 3.A]. The spin-orbit-like s–p hopping terms alternate in sign along the hopping axes in order to preserve inversion symmetry. We select the parameters $\mu_1 = 0.1$, $\mu_2 = 0.2$, $t_1 = 0.3$, $t_2 = -0.4$, $t_3 = \exp(0.3i)$, $t_4 = 0.2i\exp(0.3i)$. The dispersion relation shows that the spin bands are split away from high-symmetry points and lines that have at least a rotation and a mirror symmetry, demonstrating that TRS is broken [Fig. 3.1(c)]. The TRS-breaking terms of our model are next-next-nearest neighbor terms, which leads to linear TRS-breaking terms intrinsically cancelling out and only cubic terms remaining. The surface dispersion shows gapless, propagating surface modes within the bulk gap [Fig. 3.1(d)].

3.2.4. AMORPHOUS REALIZATION

Amorphous systems possess average continuous rotation symmetry, average reflection and average inversion [10]. Since the scalar TRS-breaking mechanism is independent of bond orientation, an amorphous realization of the crystal model (3.5) possesses ensemble isotropy while also systematically breaking time-reversal.

We construct amorphous systems using the same procedure as in Ref. [10], treating system sites as hard spheres. Rather than simulating an amorphous version of the crystal defined in Sec. 3.2.3, with two families of atoms and two degrees of freedom per atom, for simplicity and without loss of generality we simulate one type of atom with four degrees of freedom. We define a minimal real-space model using Qsymm. To further examine the extent of topological protection, we also define a model with twice the degrees of freedom and two protected Dirac cones on the surface in the continuum limit (see App. 3.A for the full definition of both models). We examine the spectral functions of the minimal model, and confirm the joint presence of a spectral gap and the lack of spin splitting [Fig. 3.2(a)], as expected from the symmetry analysis of the continuum model. The surface spectral function confirms the presence of gapless surface modes within the bulk gap [Fig. 3.2(b)].

3.3. TOPOLOGICAL PROPERTIES

3.3.1. BULK INVARIANTS

To define the topological invariants, we observe that the high spatial symmetry guarantees that the protected band gap closings only occur at high symmetry momenta: $\boldsymbol{k} = \mathbf{0}$ and $\boldsymbol{k} = \boldsymbol{\infty}$ for the amorphous system. To compute the k-space topological invariant we use an effective k-space Hamiltonian H_{eff} that we obtain by inverting the single-particle Green's function that we project onto the plane wave basis, as described in Refs. [7, 10, 13].

The invariants of 3D statistical topological insulators are constructed from the invariants of 2D strong topological phases [9]. The invariant of 2D class A systems is the Chern number, given by the integral of the Berry curvature over the 2D Brillouin zone at the Fermi energy. Our 3D class A model relies on mirror symmetry to protect its surface

modes. Therefore a possible bulk invariant of this model is a mirror Chern number, given by the difference in Chern numbers of opposite mirror sectors:

$$C_M = \frac{1}{2}(C_+ - C_-), \quad C_\pm = \iint \mathscr{F}_\pm(\boldsymbol{k})\, d^2\boldsymbol{k}, \tag{3.6}$$

where the integral runs over a compactified mirror-invariant plane $\mathbb{R}^2 \cup \{\infty\}$ [10, 13] (e.g. $k_z = 0$, invariant under the mirror operator $k_z \to -k_z$ with $U_{M_z} = \mathscr{I}\exp(i\pi S_z)$), and $\mathscr{F}_\pm$ is the Berry curvature of the even/odd ($\pm i$ eigenvalue) mirror sub-blocks of the Hamiltonian. The invariant for crystal systems has the same form for a mirror-invariant plane in the crystal Brillouin zone[4]. However, because both the systems have inversion and rotation symmetries, the mirror Chern number can also be expressed in terms of rotation and inversion eigenvalues at high-symmetry momenta. Numerical results and a further discussion of invariants of the amorphous system are found in App. 3.C.

3.3.2. SURFACE SPECTRUM

As demonstrated in Fig. 3.1(d) for the crystalline system, the high-symmetry surface of the $C_M = 1$ model hosts a single Dirac cone, and multiple Dirac cones remain protected for $C_M > 1$. We expect that the high degree of ensemble averaged spatial symmetry of the amorphous Hamiltonian prevents surface states from being gapped out on any surface both for the single and doubled model ($C_M = 1$ and 2 respectively). We confirm this by numerically computing the surface spectral function

$$A(E, \boldsymbol{k}) = \sum_l \langle \boldsymbol{k}, l | \, \delta(H - E) \, | \boldsymbol{k}, l \rangle \,, \tag{3.7}$$

using the Kernel polynomial method[10, 14, 15]. Here H is the real-space Hamiltonian of a finite slab, l runs over the internal degrees of freedom, and $|\boldsymbol{k}, l\rangle$ is a plane-wave state localized on one surface.

Both the original and doubled amorphous models have a nonzero surface density of states in the bulk gap, with one or two Dirac nodes located at zero momentum. [Fig. 3.2(b,c)]. This is a consequence of the nontrivial topology of the effective Hamiltonian, or equivalently, of the disorder-avaraged Green's function. The surface spectral function in the k_x direction probes the topology of the $k_y = 0$ cut of the bulk effective Hamiltonian, which is invariant under M_y in the thermodynamic limit. This allows decomposition into two mirror sectors, each of which is a Chern insulator, resulting in an edge spectrum with C_M pairs of counter-propagating chiral edge states crossing the bulk gap. The modes with different chirality correspond to different mirror sectors, hence they are protected from gapping out by disorder that respects the mirror symmetry on average. The surface states are insensitive to the details of the boundary, and only gap out when the symmetries protecting the topological phase (rotations and mirrors normal to the surface) are broken on average [Fig. 3.2(d,e)].

3.3.3. SURFACE TRANSPORT

Reference [9] conjectures that only the $\mathbb{Z}_2$ part of the invariant provides topological protection, or in other words, that only the surface states of systems with odd C_M are protected from localization. In a crystalline system, the surface has an ensemble point

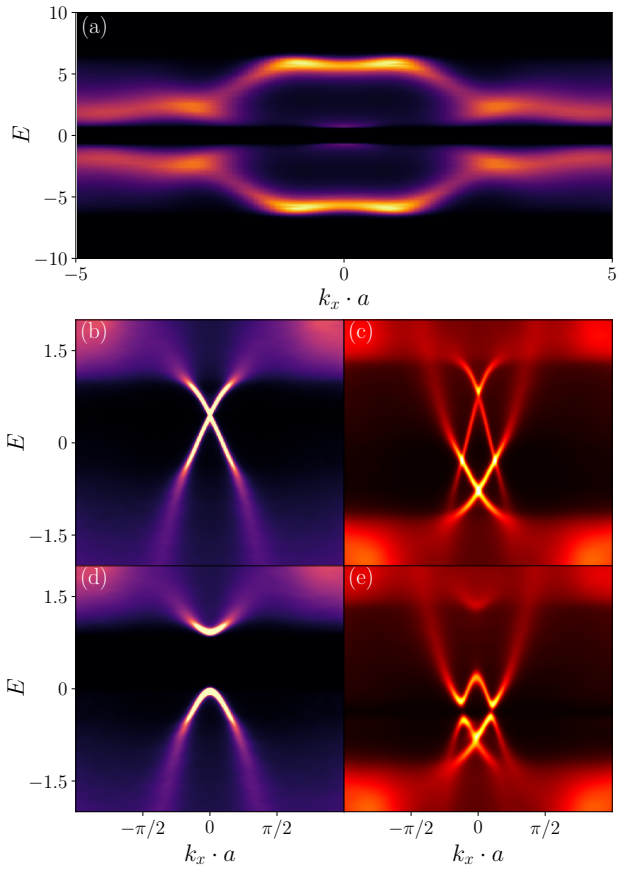

Figuur 3.2: The (a) bulk and (b)-(e) surface spectral functions of the amorphous models. (b)-(c) The surface spectral functions of the single Dirac cone model (3.A.4) and the double Dirac cone model (3.A.8). (d)-(e) the same models as (b)-(c) but with broken spatial (mirror and rotation) symmetries. Plot details are in App. 3.B.

group symmetry, and its localization properties are therefore equivalent to a doubled Chalker-Coddington network model, which has a localized phase with an anomalously large localization length [16, 17]. The conjecture, however, was not confirmed for 3D phases with continuous rotation symmetries, such as our amorphous model. To confirm the conjecture, we simulate the surface transport properties using amorphous network models.

We first simulate the transport properties of the regular network model as a baseline for the comparison. In the presence of disorder that preserves the spatial symmetries on average, the surface of the crystalline phase is equivalent to a critical Chern insulator. We simulate its transport properties with the Chalker-Coddington network model on the square lattice [18]. We fix the aspect ratio of the network to 1 and impose periodic boundary conditions along the y direction [Fig. 3.3(a)]. The scattering matrices at each node of the network are random 2×2 matrices sampled from a Haar-distributed $U(2)$

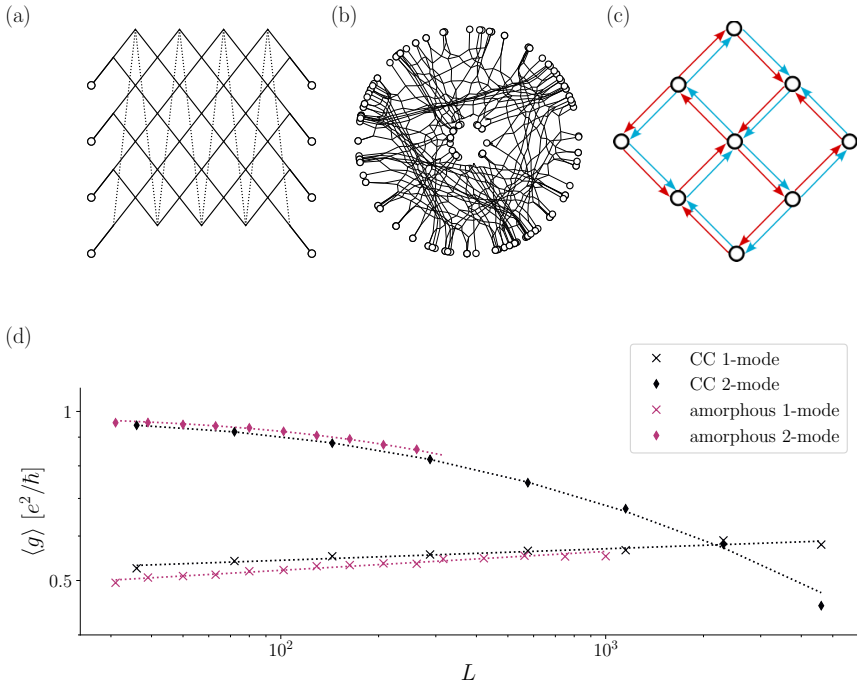

Figuur 3.3: Conductivity of translationally invariant and amorphous networks. (a) Schematic of the Chalker-Coddington model. Dashed links loop in the vertical direction to indicate periodic boundary conditions. Circular nodes indicate external nodes where modes enter and exit the network. Internal nodes are located at all solid line crossings. (b) Schematic of the amorphous network. Circular nodes indicate external nodes where modes enter and exit the network. Nodes internal to the network are located at all line crossings. (c) Schematic of modes in the doubled model. (d) Average conductivity of the networks as a function of network length and width L and fits (dashed lines). Results are shown for the Chalker-Coddington (CC) network and amorphous network, with 1 mode per link (crosses) and 2 modes per link (diamonds). Plot details are in App. 3.B.

ensemble. The conductance through the system is:

$$G = \frac{e^2}{h} \sum_i T_i, \tag{3.8}$$

where T_i are the transmission probabilities from the modes entering one side of the network to the modes exiting on the other side. Since the aspect ratio equals to 1, the system conductivity $g = G$. We calculate the average conductivity $\langle g \rangle$ as a function of system size L and reproduce the known result $\langle g \rangle \approx 0.5$–$0.6 e^2/\hbar$ [19] [Fig. 3.3(d)], with the slow increase as a function of L due to finite-size effects. We investigate the localization properties of the double Dirac cone model by doubling the number of modes on each link, as shown schematically in Fig. 3.3(c). This system is expected to localize, based on both numerical [16] and analytical [17] studies. We draw the 4×4 scattering matrices of the doubled networks from the circular unitary ensemble and confirm localization at system sizes of several thousand sites [Fig. 3.3(d)].

We now simulate the conductance of our amorphous model, in order to determine whether the average continuous rotation symmetry has an effect on the conductance properties of the system. We define an amorphous 2D network model in order to simulate the average rotation symmetry using a fourfold coordinated random graph [13, 20], for details of the construction of the amorphous network see App. 3.D. We use an annulus geometry in order to avoid issues constructing the network with periodic boundary conditions, and numerically calculate the conductance through the bulk from the modes entering the outer edge to the modes exiting the inner edge of the annulus [Fig. 3.3(b)]. The conductance G is calculated using (3.8), and the conductivity of the annulus equals:

$$g = \frac{1}{2\pi} G \log\left(\frac{R}{r}\right), \tag{3.9}$$

where R and r are the outer and inner radii of the annulus respectively. The results for the amorphous network closely follow the results for the regular network: the single Dirac cone conductivity falls within the $0.5 - 0.6 e^2/\hbar$ range for small L and increases due to finite-size effects, and the double Dirac cone network localizes [Fig. 3.3(d)]. These observations confirm that a doubled phase transition is not protected from localization, even in the presence of average isotropy.

3.4. CONCLUSION AND DISCUSSION

In this work, we found that 3D isotropic systems breaking all non-spatial symmetries host topologically protected phases of matter. We devised a rotation- and inversion-symmetric continuum model with broken time-reversal symmetry, and presented a microscopic realization of this model in amorphous matter with average isotropy. We constructed a bulk $\mathbb{Z}$ invariant—expressible both in terms of symmetry eigenvalues and mirror Chern numbers—corresponding to the number of protected ungappable surface Dirac cones, which we numerically demonstrated.

We simulated the transport of our models using both regular and amorphous network models with random scattering at each node. We found results consistent with critical scaling, deviations from which are likely due to finite-size effects. Upon doubling the degrees of freedom in both the regular and amorphous networks, the modes localize as conjectured in Refs. [9, 16, 17]. Even though any number of surface Dirac cones are protected from gapping out, only an odd number are protected from localization.

Due to the combination of average continuous rotation symmetry and inversion symmetry, the spin bands in the bulk of the amorphous system are doubly degenerate. This raises the question whether the systematic breaking of TRS leads to a macroscopic change in the material properties. Enumerating the possible non-dissipative electromagnetic responses compatible with isotropy and inversion-symmetry, but forbidden by TRS, we find $\boldsymbol{P} \propto \boldsymbol{E} \times \boldsymbol{B}$, electrical polarization parallel to the Poynting vector. This second-order response is distinct from the circular photogalvanic effect [21, 22], which only manifests in systems with broken inversion symmetry, and should therefore be absent in our system. The combination of these two responses therefore serve as a probe of the scalar TRS breaking.

A natural further quesion is, what is the classification of isotropic three-dimensional media with or without inversion symmetry in the other Altland-Zirnbauer symmetry

classes[23]. The topological invariants outlined in this work remain valid if we also include TRS besides isotropy and inversion symmetry. Our models are compatible with prescribing TRS with the usual representation $\mathscr{T} = \exp(i\pi S_y)\mathscr{K}$, which fixes some parameters, but does not forbid any topological phases. In this case odd values of C_M correspond to an amorphous strong topological insulator [24], however, the gapless surface Dirac cones remain protected by mirror symmetry for even values as well. To our knowledge, TRS does not enrich the classification in the presence of isotropy and inversion symmetry; and the classification with isotropy, broken inversion and unbroken TRS is the same as the strong $\mathbb{Z}_2$ classification with TRS only. There is, however an interesting possibility that isotropy and the protection of the surface density of states in a doubled phase prevents the surface conductivity from going below the metal-insulator critical point, and because of that guaranteeing that the surface stays metallic. We leave an investigation of these properties to future work.

Our microscopic model—relying on orbital-selective hoppings through chiral magnetic molecules—demonstrates the difficulty of constructing a time-reversal odd, inversion even, scalar order parameter. In our case the order parameter is $\boldsymbol{P}\cdot(\boldsymbol{\nabla}\times\boldsymbol{M})$, electric polarization times bound current. Analyzing an effective field-theory displaying such order paramater without other symmetry breaking would shed further light on the properties of this class of isotropic magnetic materials.

3.A. MODEL HAMILTONIANS

We use Qsymm to generate 3D class A models that respect inversion symmetry and isotropic continuous rotation symmetry, whose symmetry representations are:

$$U_{\mathscr{I}} = \sigma_0\tau_z,\ S_x = \frac{1}{2}\sigma_x\tau_0,\ S_y = \frac{1}{2}\sigma_y\tau_0,\ S_z = \frac{1}{2}\sigma_z\tau_0, \tag{3.A.1}$$

where $U_{\mathscr{I}}$ is the unitary part of the inversion operator, $S_{x,y,z}$ are the generators of continuous spin rotations around the x, y, and z axes, and the unitary part of the corresponding rotation operator is given by $U = \exp(i\boldsymbol{n}\cdot\boldsymbol{S})$ with $\boldsymbol{n}$ the axis and angle of rotation, and τ, σ are the Pauli matrices. τ represents the orbital component, and σ the spin component of the Hilbert space. The resulting model also has reflection symmetry on any 2D plane,

$$U_{\mathscr{M}_x} = i\sigma_x\tau_z,\ U_{\mathscr{M}_y} = i\sigma_y\tau_z,\ U_{\mathscr{M}_z} = i\sigma_z\tau_z, \tag{3.A.2}$$

where $U_{\mathscr{M}_{x,y,z}}$ is the unitary part of the reflection operators on the planes perpendicular to the x, y and z axes, or in general,

$$U_{\mathscr{M}_{\hat{\boldsymbol{n}}}} = \exp(i\pi\hat{\boldsymbol{n}}\cdot\boldsymbol{S})\tau_z, \tag{3.A.3}$$

where $\hat{\boldsymbol{n}}$ is a unit vector defining the mirror normal. Because of the full rotation invariance, prescribing one mirror symmetry results in mirror symmetry with respect to any plane.

The generated k-space model is listed in the main text in Eq. (3.1). In real-space, the model is of the form:

$$H_{4\times4}^{\text{onsite}} = \mu_1\sigma_0(\tau_0+\tau_z)/2 + \mu_2\sigma_0(\tau_0-\tau_z)/2, \tag{3.A.4}$$

$$\begin{aligned} H_{4\times4}^{\text{hopping}}(\boldsymbol{d}) = {} & (tn_1 + t_2d^2)\sigma_0(\tau_0+\tau_z)/2 + (tn_2 + t_3d^2)\sigma_0(\tau_0-\tau_z)/2 \\ & + (t_0 - t_5d^2)\boldsymbol{\sigma}\cdot\boldsymbol{d}\tau_y + (t_1 + t_4d^2)\boldsymbol{\sigma}\cdot\boldsymbol{d}\tau_x, \end{aligned} \tag{3.A.5}$$

where tn_i are normal hopping terms, $\boldsymbol{d} = (d_x, d_y, d_z)$, with d_i the bond lengths along axis $i \in \{x, y, z\}$ that connect neighboring sites, and $d^2 = \boldsymbol{d}\cdot\boldsymbol{d}$.

When demonstrating that symmetry-breaking gaps out the surface Dirac-nodes, we introduce a mass term that breaks all symmetries except for continuous rotation around the x axis:

$$\lambda = (\sigma_0 + \sigma_x)\tau_y. \tag{3.A.6}$$

We also construct a doubled model. In k-space, this model takes the form:

$$\begin{aligned} H_{8\times8}(\boldsymbol{k}) = {} & 1/2(\rho_0+\rho_z)\sigma_0(\mu_1(\tau_0+\tau_z)/2 + \mu_2(\tau_0-\tau_z)/2) \\ & + 1/2(\rho_0-\rho_z)\sigma_0(\mu_3(t\tau_0+\tau_z)/2 + \mu_4(\tau_0-\tau_z)/2) \\ & + (t_0(\rho_0+\rho_z)/2 + t_3(\rho_0-\rho_z)/2)\boldsymbol{\sigma}\cdot\boldsymbol{k}\tau_x \\ & - (t_4(\rho_0+\rho_z)/2 + t_7(\rho_0-\rho_z)/2)\boldsymbol{\sigma}\cdot\boldsymbol{k}\tau_y \\ & + (t_1 + it_5)\rho_-\boldsymbol{\sigma}\cdot\boldsymbol{k}\tau_- + (t_1 - it_5)\rho_+(\boldsymbol{\sigma}\cdot\boldsymbol{k}\tau_-)^\dagger \\ & + (t_2 + it_6)\rho_-\boldsymbol{\sigma}\cdot\boldsymbol{k}\tau_+ + (t_2 - it_6)\rho_+(\boldsymbol{\sigma}\cdot\boldsymbol{k}\tau_+)^\dagger, \end{aligned} \tag{3.A.7}$$

where μ_i are chemical potential terms, t_i are the hopping terms, ρ, σ and τ are the Pauli matrices, $\boldsymbol{k} = (k_x, k_y, k_z)$, and $k^2 = \boldsymbol{k}\cdot\boldsymbol{k}$. In real space, the model takes the form:

$$\begin{aligned} H_{8\times8}^{\text{onsite}} = {} & 1/2(\rho_0+\rho_z)\sigma_0(\mu_1(\tau_0+\tau_z)/2 + \mu_2(\tau_0-\tau_z)/2), \\ & + 1/2(\rho_0-\rho_z)\sigma_0(\mu_3(\tau_0+\tau_z)/2 + \mu_4(\tau_0-\tau_z)/2) \end{aligned} \tag{3.A.8}$$

$$\begin{aligned} H_{8\times8}^{\text{hopping}}(\boldsymbol{d}) = {} & 1/2(\rho_0+\rho_z)\sigma_0(tn_1(\tau_0+\tau_z)/2 + tn_2(\tau_0-\tau_z)/2) \\ & + 1/2(\rho_0-\rho_z)\sigma_0(tn_3(\tau_0+\tau_z)/2 + tn_4(\tau_0-\tau_z)/2) \\ & + (it_0(\rho_0+\rho_z)/2 + it_3(\rho_0-\rho_z)/2)\boldsymbol{\sigma}\cdot\boldsymbol{d}\tau_x \\ & - (it_4(\rho_0+\rho_z)/2 + it_7(\rho_0-\rho_z)/2)\boldsymbol{\sigma}\cdot\boldsymbol{d}\tau_y \\ & + (-t_5 + it_2)\rho_-\boldsymbol{\sigma}\cdot\boldsymbol{d}\tau_- + (t_5 + it_2)\rho_+(\boldsymbol{\sigma}\cdot\boldsymbol{d}\tau_-)^\dagger \\ & + (-t_6 + it_1)\rho_-\boldsymbol{\sigma}\cdot\boldsymbol{d}\tau_+ + (t_2 + it_6)\rho_+(\boldsymbol{\sigma}\cdot\boldsymbol{d}\tau_+)^\dagger, \end{aligned}$$

where tn_i are normal hopping terms, $\boldsymbol{d} = (d_x, d_y, d_z)$, with d_i the bond lengths along axis $i \in \{x, y, z\}$ that connect neighboring sites, and $d^2 = \boldsymbol{d}\cdot\boldsymbol{d}$. The symmetry-breaking term for the doubled model is

$$\lambda' = \begin{pmatrix} 1 & 1 \\ 1 & 1 \end{pmatrix} \otimes \begin{pmatrix} 1 & 1 \\ 1 & 1 \end{pmatrix} \otimes \tau_y. \tag{3.A.9}$$

3.B. MODEL AND PLOTTING PARAMETERS

In this section additional details of the plots are listed in order of appearance.

For panel (c) of Fig. 3.1 the Hamiltonian (3.5) was simulated using kwant [25] on a translationally invariant 3D face-centered cubic (FCC) lattice. Its eigenvalues were obtained along the high-symmetry points of the FCC lattice, using the parameters $\mu_1 = 0.1,\ \mu_2 = 0.2,\ t_1 = 0.3,\ t_2 = -0.4,\ t_3 = \exp(0.3i),\ t_4 = 0.2i\exp(0.3i)$. For the dispersion shown in panel (d), a slab was simulated, periodic along the vectors $[1,0,0]$ and $[0,1,0]$, and with a width of 20 sites in the $[0,0,1]$ direction. The parameters used are the same as for panel (c).

For panel (a) of Fig. 3.3, the Chalker-Coddington network is composed of four unit cells in both x and y. For panel (b), the amorphous network was created with an outer radius of $R = 20$, an inner radius of $r = 4$, and a density of 1. The positions of the nodes of the network underwent a relaxation step where the position of each node is sequentially averaged over the position of all neighboring nodes. For panel (d), the results for single-mode Chalker-Coddington network were obtained for 249 different random scattering matrix configurations, for network sizes of 36, 72, 144, 288, 576, 1152, 2304 and 4608 unit cells, with an aspect ratio of 1. The results for the two-mode Chalker-Coddington network were obtained for the same network sizes and aspect ratio, and for 269 different scattering matrix configurations. For the amorphous network, the results were obtained for 50 outer radii sizes between $10^{1.5}$ and $10^{2.5}$, with a fixed outer radius over inner radius ratio of 1.5, and a density of 0.7. Results for the single mode network were obtained for 500 different amorphous network and scattering matrix configurations, and 300 different configurations for the two-mode amorphous network. Additional results for the single mode network were obtained for 5 outer radii sizes between $10^{2.5}$ and 10^3, for 100 different network configurations and scattering matrices.

For Fig. 3.2(a), single-Dirac cone model as defined in Eq. (3.A.4) was used. Its parameters were set to $\mu_1 = -1,\ \mu_2 = 1,\ tn_1 = 0,\ tn_2 = 0,\ t_0 = 0.5,\ t_1 = 0.4,\ t_2 = 1,\ t_3 = -1,\ t_4 = 0.3,\ t_5 = 0.8$ and the additional symmetry-breaking term λ from Eq. (3.A.6) is set to 0. For panels (b) and (d) the same model as panel (a) was used. Its parameters were set to $\mu_1 = 1,\ \mu_2 = -1,\ tn_1 = -2,\ tn_2 = 2,\ t_0 = 1,\ t_1 = 1,\ t_2 = 1.1,\ t_3 = 1.2,\ t_4 = 1.3,\ t_5 = 1.25$ and the additional symmetry-breaking term λ from Eq. (3.A.6) is set to 0. The results were obtained obtained for k-points between $-\pi$ and π. For panel (d) and (e), λ is set to 0.3. For the doubled model as defined in Eq. (3.A.8), the parameters were set to $\mu_1 = 1,\ \mu_2 = -1,\ \mu_3 = 1,\ \mu_4 = -1,\ tn_1 = -2,\ tn_2 = 2,\ tn_3 = -2,\ tn_4 = 2,\ \lambda_1 = 0.1,\ \lambda = 0.11,\ \lambda_3 = 0.12,\ \lambda_4 = 0.123$. The amorphous slab was generated in a box of dimensions $200 \times 50 \times 50$ and density 0.4.

For panel (a) of Fig. 3.C.1, the model (3.A.4) was used. For all results, the hopping parameters were set to $t_0 = 1,\ t_1 = 1.2,\ t_2 = 0,\ t_3 = 0,\ t_4 = 0,\ t_5 = 0,\ tn_1 = -2,\ tn_2 = 2$ (terms proportional to k to the power of 2 and higher are set to 0). Since the only hopping terms are linear in d, in order to ensure that TRS is broken for this model, a different distance dependence is given for the t_1 and t_2: $t_1\exp(-0.3d)$ and $t_2\exp(-d)$, where $d = \sqrt{d^2}$ is the bond length. The amorphous samples are all contained within a cube of 30 x 30 x 30 sites, with a density of 0.7, and the crystal samples are all 10 x 10 x 10 sites. For the invariant ν_M (3.6) the numerical integration over the Brillouin zone of the effective Hamiltonian was done over a grid of 15 x 15 points.

For panel (b) of Fig. 3.C.1, the model (3.5) was used. The parameters were set to $t_1 = 0.3,\ t_2 = -0.4,\ t_3 = \exp(0.3i),\ t_4 = i\exp(0.3i)$. The Γ and X points of the model are

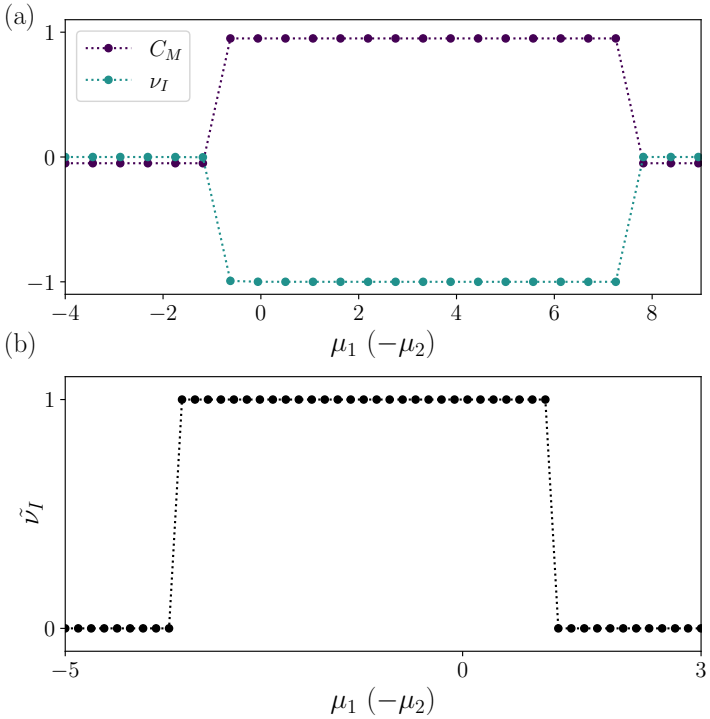

Figuur 3.C.1: Conductivity of translationally invariant and amorphous networks. (a) The topological invariants of the class A model (3.A.4) for amorphous systems (C_M defined in (3.6) and ν_I in (3.C.1)) as a function of chemical potentials $\mu_{1,2}$. Plots are offset for clarity. (b) The invariant $\tilde{\nu}_I$ of the crystal system as a function of chemical potentials $\mu_{1,2}$ (3.5). Plot details are in App. 3.B.

$(0,0,0)$ and $(0,2\pi,0)$.

3.C. ALTERNATIVE BULK INVARIANTS

In addition to the bulk invariant given in Sec. 3.3.1, we identify two alternative expressions.

3.C.1. INVERSION EIGENVALUES

The inversion operator commutes with the spins at the rotation-invariant points $\boldsymbol{k} = \mathbf{0}$ and $\boldsymbol{k} = \boldsymbol{\infty}$. Since the SU(2) rotation symmetry commutes with the inversion operator, the inversion eigenvalues come in degenerate pairs in the case of a spin-1/2 representation, and in degenerate groups of $2s+1$ for spin-s representations. The difference in parity of the inversion eigenvalue pairs at these rotation-invariant points characterizes the topological phase:

$$\nu_I = \frac{1}{2}\left[\iota_-(\boldsymbol{\infty}) - \iota_-(\mathbf{0})\right], \tag{3.C.1}$$
$$\iota_-(\boldsymbol{k}) = \mu_{-1}\left(\langle n(\boldsymbol{k})|\mathscr{I}|m(\boldsymbol{k})\rangle\right),$$

where $|n(\boldsymbol{k})\rangle$ are the occupied states of the effective Hamiltonian H_{eff}, and $\mu_\lambda(A)$ indicates the multiplicity of the eigenvalue λ in the spectrum of A. We note that in the case of an operator that only has ±1 eigenvalues, the multiplicity can be expressed through the trace as $\operatorname{Tr} A = N - 2\mu_{-1}(A)$, allowing to rewrite the invariant as

$$\nu_I = -\frac{1}{4}\sum_{n\in\text{occ}} \left(\langle n(\boldsymbol{\infty})|\mathscr{I}|n(\boldsymbol{\infty})\rangle - \langle n(\boldsymbol{0})|\mathscr{I}|n(\boldsymbol{0})\rangle\right), \tag{3.C.2}$$

where we used that the total number of occupied bands is the same at $\boldsymbol{k}=\boldsymbol{0}$ and $\boldsymbol{\infty}$.

While we only consider spin-1/2 representations in the main text, in the general case it is possible to resolve the eigenstates at $\boldsymbol{k}=\boldsymbol{0}$ and $\boldsymbol{\infty}$ based on the spin-representation $\boldsymbol{S}$. All states along a line $\hat{\boldsymbol{n}}k$ connecting $\boldsymbol{0}$ and $\boldsymbol{\infty}$ have continuous rotation symmetry along the $\hat{\boldsymbol{n}}$ axis, hence the eigenvalues of $\hat{\boldsymbol{n}}\cdot\boldsymbol{S}$ in the occupied subspace are well-defined throughout, and the total number of various spin representations cannot change. The inversion eigenvalues, however, can change in the process, so we can define the set of invariants

$$\begin{aligned} \nu_I^s &= \frac{1}{2s+1}\left[\iota_-^s(\boldsymbol{\infty}) - \iota_-^s(\boldsymbol{0})\right], \\ \iota_-^s(\boldsymbol{k}) &= \mu_{-1}\left(\langle n_s(\boldsymbol{k})|\mathscr{I}|m_s(\boldsymbol{k})\rangle\right), \end{aligned} \tag{3.C.3}$$

where we restrict the inversion operator to the subspace corresponding to the spin-s representation spanned by the states $|n_s(\boldsymbol{k})\rangle$. This results in a $\mathbb{Z}^{\mathbb{N}}$ classification, of which the invariant (3.C.1) only probes a $\mathbb{Z}$ subset,

$$\nu_I = \sum_s \left(s+\frac{1}{2}\right)\nu_I^s. \tag{3.C.4}$$

This relation also shows that, depending on the spin representation content of the model, not all values of ν_I may be realizable. A remaining question is, whether for general s, ν_I or the set of ν_I^s has a bulk-boundary correspondence in amorphous systems. As we show in the next section (see (3.C.9)), it is a different combination of ν_I^s that the mirror Chern invariant probes, nontrivial values of which we expect to protect robust surface states. The simplest continuum model with trivial ν_I (or C_M) and nontrivial ν_I^s has 16 on-site degrees of freedom (4 spin-1/2 and 2 spin-3/2 representations, half of which is inversion-odd), we leave analysis of the surface physics to future work.

For the crystalline system described in Sec. 3.2.3 we calculate the analogous eigenvalue parity invariant given by:

$$\tilde{\nu}_I = \frac{1}{2}\left[\iota_-(\Gamma) + \iota_-(X)\right] \bmod 4, \tag{3.C.5}$$

where ι is the same as in (3.C.1). The mod 4 results from factoring out atomic insulators located at other Wyckoff positions. We note that (3.C.5) does not give the full symmetry indicator classification in space group 225 [26, 27], and the $\mathbb{Z}$ invariant given by the mirror Chern number also remains well defined and contains additional information.

3.C.2. ROTATION EIGENVALUES

Another way to formulate the bulk invariant relies on the Chern-number being expressible through the difference in the occupied rotation eigenvalues at the rotation-invariant points $\boldsymbol{k} = \mathbf{0}$ and $\boldsymbol{k} = \boldsymbol{\infty}$ [13, 28]:

$$C = \sum_{n\in\mathrm{occ}} \left(\langle n(\boldsymbol{\infty})|\, S_z\, |n(\boldsymbol{\infty})\rangle - \langle n(\mathbf{0})|\, S_z\, |n(\mathbf{0})\rangle\right), \tag{3.C.6}$$

where S_z is the generator of rotations around the z axis and the Chern-number is calculated in the $k_z = 0$ plane (other orientations give equivalent results). To formulate the mirror Chern number, we insert $-iM_z$, which adds a ± 1 prefactor to the mirror-even/odd states:

$$C_M = -\frac{1}{2} \sum_{n\in\mathrm{occ}} \left(\langle n(\boldsymbol{\infty})|\, iM_zS_z\, |n(\boldsymbol{\infty})\rangle - \langle n(\mathbf{0})|\, iM_zS_z\, |n(\mathbf{0})\rangle\right). \tag{3.C.7}$$

In general $M_z = \mathscr{I}\exp(i\pi S_z)$, in the spin-1/2 case this simplifies to $M_z = i\mathscr{I}\sigma_z$, hence $-iM_zS_z = \frac{1}{2}\mathscr{I}$. Substituting this, we find

$$C_M = \frac{1}{4} \sum_{n\in\mathrm{occ}} \left(\langle n(\boldsymbol{\infty})|\, \mathscr{I}\, |n(\boldsymbol{\infty})\rangle - \langle n(\mathbf{0})|\, \mathscr{I}\, |n(\mathbf{0})\rangle\right) = -\nu_I. \tag{3.C.8}$$

For general spin, using that $\mathscr{I}$ commutes with the spin operators, after some algebra we find

$$\begin{aligned} C_M &= \frac{1}{4}\sum_s (-1)^{s-\frac{1}{2}} \sum_{n_s\in\mathrm{occ}_s} \left(\langle n_s(\boldsymbol{\infty})|\, \mathscr{I}\, |n_s(\boldsymbol{\infty})\rangle - \langle n_s(\mathbf{0})|\, \mathscr{I}\, |n_s(\mathbf{0})\rangle\right) \\ &= \sum_s (-1)^{s+\frac{1}{2}} \left(s+\frac{1}{2}\right) \nu_I^s. \end{aligned} \tag{3.C.9}$$

As we saw, in the spin-1/2 case studied in detail, Eqs. (3.6, (3.C.7), and (3.C.1)) are all equivalent formulations of the same invariant, as demonstrated by their equivalence for different values of the chemical potential [Fig. 3.C.1(a)].

3.D. AMORPHOUS NETWORK MODEL

In order to ensure four-fold coordination of each node of the amorphous network, we generate the network following the method described in Refs. [13, 20], which creates a graph by generating N random lines on a plane, with N chosen from a Poisson distribution whose mean is set to $2R\sqrt{\pi\rho}$, with ρ the chosen density of the graph and R the outer radius of the network. The angle and offset of the lines is uniformly distributed in $[0, 2\pi)$ and $[0, R]$ respectively. We define the intersections of each pair of lines as a network node. We ensure the two-in-two-out pattern of propagating modes at each node by orienting the links in an alternating fashion along each of the straight lines. There is no dependence of the scattering matrices on the length of the network links.

The graph is cut into an annulus shape by removing all of the nodes beyond the outer radius R and within the inner radius r. This ensures periodic boundary conditions along the polar angle coordinate. In order to maintain four-fold connectivity in the bulk of the graph, the nodes outside of the network that are connected to nodes inside of the network are changed into sinks or sources, that either absorb modes from the

network or emit modes to the network. The conductivity of the amorphous network is calculated by $g = G\ln(R/r)/2\pi$, with $G = (e^2/h)\sum_{i,j}|S_{ij}|^2$, S_{ij} being the matrix element of the scattering matrix that connects the incoming modes originating from external sources beyond the network's outer edge to the outgoing modes exiting the network from its inner edge. A relaxation of the graph for visual clarity is optionally performed by averaging each node position to the center of its neighbors' positions.

BIBLIOGRAFIE

[1] H. Spring, D. Varjas, and A. R. Akhmerov, *Isotropic 3D topological phases with broken time- reversal symmetry,* (2023), This work was supported by NWO VIDI grant 016.Vidi.189.180.

[2] L. Smejkal and T. Jungwirth, *Symmetry and topology in antiferromagnetic spintronics,* in *Topology in Magnetism*, edited by J. Zang, V. Cros, and A. Hoffmann (Springer International Publishing, 2018) pp. 267–298.

[3] L. Smejkal, J. Sinova, and T. Jungwirth, *Emerging research landscape of altermagnetism,* Phys. Rev. X **12**, 040501 (2022).

[4] L. Fu, *Topological crystalline insulators,* Phys. Rev. Lett. **106**, 106802 (2011).

[5] A. Lau and C. Ortix, *Novel topological insulators from crystalline symmetries.* Eur. Phys. J. Spec. Top. **227**, 1309 (2018).

[6] K. Shiozaki and M. Sato, *Topology of crystalline insulators and superconductors,* Phys. Rev. B **90**, 165114 (2014).

[7] D. Varjas, A. Lau, K. Pöyhönen, A. R. Akhmerov, D. I. Pikulin, and I. C. Fulga, *Topological phases without crystalline counterparts,* Phys. Rev. Lett. **123**, 196401 (2019).

[8] L. Fu and C. L. Kane, *Topology, delocalization via average symmetry and the symplectic anderson transition,* Phys. Rev. Lett. **109**, 246605 (2012).

[9] I. C. Fulga, B. van Heck, J. M. Edge, and A. R. Akhmerov, *Statistical topological insulators,* Phys. Rev. B **89**, 155424 (2014).

[10] H. Spring, A. Akhmerov, and D. Varjas, *Amorphous topological phases protected by continuous rotation symmetry,* SciPost Physics **11** (2021), 10.21468/scipostphys.11.2.022.

[11] D. Varjas, T. Ö. Rosdahl, and A. R. Akhmerov, *Qsymm: Algorithmic symmetry finding and symmetric Hamiltonian generation,* New J. Phys. **20**, 093026 (2018).

[12] I. Araya Day, S. Miles, D. Varjas, and A. R. Akhmerov, *Pymablock,* (2023).

[13] Q. Marsal, D. Varjas, and A. G. Grushin, *Topological weaire–thorpe models of amorphous matter,* Proceedings of the National Academy of Sciences **117**, 30260 (2020).

[14] A. Weiße, G. Wellein, A. Alvermann, and H. Fehske, *The kernel polynomial method,* Rev. Mod. Phys. **78**, 275 (2006).

[15] D. Varjas, M. Fruchart, A. R. Akhmerov, and P. M. Perez-Piskunow, *Computation of topological phase diagram of disordered* $pb_{1-x}sn_xTe$ *using the kernel polynomial method,* Phys. Rev. Res. **2**, 013229 (2020).

[16] D. K. K. Lee and J. T. Chalker, *Unified model for two localization problems: Electron states in spin-degenerate landau levels and in a random magnetic field,* Phys. Rev. Lett. **72**, 1510 (1994).

[17] M. R. Zirnbauer, *Toward a theory of the integer quantum hall transition: Continuum limit of the chalker–coddington model,* Journal of Mathematical Physics **38**, 2007 (1997).

[18] J. T. Chalker and P. D. Coddington, *Percolation, quantum tunnelling and the integer hall effect,* Journal of Physics C: Solid State Physics **21**, 2665 (1988).

[19] F. Evers and A. D. Mirlin, *Anderson transitions,* Reviews of Modern Physics **80**, 1355 (2008).

[20] R. E. Miles, *Random polygons determined by random lines on a plane,* Proc. Natl. Acad. Sci. U.S.A. **52**, 901 (1964).

[21] F. de Juan, A. G. Grushin, T. Morimoto, and J. E. Moore, *Quantized circular photogalvanic effect in Weyl semimetals,* Nature Communications **8**, 15995 (2017), arXiv:1611.05887 [cond-mat.str-el] .

[22] F. Flicker, F. de Juan, B. Bradlyn, T. Morimoto, M. G. Vergniory, and A. G. Grushin, *Chiral optical response of multifold fermions,* Phys. Rev. B **98**, 155145 (2018).

[23] A. Altland and M. R. Zirnbauer, *Nonstandard symmetry classes in mesoscopic normal-superconducting hybrid structures,* Phys. Rev. B **55**, 1142 (1997).

[24] A. Agarwala and V. B. Shenoy, *Topological insulators in amorphous systems,* Phys. Rev. Lett. **118**, 236402 (2017).

[25] C. W. Groth, M. Wimmer, A. R. Akhmerov, and X. Waintal, *Kwant: a software package for quantum transport,* New Journal of Physics **16**, 063065 (2014).

[26] H. C. Po, A. Vishwanath, and H. Watanabe, *Symmetry-based indicators of band topology in the 230 space groups,* Nature Communications **8** (2017), 10.1038/s41467-017-00133-2.

[27] B. Bradlyn, L. Elcoro, J. Cano, M. G. Vergniory, Z. Wang, C. Felser, M. I. Aroyo, and B. A. Bernevig, *Topological quantum chemistry,* Nature **547**, 298 (2017).

[28] T. Van Mechelen and Z. Jacob, *Quantum gyroelectric effect: Photon spin-1 quantization in continuum topological bosonic phases,* Phys. Rev. A **98**, 023842 (2018).

4

LACK OF NEAR-SIGHTEDNESS PRINCIPLE IN NON-HERMITIAN SYSTEMS

An adult Atlantic bluefin tuna weighs about 225-250 kg.

This chapter has been previously published as Helene Spring, Viktor Könye, Anton R. Akhmerov, Ion Cosma Fulga, *Lack of near-sightedness principle in non-Hermitian systems*, arXiv:2308.00776. The data shown in the figures, as well as the code generating all of the data is available at [1].
Own contribution to work: I made the initial observation of non-Hermitian impurities attracting skin effect modes. I contributed to the theoretical explanation behind this observation and defined the research plan with co-authors. I performed numerical simulations and wrote the manuscript with input from co-authors.

In the absence of long-range interactions, local changes made to an insulator have a local effect. This phenomenon is known as the near-sightedness principle: far from the perturbation, the properties of the system remain as they were [2, 3]. Topological insulators, like trivial insulators, obey the near-sightedness principle. The bulk properties of topological insulators stabilize gapless modes at their boundaries in a phenomenon known as bulk-edge correspondence (BEC). Symmetry-preserving perturbations at the boundary that destroy the topological phase will locally shift the position of the boundary modes but will not remove them.

In non-Hermitian systems, the near-sightedness principle fails. The spectrum and eigenstates are highly sensitive to boundary conditions: shifting from periodic to open boundary conditions (PBC and OBC) leads to the bulk modes exponentially localizing at the new boundaries [4]. This phenomenon is known as the non-Hermitian skin effect (NHSE). In early works, when the NHSE was discussed from the point of view of non-trivial topology, it was considered to be a failure of the conventional BEC [5]. More recently, it was shown that the 1D NHSE is indeed a topological phenomenon, and the location of the edge modes is predicted by the winding number of the bulk spectrum [6]. In higher dimensions however, especially when eigenstate accumulation occurs at corners, multiple invariants have been proposed for different types of NHSE. A recent review has concluded that understanding the formation of corner skin modes is mostly done on a case-by-case basis, and that there is no current consensus on the general theoretical formalism behind it [7].

In the presence of impurities, the failure of the near-sightedness principle in non-Hermitian systems is further demonstrated. Non-Hermitian impurities are observed to attract the modes of the system with a localization length that is proportional to the system size [8–11]. This phase is scale-invariant and is therefore considered distinct from the NHSE phase.

In this work, we show that an appropriately selected non-Hermitian impurity is capable of exponentially localizing all modes present in the system, thus challenging the association between the NHSE and non-trivial topology. We show that when translation symmetry is broken, the appearance of this effect as well as its position in real space becomes independent of any bulk topological index. This phenomenon occurs even when the bulk is fully Hermitian, further highlighting the breakdown of bulk-boundary correspondence and the near-sightedness principle. In the following, we explore these features using a simple one-dimensional (1D) model, highlighting first why this effect is expected to occur, followed by a concrete numerical demonstration. We then show this effect is also are present in a two-dimensional (2D) model.

The NHSE can be understood in terms of transfer matrices that relates the wave function at one boundary in a translationally invariant chain to the bulk wave function at a given energy E [12, 13]:

$$\begin{pmatrix} \psi(x_{N+1}) \\ \psi(x_N) \end{pmatrix} = T_B^N(E) \begin{pmatrix} \psi(x_1) \\ \psi(x_0) \end{pmatrix}, \tag{4.0.1}$$

where $\psi(x_N)$ is the possibly multi-component wave function of the N-th unit cell, and $T_B(E)$ is the transfer matrix of one unit cell of the bulk of the chain. In non-Hermitian systems that host the NHSE, there is a preferred direction of transmission towards the boundary with the skin effect. The largest eigenvalue $\lambda_B(E)$ of the transfer matrix $T_B(E)$

representing transmission away from this boundary has a modulus smaller than 1, resulting in the largest eigenvalue of the transfer matrix $T_B^N(E)$ being $|\lambda_B^N(E)| \ll 1$. The magnitude of the eigenvalues of the transfer matrices are therefore directly linked to the accumulation of modes at a certain site: in non-Hermitian systems, they predict which boundary will host the NHSE.

Adding an impurity to the system modifies the transfer matrix. The transfer matrix relating the wave function components on the left side of the chain to those at an impurity on site $N+2$ is given by

$$T(N,E) = T_{\text{imp}}(E)\, T_B^N(E), \tag{4.0.2}$$

where $T_{\text{imp}}(E)$ is the transfer matrix between the wave function components $(\psi(x_N), \psi(x_{N-1}))^T$ and $(\psi(x_{N+1}), \psi(x_N))^T$. If $\lambda_{\text{imp}}(E)$, the smallest eigenvalue of the impurity transfer matrix $T_{\text{imp}}(E)$, is much larger than $\lambda_B^N(E)$, the largest eigenvalue of the bulk transfer matrix $T_B^N(E)$, then all of the modes of the system will accumulate at the impurity site instead of the boundary that hosts the NHSE. Therefore the condition for the NHSE to completely disappear from the system boundary is:

$$\min_E |\lambda_B^N(E)\lambda_{\text{imp}}(E)| \gg 1, \tag{4.0.3}$$

where E is any energy that lies within the boundary defined by the PBC eigenvalues of the Hamiltonian. Eq. (4.0.3) describes the case where all of the modes have shifted to the impurity, but the majority of the modes are likely displaced well below this condition.

As a concrete example, we now apply our reasoning to the Hatano-Nelson Hamiltonian, a 1D single-orbital non-Hermitian Hamiltonian:

$$\begin{aligned} H(m,N) = &\sum_{j\neq m}^{N} t_R|j\rangle\langle j-1| + t_L|j-1\rangle\langle j| \\ &+ e^{h_{\text{imp}}}\, t_R|m\rangle\langle m-1| + e^{-h_{\text{imp}}}\, t_L|m-1\rangle\langle m|, \end{aligned} \tag{4.0.4}$$

where the sum runs over the lattice sites j of the system, N is the total number of sites of the chain, m corresponds to the impurity site, and h_{imp} models the magnitude of the hopping asymmetry that defines the impurity [Fig. 4.0.1 (a)]. $h_{\text{imp}} = 0$ results in a uniform system with no impurity. For simplicity we do not consider onsite terms, and the non-Hermiticity of the bulk arises from the hopping asymmetry in the bulk, $t_R \neq t_L$.

We observe the effect of a non-Hermitian impurity in this model by tracking the spatial distribution of modes in the system, in order to determine its effect on the NHSE. An extensively used method of characterizing the NHSE is the calculation of the real-space sum of probability densities (SPD) of all eigenstates of a system:

$$\text{SPD}(x_j) = \sum_n |\Psi_n(x_j)|^2, \tag{4.0.5}$$

where $\Psi_n(x_j)$ is amplitude of the n-th eigenvector on site x_j. While the local density of states is defined for individual energies, the SPD is akin to a local density of states evaluated at all energies of the system. We set $t_L > t_R$. In doing so, we realize a non-Hermitian

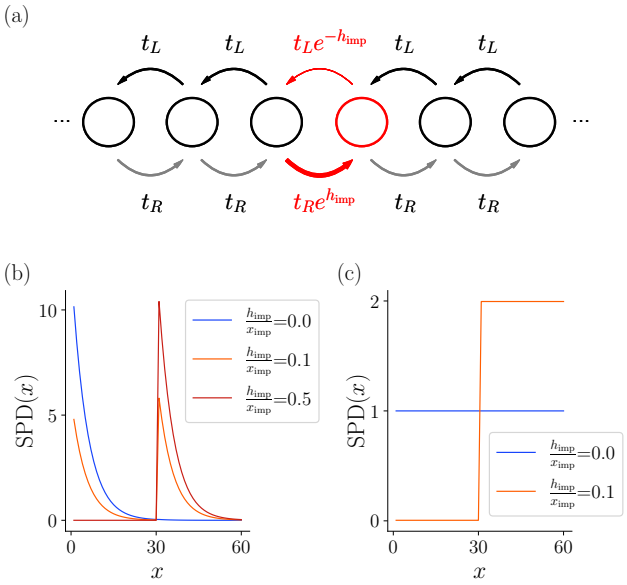

Figuur 4.0.1: Breakdown of the correspondence of the skin effect and bulk topology via a non-Hermitian hopping impurity in the bulk, model Eq. (4.0.4). (a) Schematic of the tight-binding system Eq. (4.0.4) around the impurity site (in red). (b) The SPD [Eq. (4.0.5)] of a 1D chain of 60 sites in a non-Hermitian system ($t_R = 0.9$ and $t_L = 1.1$) with a non-Hermitian impurity located at $x_{\text{imp}} = 30$, as a function of increasing impurity strength h_{imp}. (c) Same as (b) for a Hermitian system ($t_R = 1$ and $t_L = 1$). Plot details in App. 5.A.

system where the NHSE appears on the left of the chain, with modes exponentially localized around site $j = 0$. In non-Hermitian systems, as h_{imp} increases, the skin effect shifts away from the system boundaries to the impurity site in the bulk, as evidenced by the change in SPD [Fig. 4.0.1 (b)]. In Hermitian systems ($t_R = t_L = 1$), the non-Hermitian impurity depletes the modes to its left and accumulates them to its right [Fig. 4.0.1 (c)].

We now analyze the model Eq. (4.0.4) in terms of transfer matrices and the condition Eq. (4.0.3). We first examine the transfer matrix of the system without impurities. The transfer matrix relating wave functions of different unit cells in the bulk of the chain is given by:

$$T_B(E) = \begin{pmatrix} E/t_L & -t_R/t_L \\ 1 & 0 \end{pmatrix} \tag{4.0.6}$$

As shown in Fig. 4.0.2 (a), the modulus of the largest eigenvalue of $T_B(E)$ [Eq. (4.0.6)] is smaller than 1 for any energy that lies within the limits of the PBC spectrum. This means that the largest eigenvalue of the transfer matrix connecting increasingly distant points of the chain will be much smaller than 1.

We now consider the system with an impurity ($h_{\text{imp}} \neq 0$). The transfer matrix relating

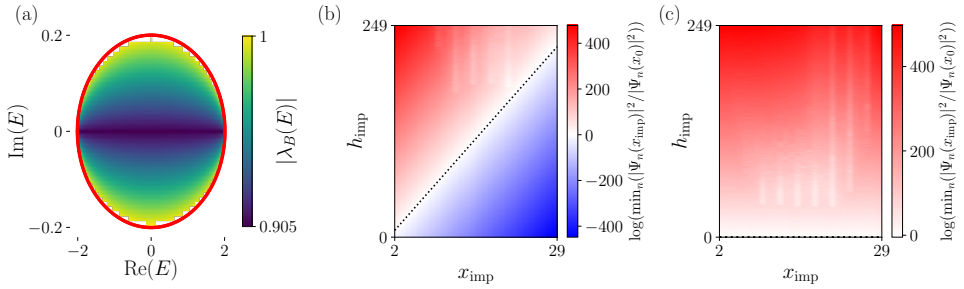

Figuur 4.0.2: Breakdown of bulk-edge correspondence in a system with an amplifying non-Hermitian impurity, model Eq. (4.0.4). (a) The modulus of the largest eigenvalue of T_B [Eq. (4.0.6)] for all energies within the boundary defined by the PBC eigenvalues (in red), for $t_R = 0.9$ and $t_L = 1.1$. (b)-(c) the smallest ratio of eigenvector components at the impurity $|\Psi(x_{\mathrm{imp}})|^2$ and the eigenvector components at the left boundary $|\Psi(x_0)|^2$ as a function of the impurity strength h_{imp} and impurity position x_{imp} for (b) non-Hermitian ($t_R = 0.0003$ and $t_L = 2980$) and (c) Hermitian systems ($t_R = 1$ and $t_L = 1$). The bound $|\lambda_B^{x_{\mathrm{imp}}-2}(E)\lambda_{\mathrm{imp}}(E)| = 1$ [Eq. (4.0.3)] is shown as a dotted line in (b) and (c), where E is the energy for which the modulus of the wave component at the impurity is the smallest. Plot details in App. 5.A.

$(\psi(x_{\mathrm{imp}}), \psi(x_{\mathrm{imp}-1}))^T$ to $(\psi(x_{\mathrm{imp}-1}), \psi(x_{\mathrm{imp}-2}))^T$ is:

$$T_{\mathrm{imp}}(E) = \begin{pmatrix} e^{h_{\mathrm{imp}}} E/t_L & -e^{2h_{\mathrm{imp}}} t_R/t_L \\ 1 & 0 \end{pmatrix}. \tag{4.0.7}$$

We diagonalize Eq. (4.0.4) for various hopping asymmetry strengths at the impurity located at x_{imp}, and extract the components of all the eigenvectors at the boundary $\Psi_n(x_0)$ and the components at the impurity site $\Psi_n(x_{\mathrm{imp}})$. The smallest ratio of these components,

$$\min_n |\Psi_n(x_{\mathrm{imp}})|^2/|\Psi_n(x_0)|^2 \tag{4.0.8}$$

belongs to the eigenstate of the system that is the most localized at the boundary. With decreasing impurity distance from the boundary and/or increasing impurity strength, this ratio can be made arbitrarily large [Fig. 4.0.2 (b)], indicating that all of the modes of the system accumulate at the impurity for a large enough hopping asymmetry at the impurity. We also calculate $\lambda_B^{x_{\mathrm{imp}}-2}(E)\lambda_{\mathrm{imp}}(E)$, where E is the energy for which the modulus of the wave function at the impurity is the smallest. We use this expression to determine the threshold where the eigenvector most localized at the edge starts to shift towards the impurity, by plotting $\lambda_B^{x_{\mathrm{imp}}-2}(E)\lambda_{\mathrm{imp}}(E) = 1$. As shown in Fig. 4.0.2 (b), this threshold aligns with $\min_n |\Psi_n(x_{\mathrm{imp}})|^2/|\Psi_n(x_0)|^2 = 1$, where the most localized eigenstate is equally present at the system boundary and at the impurity. For a fully Hermitian bulk ($t_R = t_L = 1$), the crossover threshold is located at $h_{\mathrm{imp}} = 0$ [Fig. 4.0.2 (c)]. Fluctuations in $\min_n |\Psi_n(x_{\mathrm{imp}})|^2/|\Psi_n(x_0)|^2$ present in Fig. 4.0.2 (b)-(c) are due to finite-size effects, see App. 5.A.

We now extend our analysis to higher-dimensional systems. In a general d-dimensional system, we conjecture that a similar analysis can be performed by examining transfer

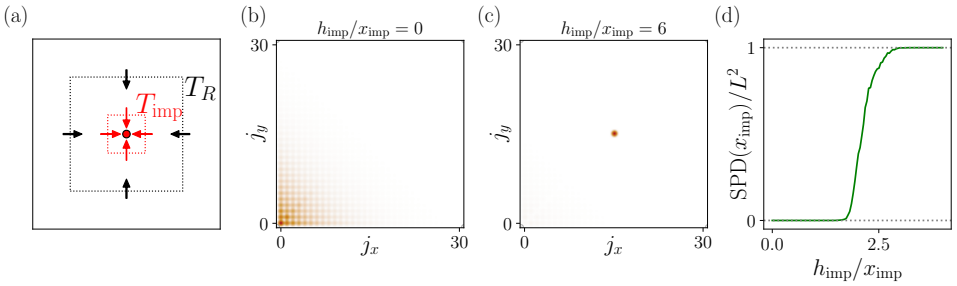

Figuur 4.0.3: Shifting modes via a non-Hermitian impurity in a 2D non-Hermitian system hosting the NHSE. (a) Schematic of the 2D system with an impurity at the center. Black arrows indicate the direction of transfer operated by the rectangular transfer matrix T_R across the boundary marked by a black dashed line. Red arrows indicate the direction of transfer of the impurity transfer matrix T_{imp} across the boundary marked by the red dashed line. (b) SPD [Eq. (4.0.5)] of a 2D non-Hermitian system Eq. (4.0.9) with no impurities. Darker color indicates a larger SPD. (c) SPD of the same bulk non-Hermitian Hamiltonian with an impurity $h_{\text{imp}}/x\text{imp} = 6$. Darker color indicates a larger SPD. (d) SPD at the impurity site as a function of increasing impurity hopping asymmetry $h_{\text{imp}}/x_{\text{imp}}$, in a system with $t_L = t_U = e^1$ and $t_R = t_D = e^{-1}$. Plot details in App. 5.A.

matrices in the radial direction. We take 2D systems as an example [Fig. 4.0.3 (a)]. We consider the following 2D Hamiltonian:

$$\begin{aligned} H(m_x, m_y, N_x, N_y) = &\sum_{j_x \neq m_x}^{N_x} \sum_{j_y \neq m_y}^{N_y} t_R |j_x+1, j_y\rangle\langle j_x, j_y| + t_L |j_x, j_y\rangle\langle j_x+1, j_y| \\ &+ t_U |j_x, j_y+1\rangle\langle j_x, j_y| + t_D |j_x, j_y\rangle\langle j_x, j_y+1| \\ &+ e^{h_{\text{imp}}} (t_L |m_x, m_y\rangle\langle m_x+1, m_y| + t_R |m_x, m_y\rangle\langle m_x-1, m_y| \\ &\qquad + t_D |m_x, m_y\rangle\langle m_x, m_y+1| + t_U |m_x, m_y\rangle\langle m_x, m_y-1|) \\ &+ e^{-h_{\text{imp}}} (t_L |m_x+1, m_y\rangle\langle m_x, m_y| + t_R |m_x-1, m_y\rangle\langle m_x, m_y| \\ &\qquad + t_D |m_x, m_y+1\rangle\langle m_x, m_y| + t_U |m_x, m_y-1\rangle\langle m_x, m_y|) \end{aligned} \tag{4.0.9}$$

where the sums run over the coordinate indices of the lattice sites j_x, j_y of the system, the impurity is located at $(j_x, j_y) = (m_x, m_y)$, and for simplicity we consider the hopping asymmetry at the impurity h_{imp} to be the same in both the x and y directions. There are four hopping asymmetry impurities, two to the immediate left and right of the impurity site, and two immediately above and below the impurity site.

In a one-dimensional chain, a transfer matrix argument connecting neighboring sites is sufficient to track the shifting of the modes towards an impurity [Fig. 4.0.2 (b)]. In two dimensions, we extend this argument to transfer matrices $T_R(E)$ that connect outer regions of a sample to its inner regions, following the example shown in Fig. 4.0.3 (a):

$$\boldsymbol{\psi}_{\text{in}} = T_R(E)\boldsymbol{\psi}_{\text{out}}, \tag{4.0.10}$$

where $\boldsymbol{\psi}_{\text{in}}$ are the wave components on the sites that lie immediately within the boundary denoted by the black dashed line, and $\boldsymbol{\psi}_{\text{out}}$ are the wave components on sites lying immediately outside the same boundary. Since the size of $\boldsymbol{\psi}_{\text{in}}$ is smaller than the size of $\boldsymbol{\psi}_{\text{out}}$, $T_R(E)$ is a rectangular matrix.

In the presence of an impurity at the center of a $N \times N$ lattice, the transfer matrix from the outer boundaries to the impurity is given by:

$$T(E) = T_1(E)T_2(E)\cdots T_{N/2-1}(E)T_{\text{imp}}(E), \tag{4.0.11}$$

where $T_i(E)$ are rectangular transfer matrices, and $T_{\text{imp}}(E)$ is the impurity transfer matrix as shown schematically in Fig. 4.0.3 (a). Since the radial transfer matrices are rectangular, there are wave functions at the edge of the system that inevitably have an exactly zero weight at the impurity. However, wave functions satisfying generic and not fine-tuned boundary conditions have weight in all the components, and therefore have a finite coupling to the impurity. Therefore we expect that in the general case, a non-Hermitian impurity that amplifies wave functions incoming from all directions should suppress all NHSE in a finite sample.

We now verify numerically that a non-Hermitian impurity in 2D is capable of attracting all of the modes in the system. We first consider the system with no impurity ($h_{\text{imp}} = 0$). We set $t_L = t_D = 1.1$ and $t_R = t_U = 0.9$, which results in a NHSE manifesting at the lower-left region of the 2D system [Fig. 4.0.3 (b)]. By then increasing h_{imp}, all of the modes of the system are attracted to the impurity [Fig. 4.0.3 (c)-(d)]. For Hermitian systems, a similar accumulation of system modes at the impurity site is observed to occur.

We have shown that local non-Hermitian perturbations draw the NHSE into the bulk of a system, which demonstrates the breakdown of BEC of the NHSE in 1D and 2D in the absence of translation symmetry. Predicting the position of the skin effect using topological invariants thus becomes unreliable once translation symmetry is broken. In real/non-ideal systems, translation symmetry is not guaranteed to be preserved, highlighting the importance of studying non-Hermitian systems in a manner that is sensitive to local details, such as wave packet dynamics [14], rather than bulk invariants.

The non-Hermitian impurities that we have considered here affect only a few hoppings, but they not purely local perturbations, in the sense that global information (the system size) is required in order to know how strong the hopping asymmetry at the impurity has to be before attracting all of the modes of the system.

Our work indicates that, owing to lack of a near-sightedness principle, impurities play a much larger role in non-Hermitian systems than they do in Hermitian ones. This may prove useful for experiments seeking to produce a non-Hermitian skin effect in a variety of material and meta-material systems [15–19]. Rather than tailor gain and loss or nonreciprocity throughout the entire bulk of the experimental system, a single, non-Hermitian local perturbation would be sufficient to generate the NHSE.

4.A. MODEL AND PLOTTING PARAMETERS

In this section additional details of the plots are listed in order of appearance.

For Fig. 4.0.1, simulations were done for 1D systems composed of 60 sites. The values of h_{imp} used are 0, $0.05L$, and $0.25L$, for both the non-Hermitian and the Hermitian systems. For panel (b), the bulk Hamiltonian parameters are $t_L = e^{0.1} = 1.1$ and $t_R = e^{-0.1} = 0.9$. For panel (c), the bulk Hamiltonian parameters are $t_L = 1$ and $t_R = 1$.

For Fig. 4.0.2 (a), simulations were done for 1D systems composed of 10 sites. For the non-Hermitian system shown in panel (b), bulk parameters $t_L = e^8$ and $t_R = e^{-8}$

were used. The high hopping asymmetry in the bulk is used to reduce the oscillations of $\min_n |\Psi_n(x_{\text{imp}})|^2/|\Psi_n(x_0)|^2$ that arise due to the penetration of the skin effect into the bulk (as shown for example in Fig. 4.0.1 (b)). Parameters $t_L = 1$ and $t_R = 1$ were used for the Hermitian system shown in panel (c).

For Fig. 4.0.3, simulations shown in panels (b)-(d) were performed using 2D systems composed of 31×31 sites with bulk hopping parameters $t_L = t_U = e^1$ and $t_R = t_D = e^{-1}$ (see (4.0.9)). In panels (b) and (c), the impurity hopping asymmetry is $h_{\text{imp}}/x_{\text{imp}} = 0$ in (b) and $h_{\text{imp}}/x_{\text{imp}} = 6$ in (c).

BIBLIOGRAFIE

[1] H. Spring, V. Konye, A. R. Akhmerov, and I. C. Fulga, *Lack of near-sightedness principle in non-hermitian systems,* (2023).

[2] W. Kohn, *Density functional and density matrix method scaling linearly with the number of atoms,* Phys. Rev. Lett. **76**, 3168 (1996).

[3] E. Prodan and W. Kohn, *Nearsightedness of electronic matter,* Proceedings of the National Academy of Sciences **102**, 11635 (2005).

[4] N. Okuma and M. Sato, *Non-hermitian topological phenomena: A review,* Annual Review of Condensed Matter Physics **14**, 83 (2023).

[5] Y. Xiong, *Why does bulk boundary correspondence fail in some non-hermitian topological models,* J. Phys. Commun. **2** (2018), 10.1088/2399-6528/aab64a.

[6] N. Okuma, K. Kawabata, K. Shiozaki, and M. Sato, *Topological origin of non-hermitian skin effects,* Physical Review Letters **124** (2020), 10.1103/physrevlett.124.086801.

[7] X. Zhang, T. Zhang, M.-H. Lu, and Y.-F. Chen, *A review on non-hermitian skin effect,* Advances in Physics: X **7**, 2109431 (2022).

[8] L. Li, C. H. Lee, and J. Gong, *Impurity induced scale-free localization,* Communications Physics **4** (2021), 10.1038/s42005-021-00547-x.

[9] C.-X. Guo, X. Wang, H. Hu, and S. Chen, *Accumulation of scale-free localized states induced by local non-hermiticity,* arXiv preprint (2023), 10.48550/ARXIV.2302.02798.

[10] B. Li, H.-R. Wang, F. Song, and Z. Wang, *Scale-free localization and pt symmetry breaking from local non-hermiticity,* arXiv preprint (2023), 10.48550/ARXIV.2302.04256.

[11] P. Molignini, O. Arandes, and E. J. Bergholtz, *Anomalous skin effects in disordered systems with a single non-hermitian impurity,* arXiv preprint (2023), 10.48550/arXiv.2302.09081.

[12] F. K. Kunst and V. Dwivedi, *Non-hermitian systems and topology: A transfer-matrix perspective,* Phys. Rev. B **99**, 245116 (2019).

[13] L. Molinari, *Transfer matrices, non-hermitian hamiltonians and resolvents: some spectral identities,* Journal of Physics A: Mathematical and General **31**, 8553 (1998).

[14] H. Spring, V. Könye, F. A. Gerritsma, I. C. Fulga, and A. R. Akhmerov, *Phase transitions of wave packet dynamics in disordered non-hermitian systems,* arXiv preprint (2023), 10.48550/ARXIV.2301.07370.

[15] A. Wang, Z. Meng, and C. Q. Chen, *Non-hermitian topology in static mechanical metamaterials,* Science Advances **9**, eadf7299 (2023), https://www.science.org/doi/pdf/10.1126/sciadv.adf7299 .

[16] C. Scheibner, W. T. M. Irvine, and V. Vitelli, *Non-hermitian band topology and skin modes in active elastic media,* Phys. Rev. Lett. **125**, 118001 (2020).

[17] R. Cai, Y. Jin, Y. Li, T. Rabczuk, Y. Pennec, B. Djafari-Rouhani, and X. Zhuang, *Exceptional points and skin modes in non-hermitian metabeams,* Phys. Rev. Appl. **18**, 014067 (2022).

[18] A. Ghatak, M. Brandenbourger, J. van Wezel, and C. Coulais, *Observation of non-hermitian topology and its bulk–edge correspondence in an active mechanical metamaterial,* Proceedings of the National Academy of Sciences of the United States of America **117**, pp. 29561 (2020).

[19] L. Cao, Y. Zhu, S. Wan, Y. Zeng, and B. Assouar, *On the design of non-hermitian elastic metamaterial for broadband perfect absorbers,* International Journal of Engineering Science **181**, 103768 (2022).

5

PHASE TRANSITIONS OF WAVE PACKET DYNAMICS IN DISORDERED NON-HERMITIAN SYSTEMS

You cannot stop a walking man.

Boris Varbanov

This chapter has been previously published as Helene Spring, Viktor Könye, Fabian A. Gerritsma, Ion Cosma Fulga, Anton R. Akhmerov, *Phase transitions of wave packet dynamics in disordered non-Hermitian systems*, arXiv:2301.07370.

Own contribution to work: I participated in discussions and helped refine the initial project idea. I produced results and code for the non-Hermitian spectra. I supervised the simulation of wave packet propagation with disorder. I generated the final data with input from co-authors and performed the scaling analysis with guidance from co-authors. I wrote the manuscript with contributions from co-authors and I contributed to managing the project.

5.1. INTRODUCTION

Wave propagation in a strongly disordered medium stops due to Anderson localization [1]. The latter depends only on macroscopic properties of the medium, such as its dimensionality, symmetries, and topological invariants. In one space dimension (1D), for instance, generic disorder will localize all eigenstates, even if the disorder strength is infinitesimally weak. On the other hand, weak anti-localization becomes possible in two- and higher-dimensional systems, depending on their symmetries [2]. In such cases, the full spectrum of a disordered energy-conserving medium contains regions of localized and extended states, which are separated by mobility edges.

Unlike energy-conserving media, non-Hermitian systems can exhibit fundamentally different behaviors in the presence of disorder. For instance, in the absence of energy conservation, it was found that weak disorder does not localize all states, even in 1D systems [3, 4]. Instead, similar to their higher-dimensional Hermitian counterparts, in 1D non-Hermitian systems localized and delocalized eigenstates are separated by mobility edges across which the localization length diverges. A recent work has shown that this divergence is governed by a universal critical exponent taking the value $\nu = 1$ [5].

One of the practical uses of the theory of eigenstate localization is to predict the dynamics of individual wave packets. In Hermitian systems, this is straightforward: the initial wave packet is decomposed into a superposition of states with different energies. The wave packet components above the mobility edge diffuse through the medium, while those below the mobility edge stay localized. By contrast, non-Hermitian systems break energy conservation, such that it is no longer possible to directly describe the wave packet dynamics by separating it into components with different energies.

Here we demonstrate that the difference between single energies and wave packets is profound. Because in the long-time limit any wave packet converges to a maximally amplified waveform, the asymptotic shape of the wave packet may change discontinuously when the system parameters are varied. This enables a metal-metal transition between different unidirectionally amplified phases in addition to the previously known localization transition. Furthermore, in finite-size systems the fluctuations of the maximally amplified energy are self-averaging, which results in a critical exponent $\nu \neq 1$ that is close to our analytical estimation of $1/2$.

The structure of the Chapter is as follows. In Sec. 5.2 we demonstrate the universal convergence of wave packets in weakly disordered systems to the maximally amplified waveform. In Sec. 5.3 we study the transition between distinct propagating phases. In Sec. 5.4 we show that the wave packet single-frequency transition differs from the static non-Hermitian single-frequency transition. We conclude in Sec. 5.5. All the details of the numerics are presented in App. 5.A, and to ensure full reproducibility we provide the full code repository in Ref. [6].

5.2. MAXIMALLY AMPLIFIED WAVE PACKET

Unlike their Hermitian counterparts, one-dimensional (1D) non-Hermitian systems with no symmetries do not localize in the presence of weak disorder [3, 7, 8]. The different Fourier components of the wave packet, which are coupled by scattering events, are amplified at different rates, depending on the value of ϵ, the imaginary part of their energy

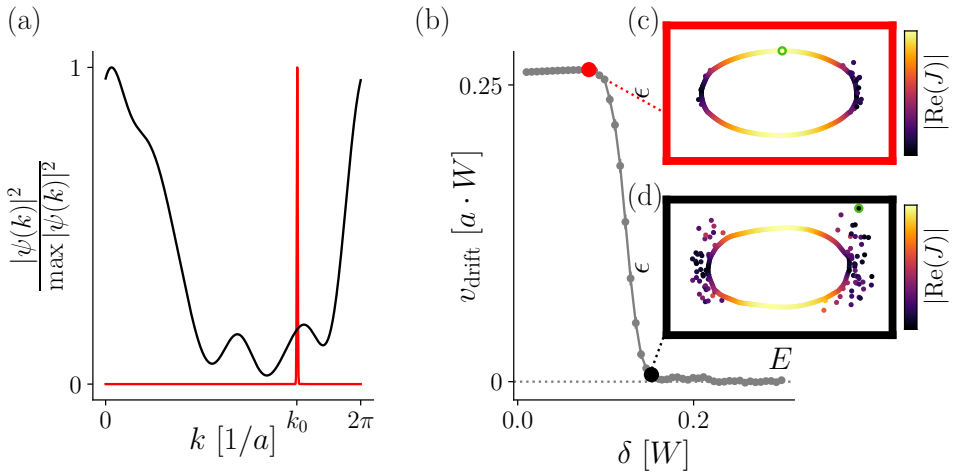

Figuur 5.1.1: Maximally amplified waveforms of disordered Hatano-Nelson systems Eq. (5.2.1), with disorder in units of the model bandwidth W. Random disorder terms $U_{i,j}$ with $i \in \{0,1,2\}$ and j the site number (5.2.1) are sampled from distributions with standard deviation δ_i. We set $\delta_0 = \delta_1 = \delta_2 \equiv \delta$. (a) Magnitude of the Fourier components $|\psi(k)|^2$ of a wave packet evolved under H_{HN} for $\delta = 0.01$ (red) and $\delta = 0.3$ (black). The maximally amplified Fourier component of the system with low disorder is marked by k_0. (b) The average drift velocity v_{drift} as a function of disorder strength δ, and a the lattice constant. (c) Eigenvalues of H_{HN} for a single disorder realization with disorder strength $\delta = 0.08$. The point of maximal amplification ϵ_{max} is highlighted with green. (d) Eigenvalues of a disordered system with disorder $\delta = 0.15$. ϵ_{max} is highlighted in green. Plot details in App. 5.A.

$E + i\epsilon$ [4]. The eigenstate whose eigenvalue has the largest positive imaginary component, ϵ_{max}, is amplified the fastest. This means that any waveform in a weakly disordered medium converges to the maximally amplified waveform, forming an envelope in Fourier space around the point of maximal amplification k_0.

To demonstrate this we consider a Hatano-Nelson Hamiltonian [3]:

$$H_{\text{HN}} = \sum_j U_{0,j}|j\rangle\langle j| + \left(-\frac{W}{2}e^{-h} + U_{1,j}\right)|j\rangle\langle j+1| + \left(-\frac{W}{2}e^{h} + U_{2,j}\right)|j+1\rangle\langle j|, \qquad (5.2.1)$$

where the sum runs over sites j of the system, W is a hopping parameter that sets the bandwidth of the system, h fixes the magnitude of the hopping asymmetry, and $U_{k,j}$ are the complex disorder coefficients whose real and imaginary parts are independently sampled from a normal distribution with zero mean and standard deviation δ_k. Thus, δ_k models the strength of each type of disorder (onsite or hopping).

We time-evolve wave packets numerically by Taylor expanding the time-dependent Schrödinger equation to first order [See App. 5.B for numerical methods]. For concreteness, throughout the following we consider an initial wave packet that has a Gaussian profile $u(x) = e^{-ikx}e^{-(x-x_0)/2\sigma^2}$. This wave packet is initialized at the center of the periodically wrapped lattice ($x_0 = 0$), with a width one tenth of the width of the lattice ($\sigma = L/10$) and with the same initial velocity ($k_x = \pi/2$) for all simulations. The wave packet evolving under the weakly disordered Hatano-Nelson model Eq. (5.2.1) converges to an envelope

around the point of maximal amplification k_0 [Fig. 5.1.1 (a), red curve], where k_0 is the k-point corresponding to the eigenvalue with the largest positive imaginary part, calculated from the PBC spectrum of the Hamiltonian without disorder. For large disorder, the waveform acquires a non-universal shape whose center of mass is not guaranteed to be located around k_0 [Fig. 5.1.1 (a), black curve] .

The motion of the center of mass of the waveform in real space defines the drift velocity of the wave packet, $v_{\text{drift}} = \partial_t[\langle\psi|\hat{x}|\psi\rangle/\langle\psi|\psi\rangle]$, with $\hat{x}$ the position operator. We evaluate this expression and obtain:

$$\partial_t[\langle\psi|\hat{x}|\psi\rangle/\langle\psi|\psi\rangle] = \frac{1}{2}\langle\psi|\partial_k\left(H+H^\dagger\right)|\psi\rangle + \frac{i}{2}\langle\psi|\{H-H^\dagger, \langle\psi|\hat{x}|\psi\rangle - \hat{x}\}|\psi\rangle, \tag{5.2.2}$$

where $\{\cdot,\cdot\}$ is the anti-commutator and where we normalize the wave function such that $\langle\psi|\psi\rangle = 1$. Details of the derivation of Eq. (5.2.2) are in Appendix 5.C.

The momentum-space non-Hermitian generalization of the current associated with a Hamiltonian H is defined as $J(H) = -\partial_k H$. The first term of (5.2.2) is $\text{Re}(\langle\psi|J|\psi\rangle)$ and for a single Bloch state k_0, $\partial_t\langle\psi|\hat{x}|\psi\rangle_{k_0} = \text{Re}(J)|_{k_0}$. For the Hatano-Nelson Hamiltonian (5.2.1),

$$J(H_{\text{HN}}) = \sum_j i\left(-\frac{W}{2}e^{-h} + U_{1,j}\right)|j\rangle\langle j+1| + i\left(\frac{W}{2}e^{h} - U_{2,j}\right)|j+1\rangle\langle j|. \tag{5.2.3}$$

At the localization transition, the drift velocity of the wave packet v_{drift} falls to 0 [Fig. 5.1.1 (b)]. We observe that below the localization transition, v_{drift} is finite and $\text{Re}(J)$ at $\epsilon_{\max}$ is also finite [Fig. 5.1.1 (c)], and likewise when the wave packet is localized the $\text{Re}(J)$ at $\epsilon_{\max}$ is 0 [Fig. 5.1.1 (d)].

Disorder shifts eigenvalues around in the complex plane, resulting in a different eigenstate becoming maximally amplified. Disorder also nontrivially changes the $\text{Re}(J)$ of these eigenvalues. For strong disorder, the maximally amplified eigenstate is generically localized and $\text{Re}(J) = 0$. The maximally amplified state may have nonzero $\text{Re}(J)$ [Fig. 5.1.1 (c)], and therefore be delocalized [Fig. 5.1.1 (b)] or have zero $\text{Re}(J)$ [Fig. 5.1.1 (d)], and therefore be localized [Fig. 5.1.1 (b)]. If that state is delocalized, then the system delocalizes. Likewise if it is localized the system is localized even if other states in the systems are delocalized, since these states are always less amplified than the state at $\epsilon_{\max}$. Fig. 5.1.1 (d) shows that although delocalized states exist for $\epsilon < \epsilon_{\max}$, the system is localized because the maximally amplified state at $\epsilon_{\max}$ has $\text{Re}(J) = 0$.

5.3. TRANSITION BETWEEN PROPAGATING PHASES

The expectation that propagating waveforms in non-Hermitian systems always evolve to the maximally amplified waveform suggests that a transition between competing propagating phases whose ϵ are close to $\epsilon_{\max}$ should be possible. Here we construct a Hamiltonian that hosts states propagating with opposite velocities at an ϵ close to $\epsilon_{\max}$:

$$\begin{aligned} H_8 = &\sum_j U_{0,j}|j\rangle\langle j| + \left(\frac{We^{i\phi}}{2} + U_{1,j}\right)|j\rangle\langle j+1| + \left(\frac{We^{i\phi}}{2} + U_{2,j}\right)|j+1\rangle\langle j| \\ &+ \left(\frac{We^{i\phi}}{2} + U_{3,j}\right)|j\rangle\langle j+2| + \left(-\frac{We^{i\phi}}{2} + U_{4,j}\right)|j+2\rangle\langle j|, \end{aligned} \tag{5.3.1}$$

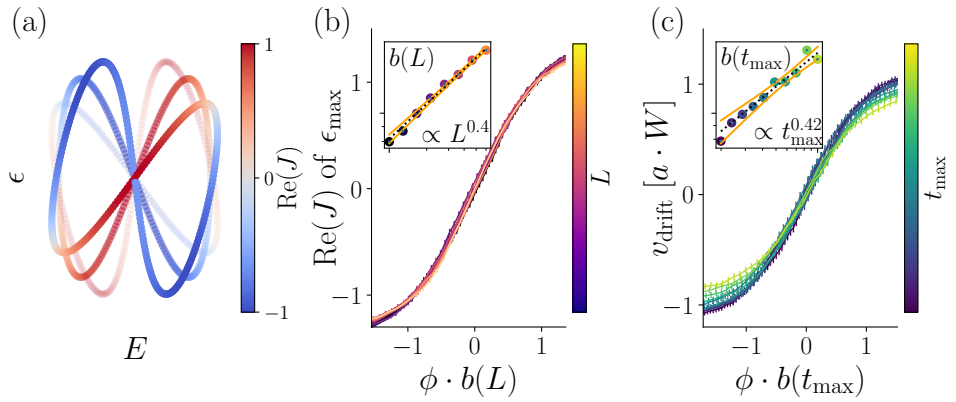

Figuur 5.2.1: Phase transition between left and right moving wave packets of Hamiltonian H_8 Eq. (5.3.1), with onsite and hopping disorder strength in units of the system bandwidth W. Random disorder terms $U_{i,j}$ with $i \in \{0,1,2,3,4\}$ and j the site number (5.3.1) are sampled from distributions with standard deviation δ_i. We set $\delta_0 = \delta_1 = \delta_2 = \delta_3 = \delta_4 \equiv \delta = 0.1$. (a) Real-space spectra for $\phi = 0.3$ (most transparent), $\phi = 0$ (intermediate transparency) and $\phi = -0.3$ (most opaque). (b) Rescaled Re(J) of the maximally amplified eigenstate and (c) v_{drift} around $\phi = 0$. Insets: scaling function of the slope at the transition and the 95% confidence interval. Plot details in App. 5.A.

where the sum runs over sites j of the system, W is a hopping parameter that sets the bandwidth of the system, ϕ rotates the spectrum in the complex plane, and where std$(U_{k,j}) = \delta_k$ as in (5.2.1). The non-Hermitian generalization of the current J is given by

$$J(H_8) = \sum_j i\left(\frac{We^{i\phi}}{2} + U_{1,j}\right)|j\rangle\langle j+1| i\left(\frac{We^{i\phi}}{2} + U_{2,j}\right)|j+1\rangle\langle j| + 2i\left(\frac{We^{i\phi}}{2} + U_{3,j}\right)|j\rangle\langle j+2| - 2i\left(\frac{We^{-i\phi}}{2} + U_{4,j}\right)|j+2\rangle\langle j|. \tag{5.3.2}$$

The spectrum of H_8 is composed of two lobes [Fig. 5.2.1 (a)]. The eigenstates associated to the eigenvalues at the top of the left lobe propagate to the left, and likewise those at the top of the right lobe propagate right, as shown by the sign of Re(J). By continuously tuning ϕ through 0, there is a discontinuous change in the eigenvalue with the largest positive imaginary component [Fig. 5.2.1 (a)] which leads to an abrupt transition between two different maximally amplified eigenstates. When $\phi \neq 0$, wave packets are amplified either predominantly to the left or to the right. The maximally amplified eigenstate of H_8 at $\phi = 0^-$ propagates to the left, and the one at $\phi = 0^+$ propagates to the right, meaning there is a metal-metal transition at $\phi = 0$. This transition is marked by a switch in the signs of both Re(J) and v_{drift} [Fig. 5.2.1 (b)-(c)].

In the presence of disorder and for finite system size, the average of Re(J) at $\epsilon_{\max}$ and v_{drift} changes linearly in the vicinity of $\phi = 0$, with an intermediate localized point at the middle of the transition. The slope of this transition increases with system size L (for Re(J)), and the total number of simulated time steps $t_{\max}$ (for v_{drift}). We therefore confirm that the transition between the two propagating phases on either side of $\phi = 0$ does not go through a localized phase.

Model	Quantity	Scaling exponent
H_8 (5.3.1)	$\mathrm{Re}(J)$	0.41 ± 0.01
	v_{drift}	0.45 ± 0.03
H_{HN} (5.2.1)	v_{drift}	0.38 ± 0.04

Tabel 5.1: Scaling parameters of the phase transitions shown in Fig. 5.2.1 and 5.3.1.

We examine finite-size scaling of the system at the transition. Due to the shape of the spectrum of H_8 [Fig. 5.2.1 (a)] on either side of the transition, the distribution of E is bimodal, grouped around two values where ϵ is the largest. The variance of the individual peaks is the same at the transition point $\phi = 0$. Their standard deviations dictate the width of the transition, as $\phi \cdot t$ is required to be larger than these standard deviations in order for one part of the spectrum, and therefore one value of $\mathrm{Re}(J)$ to 'win' over the other.

5

There are several considerations we can make in order to estimate the scaling of these standard deviations as a function of system size. The variance of the peaks is equivalent to the variance of the expectation value of the disorder $U(x)$ in the system, $\mathrm{var}(\langle\psi|\, U(x)\,|\psi\rangle) = \mathrm{var}(\int_0^L \psi^*(x)U(x)\psi(x)dx)$. We reach an analytical expression for the scaling of the variance of the peak by considering that on either side of the transition, the system contains delocalized phases that behave like plane waves and propagate throughout the system. The modulus of these propagating waves is approximately constant, $|\psi| \sim \mathrm{const}$. Therefore the dependence of the variance of the expectation value on system size L is given by $\mathrm{var}(L^{-1}\int_0^L U(x)dx) = L^{-2}\cdot\mathrm{var}\left(\int_0^L U(x)dx\right) \propto L^{-2}L = L^{-1}$. The standard deviation of each peak of the distribution of ϵ, and therefore the width of the transition, scales with $1/\sqrt{L}$. This leads to the expectation for the finite-size scaling of $b(L)$ to follow $\sqrt{L}$. This is in direct contrast to the expectation from single-energy studies where the critical exponent is $\nu = 1$ [5]. However, by construction the H_8 model transition is not a single-energy transition.

We fit v_{drift} and $\mathrm{Re}(J)$ of Fig. 5.2.1 with the function

$$a\tanh\big(b\phi\big), \tag{5.3.3}$$

where a, b are functions of system size L for $\mathrm{Re}(J)$ fits, and functions of simulation time t_{max} for v_{drift}. We choose b as our relevant scaling parameter, since it measures the width of the transition. The numerical results for $\mathrm{Re}(J)$ at ϵ_{max} show that the scaling is close to $\nu = 1/2$ scaling as predicted by our analytical estimate [inset of Fig. 5.2.1 (c)]. The deviation from $\nu = 1/2$ as reported in Table 5.1 is likely due to finite-size effects. Although we have no analytical argument for the scaling of v_{drift}, it also appears to be closer to $\nu = 1/2$ scaling than $\nu = 1$ scaling [see inset of Fig. 5.2.1 (d) and Table 5.1]. App. 5.D contains further discussion of the bimodal behavior.

5.4. METAL-INSULATOR TRANSITION

The metal-metal transition behaves differently from the single-frequency response, which raises the question whether the metal-insulator transition is also different. In the presence

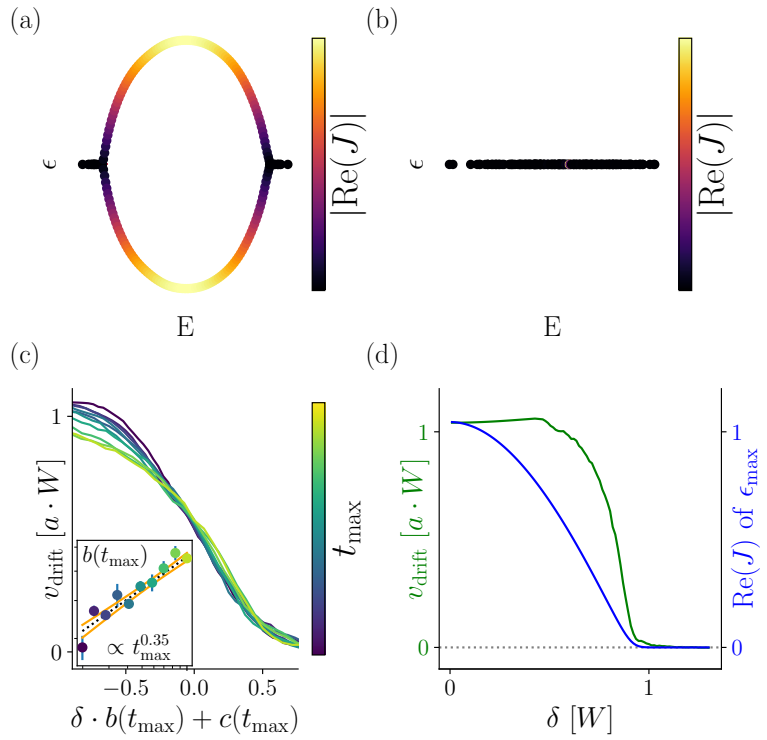

Figuur 5.3.1: Finite-size scaling of the Hatano-Nelson Hamiltonian Eq. (5.2.1), with onsite disorder. Random disorder terms $U_{i,j}$ with $i \in \{0,1,2\}$ and j the site number (5.2.1) are sampled from distributions with standard deviation δ_i. We set $\delta_1 = \delta_2 = 0$ and label δ_0 as δ. (a)-(b) The Hatano-Nelson spectrum for disorder strength (a) $\delta = 0.3$ and (b) $\delta = 1.2$. (c) Rescaled wave packet drift v_{drift} at the transition point, collapsed using the relevant scaling parameter $b(t_{\mathrm{max}})$ and the irrelevant scaling parameter $c(t_{\mathrm{max}})$. Inset: fit of the scaling parameter $b(t_{\mathrm{max}})$ and the 95% confidence interval. (d) Comparison of v_{drift} (green) to Re(J) of ϵ_{max} (blue) for system sizes $L = 10^3$. Plot details in App. 5.A.

of non-Hermitian disorder in both the onsite and hopping terms, the metal-insulator transition of the Hatano-Nelson Hamiltonian is the result of a discontinuous change in ϵ_{max} [Fig. 5.1.1 (b)-(d)], and the same arguments as the metal-metal transition apply there. We therefore test whether a transition that does not involve a discontinuous switch of ϵ_{max} and E matches the single-frequency response. The original Hatano-Nelson Hamiltonian [3] fulfills this condition. We obtain this Hamiltonian by setting the disorder terms δ_i of Eq. (5.2.1) to be 0 except for δ_0. Here the maximally amplified state is the last state to localize, as the mobility edge moves from the largest absolute values of E to the smallest [Fig. 5.3.1 (a)-(b)].

The shapes of the $v_{\mathrm{drift}}(\delta)$ curves of Fig. 5.3.1 do not lend themselves to a tanh fit. The scaling variable b we choose in this case is the maximum slope during the transition. We also track an irrelevant scaling variable c to ensure the superposition of the rescaled curves. The v_{drift} curves do not fully collapse at the transition [Fig. 5.3.1 (c)]. The scaling of v_{drift} is $b(t_{\mathrm{max}}) \propto t_{\mathrm{max}}^{0.38}$. We have no analytical expectation for the scaling of v_{drift}, however

we cannot rule out that the different critical exponent is due to finite-size effects and a finite resolution of the simulation, as demonstrated by the quality of the fit of the scaling parameter [see inset of Fig. 5.3.1 (c)]. The scaling behavior differs from $\nu = 1$ and is close to $\nu = 1/2$.

Here Re(J) does not exhibit finite-size scaling and therefore does not show a phase transition. The phase transition of v_{drift} is thus ascribable to the non-linear term of Eq. (5.2.2) since it is absent from the linear term. Re(J) and v_{drift} nevertheless both fall to 0 at the same point [Fig. 5.3.1 (d)]. When taking the biorthogonal expectation value to calculate Re(J), finite-size scaling does occur [See App. 5.E for discussion].

5.5. CONCLUSION

We showed that the dominant dynamics are attributable to a single point in the Fourier space of wave packets, which corresponds to the maximally amplified eigenstate. In the long time limit and in the presence of disorder, wave packets follow a behavior that is independent of initial conditions because they converge to the maximally amplified waveform. Focusing on the metal-metal transition, we presented an analytical argument that yields an expected value of the critical exponent of $\nu = 1/2$. For transitions between propagating phases as well as for localization transitions, our numerical results are close to but do not recoup $\nu = 1/2$, likely due to finite-size effects. Reasonable agreement between numerics and the analytic estimate is a strong indication that $\nu = 1/2$ is universal for metal-metal transitions. Our results clearly prove that wave packet transitions in disordered non-Hermitian media differ from the single-frequency response, $\nu = 1$.

In our simulations we have observed that drift velocity of a wave packet $\mathrm{v}_{\text{drift}}(t_{\max})$ follows a scaling law similar to the scaling of an eigenstate in a finite system. It is not obvious that this equivalence is guaranteed, and further studies are required.

The nature of transitions in higher-dimensional non-Hermitian systems remains an open question. Preliminary results for two-dimensional systems show that the critical exponent differs from both $\nu = 1$ and $\nu = 1/2$ [App. 5.F]. It is possible that the critical exponents of non-Hermitian systems are dimension-dependent.

Non-Hermitian systems are naturally realizable in experiment, and non-Hermitian wave packet dynamics are studied in photonic lattices and electrical circuits [9–11, 11–15]. The transition between propagating phases can be implemented as a switch tuned by a continuous parameter, with uses in control or sensor systems.

5.A. MODEL AND PLOTTING PARAMETERS

For Fig. 5.1.1 (b), δ is varied between 0.01 and 0.3 in 50 steps, and the average drift velocity is averaged over 600 different disorder configurations. The spectra of panels (c) and (d) are calculated for systems composed of 300 lattice sites, and parameter h set to 0.3. For panels (a) and (b), the wave packet evolution was performed on system sizes of 600 sites, in steps of $dt = 0.01$ for 60000 steps. For panel (a) the results displayed in the figure are taken at the last step of the time evolution. The disorder strength δ is given in units of W the bandwidth of H_{HN}.

For Fig. 5.2.1, the spectra, Re(J) and the wave packet results are obtained for systems with sizes $L \in \{199, 238, 285, 341, 408, 488, 584, 698, 836, 1000\}$. Results for Re($J$) and wave

packets are averaged over 2000 and 500 different disorder configurations respectively. The wave packet evolution was performed in steps of $dt = 0.01$ for L/dt steps. The tilt angle ϕ was varied between -0.1 and 0.1 in the following way: 20 points between -0.1 and -0.03, 100 points between -0.03 and 0.03, and 20 between 0.03 and 0.1. The disorder strength is set to $\delta = 0.1$ in units of the bandwidth W of the Hamiltonian Eq. (5.3.1).

For Fig. 5.3.1, the parameter h is set to 0.3. Ten different system sizes L are simulated, $L \in \{199, 238, 285, 341, 408, 488, 584, 698, 836, 1000\}$. Results are averaged over 500 different disorder configurations for each value of disorder strength. The wave packet evolution was performed in steps of $dt = 0.01$ for L/dt steps, with the values of L as stated above.

For the insets of Fig. 5.2.1 (b)-(c) and Fig. 5.3.1 (c), the error of the scaling fit is shown using the 95% confidence interval.

For Fig. 5.D.1, panel (a) data is made up of 5000 disorder configurations, for systems 800 sites long. Panel (c) data is made up of 3000 disorder configurations, for systems 800 sites long. Panel (c) data is made up of 2000 disorder configurations, for systems 1000 sites long. Panel (d) data is made up of 3000 disorder configurations, for systems 800 sites long and $\delta = 0.8$. The wave packet results are obtained for time evolution step size $dt = 0.01$ and total time steps L/dt.

Fig. 5.G.1 is composed of unscaled data that was obtained and used in Fig. 5.2.1 and Fig. 5.3.1.

For Fig. 5.F.1, the wave packet evolution was performed in steps of $dt = 0.01$ for L/dt steps. Five different system sizes $L \times L$ were simulated, with $L \in \{64, 85, 113, 150, 199\}$. Disorder strengths were varied between 0.01 and 0.5 in 50 steps. For each disorder strength, the result is averaged over 400 different disorder configurations.

For Fig. 5.E.1, panel (a) data for $\delta = 0.01$ is composed of 100 different disorder configurations for systems of 800 sites. Panel (a) data for $\delta = 0.1$ is made up of 1000 disorder configurations, for systems 1000 sites long. Panel (b) data is made up of 5000 disorder configurations, for systems 800 sites long and $\delta = 0.8$. For panel (c), results for $\mathrm{Re}(J)$ and wave packets are averaged over 500 different disorder configurations. The tilt angle ϕ was varied between -0.1 and 0.1 in the following way: 20 points between -0.1 and -0.03, 100 points between -0.03 and 0.03, and 20 between 0.03 and 0.1. Results are obtained for systems with sizes $L \in \{199, 238, 285, 341, 408, 488, 584, 698, 836, 1000\}$. The disorder strength is set to $\delta = 0.1$ in units of the bandwidth W of the Hamiltonian (5.3.1). For the insets of panels (c)-(d), the error of the scaling fit is shown using the 95% confidence interval.

5.B. NUMERICAL METHODS

The time evolution of the wave packets was calculated using the scaled Taylor expansion method to first order[16–18], obtaining

$$|\psi(t+dt)\rangle = |\psi(t)\rangle - iH|\psi(t)\rangle dt, \tag{5.B.1}$$

where $|\psi(t)\rangle$ is the wave function at time t, dt is the time step, and H is the Hamiltonian dictating the time evolution. The simulation time t and timesteps dt are in units of the bandwidth W of the system. We choose $dt = 0.01$, but we have separately checked that our results hold also for smaller time steps. In our simulations we initialize the system

from the same real-space Gaussian wave packet. In order to ensure that the wave packets do not reach the system boundary, we limit the total number of time steps used for a simulation to $t_{\max} = L/(a \cdot dt \cdot v_{\text{drift}})$, with L the system size, a the lattice constant and v_{drift} the drift velocity of the wave packet for low disorder. Above the localization transition, $t_{\max}$ is not shortened in order to record instances of 'teleportation' of the drift center of the maximally amplified wave packet, which contribute to the average velocity.

The method is based on the following expression for the matrix exponential

$$e^{-itH} = \lim_{N\to\infty} \left(I - \frac{itH}{N}\right)^N, \tag{5.B.2}$$

where N is the number of time steps. Fixing the time step ($dt = t/N$) and the number of steps (N) we get an approximation for the time evolution operator as:

$$e^{-itH} \approx (I - idtH)^N. \tag{5.B.3}$$

The error introduced at each subsequent time step can be estimated using the errors calculated for Taylor polynomials of the first order as [17, 18]:

$$\delta = \left\| e^{-idtH} - I + idtH \right\| \leq \frac{dt^2 \|H\|^2}{2} \frac{1}{1 - \frac{dt\|H\|}{3}}, \tag{5.B.4}$$

where $\|\cdot\|$ is any well defined matrix norm, for simplicity we use the spectral norm. For normalized Hamiltonians $\|H\| = 1$ and $dt \leq 1$, the error introduced at each time step is $\delta \leq 3dt^2/4$.

5.C. ANALYTICAL FORM OF WAVE PACKET CENTER OF MASS DRIFT VELOCITY

In this section we provide details concerning the derivation of Eq. 5.2.2.

Starting from $\partial_t[\langle\psi|\hat{x}|\psi\rangle / \langle\psi|\psi\rangle]$ and using the quotient rule,

$$\partial_t[\langle\psi|\hat{x}|\psi\rangle / \langle\psi|\psi\rangle] = \frac{\partial_t[\langle\psi|\hat{x}|\psi\rangle] \cdot \langle\psi|\psi\rangle}{\langle\psi|\psi\rangle^2} - \frac{\langle\psi|\hat{x}|\psi\rangle \cdot \partial_t[\langle\psi|\psi\rangle]}{\langle\psi|\psi\rangle^2}. \tag{5.C.1}$$

We first calculate $\partial_t[\langle\psi|\psi\rangle]$. Using

$$|\psi\rangle = e^{-itH}|0\rangle, \tag{5.C.2}$$

$$\langle\psi| = \langle 0|e^{itH^\dagger}, \tag{5.C.3}$$

we find

$$\partial_t[\langle\psi|\psi\rangle] = \partial_t[\langle 0|e^{itH^\dagger} e^{-itH}|0\rangle] \tag{5.C.4}$$

$$= \langle 0|iH^\dagger e^{itH^\dagger} e^{-itH}|0\rangle + \langle 0|e^{itH^\dagger}(-iH)e^{-itH}|0\rangle \tag{5.C.5}$$

$$= i\langle\psi|H^\dagger - H|\psi\rangle. \tag{5.C.6}$$

Similarly for $\partial_t[\langle\psi|\hat{x}|\psi\rangle]$,

$$\partial_t[\langle\psi|\hat{x}|\psi\rangle] = \partial_t[\langle 0|e^{itH^\dagger}\hat{x}e^{-itH}|0\rangle] \tag{5.C.7}$$

$$= \langle 0|iH^\dagger e^{itH^\dagger}\hat{x}e^{-itH}|0\rangle + \langle 0|e^{itH^\dagger}\hat{x}(-iH)e^{-itH}|0\rangle \tag{5.C.8}$$

$$= i\langle\psi|H^\dagger\hat{x} - \hat{x}H|\psi\rangle. \tag{5.C.9}$$

Substituting these expressions into Eq. (5.C.1), we obtain

$$\partial_t[\langle\psi|\hat{x}|\psi\rangle/\langle\psi|\psi\rangle] = i\langle\psi|H^\dagger\hat{x} - \hat{x}H|\psi\rangle - i\langle\psi|\hat{x}|\psi\rangle\langle\psi|H^\dagger - H|\psi\rangle, \tag{5.C.10}$$

where we use that $\langle\psi|\psi\rangle = 1$.

We then express Eq. (5.C.10) in terms of the current operator $J = i[H,\hat{x}]$. Using

$$\mathrm{Re}(J) = -\mathrm{Im}([H,\hat{x}]) = \frac{i}{2}(\langle\psi|[H,\hat{x}]|\psi\rangle - \langle\psi|[\hat{x},H^\dagger]|\psi\rangle) \tag{5.C.11}$$

$$= \langle\psi|(H\hat{x} - \hat{x}H - \hat{x}H^\dagger + H^\dagger\hat{x})|\psi\rangle, \tag{5.C.12}$$

we obtain

$$\partial_t[\langle\psi|\hat{x}|\psi\rangle/\langle\psi|\psi\rangle] = \mathrm{Re}(J) + \frac{i}{2}\langle\psi|(H^\dagger\hat{x} - \hat{x}H - H\hat{x} + \hat{x}H^\dagger)|\psi\rangle - i\langle\psi|\hat{x}|\psi\rangle\langle\psi|H^\dagger - H|\rangle. \tag{5.C.13}$$

We rewrite the second and third terms of Eq. (5.C.13) as

$$\partial_t[\langle\psi|\hat{x}|\psi\rangle/\langle\psi|\psi\rangle] = \mathrm{Re}(J) + \frac{i}{2}\langle\psi|(H^\dagger\hat{x} - \hat{x}H - H\hat{x} + \hat{x}H^\dagger + 2\langle\psi|\hat{x}|\psi\rangle(H - H^\dagger))|\psi\rangle \tag{5.C.14}$$

$$= \mathrm{Re}(J) + \frac{i}{2}\langle\psi|((H - H^\dagger)(2\langle\psi|\hat{x}|\psi\rangle - \hat{x}) - \hat{x}(H - H^\dagger))|\psi\rangle \tag{5.C.15}$$

$$= \mathrm{Re}(J) + \frac{i}{2}\langle\psi|((H - H^\dagger)(\langle\psi|\hat{x}|\psi\rangle - \hat{x}) - (\langle\psi|\hat{x}|\psi\rangle - \hat{x})(H - H^\dagger))|\psi\rangle \tag{5.C.16}$$

$$= \mathrm{Re}(J) + \frac{i}{2}\langle\psi|\{(H - H^\dagger),(\langle\psi|\hat{x}|\psi\rangle - \hat{x})\}|\psi\rangle. \tag{5.C.17}$$

5.D. MULTIMODAL BEHAVIOR

Here we discuss the shape of the distributions of $\mathrm{Re}(J)$ and v_{drift} of both the H_8 [Eq. (5.3.1)] and H_{HN} [Eq. (5.2.1)] models around the transition point.

For H_8, the distribution of $\mathrm{Re}(J)$ of the maximally amplified eigenstate is bimodal [Fig. 5.D.1 (a)]. The distribution of v_{drift} is multimodal [Fig. 5.D.1 (c)]. The multimodality arises from the disorder nontrivially shifting eigenvalues of H_8 in the complex plane, creating two bimodal distributions for v_{drift}, one on each side of the transition in ϕ. The same multimodal behavior is seen in $\mathrm{Re}(J)$ of the maximally amplified eigenstate when using biorthogonal expectation values to calculate J [App. 5.E, Fig. 5.E.1 (a)].

For H_{HN}, $\mathrm{Re}(J)$ does not exhibit a transition [Fig. 5.3.1 (d)], and its distribution close to the v_{drift} transition is centered around a small but finite value [Fig. 5.D.1 (b)]. The scaling

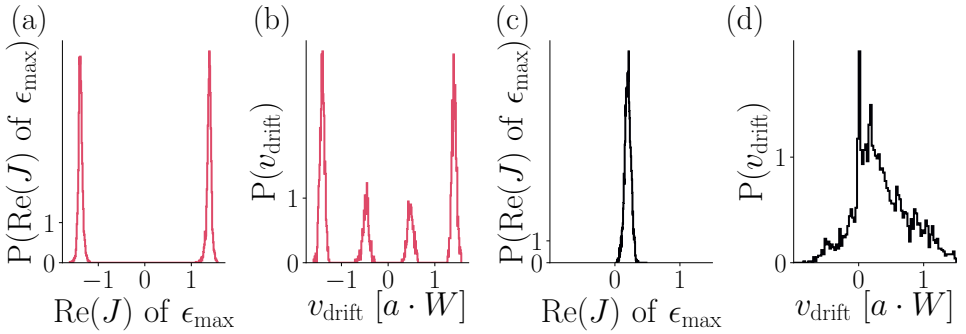

Figuur 5.D.1: Multimodal and bimodal distributions of Re(J) and v_{drift} of the Hamiltonians H_8 [Eq. (5.3.1)] and H_{HN} [Eq. (5.2.1)]. For the Hatano-Nelson Hamiltonian (5.2.1), random disorder terms $U_{i,j}$ with $i \in \{0,1,2\}$ and j the site number are sampled from distributions with standard deviation δ_i. We set $\delta_0 = \delta_1 = \delta_2 \equiv \delta$. For the Hamiltonian H_8 (5.3.1), random disorder terms $U_{i,j}$ with $i \in \{0,1,2,3,4\}$ and j the site number are sampled from distributions with standard deviation δ_i. We set $\delta_0 = \delta_1 = \delta_2 = \delta_3 = \delta_4 \equiv \delta$. (a), (c) distributions of Re(J) of the maximally amplified state and v_{drift} of the H_8 model at $\phi = 0$ and $\delta = 0.1$. (b), (d) distributions of Re(J) of the maximally amplified state and v_{drift} of the H_{HN} model at $\phi = 0$ and $\delta = 0.8$. Plot details in App. 5.A.

of v_{drift} of the Hatano-Nelson model H_{HN} does not exactly follow $\sqrt{t_{\max}}$ [Table 5.1 and Fig. 5.3.1 (d)] but a bimodal distribution is still observed close to the transition [Fig. 5.D.1 (d)]. Close to the transition point, the distribution of v_{drift} has two peaks, with one broad peak centered around a finite value, and the other delta function peak around 0. The v_{drift} around 0 originates from disorder configurations that result in localization, and the v_{drift} with finite velocity originates from disorder configurations where propagation is still possible.

5.E. BIORTHOGONAL EXPECTATION VALUE

In the results of the manuscript, we calculated Re(J) of the state m as $\text{Re}\left(\langle\psi_m|J|\psi_m\rangle\right)$ such that $\langle\psi_m| = |\psi_m\rangle^\dagger$. In this section we calculate Re(J) of state m as $\text{Re}\left(\langle\psi_m|J|\psi_m\rangle\right)$ such that $\langle\psi_m| = |\psi_m\rangle^{-1}$, that is to say $\langle\psi_m|$ is the m-th left eigenstate and $|\psi_m\rangle$ is the m-th right eigenstate. We refer to this $\text{Re}\left(\langle\psi_m|J|\psi_m\rangle\right)$ as the biorthogonal expectation value of Re(J). The behavior of Re(J) is significantly impacted by this change in expectation value, as shown in Fig. 5.E.1.

For the H_8 model, similarly to Fig. 5.D.1 for low disorder ($\delta = 0.01$) the distribution of Re(J) of the maximally amplified eigenstate is bimodal [Fig. 5.E.1 (a)]. At finite disorder, the distribution becomes multimodal, similar to v_{drift} [Fig. 5.D.1 (c)]. The scaling parameter at the transition of the biorthogonally projected Re(J) scales as $L^{0.44\pm0.01}$ [Fig. 5.E.1 (c)].

The Hatano-Nelson model H_{HN} also exhibits bimodal behavior [Fig. 5.E.1 (b)], similarly to the distribution of v_{drift} [Fig. 5.D.1 (d)]. Close to the transition point, the distribution of Re(J) has two peaks, with one broad peak around the low-disorder Re(J) value 1.1, and the other delta function peak around the high disorder Re(J) value 0. In the biorthogonal case, the Re(J) of the H_{HN} displays a phase transition. The scaling of the transition width is found to scale close to $\sqrt{L}$, as $L^{0.55\pm0.02}$ [Fig. 5.E.1 (d)], similarly to the

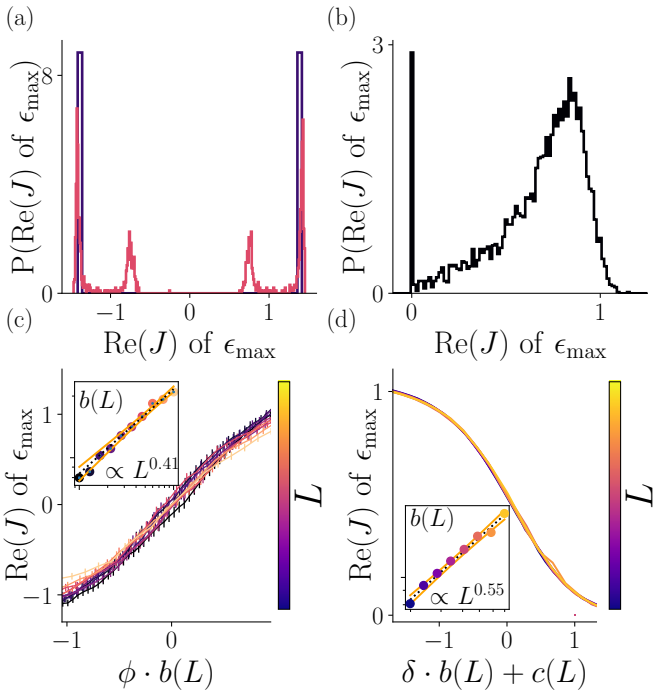

Figuur 5.E.1: Re(J) results using biorthogonal expectation values for Hamiltonians H_8 [Eq. (5.3.1)] and H_{HN} [Eq. (5.2.1)]. For the Hatano-Nelson Hamiltonian (5.2.1), random disorder terms $U_{i,j}$ with $i \in \{0,1,2\}$ and j the site number are sampled from distributions with standard deviation δ_i. We set $\delta_0 = \delta_1 = \delta_2 \equiv \delta$. For the Hamiltonian H_8 (5.3.1), random disorder terms $U_{i,j}$ with $i \in \{0,1,2,3,4\}$ and j the site number are sampled from distributions with standard deviation δ_i. We set $\delta_0 = \delta_1 = \delta_2 = \delta_3 = \delta_4 \equiv \delta$. (a) distributions of Re(J) of the maximally amplified state of the H_8 model at $\phi = 0$ and $\delta = 0.1$ and $\delta = 0.01$ in units of the bandwidth W. (b) distribution of Re(J) of the maximally amplified state of the H_{HN} model at $\delta = 0.8$. (c) Rescaled Re(J) of the maximally amplified state of the H_8 model for $\delta = 0.1$. (d) Rescaled Re(J) of the maximally amplified state of the H_{HN} model for $\delta = 0.1$. Insets of (c) and (d): scaling functions of the slope at the transition and the 95% confidence interval. Plot details in App. 5.A.

H_8 case.

The Re(J) calculated using the biorthogonal expectation value appears to follow the behavior of v_{drift} more closely, but we do not have an argument as to why this would be the case.

5.F. RESULTS IN TWO DIMENSIONS

We consider the following two-dimensional non-Hermitian model:

$$H_N = \sum_{d=1}^{N}\sum_{j}^{L_d} U_{0,j}|x_{d,j}\rangle\langle x_{d,j}| + \left(t_{x_d,+} + i\,t'_{x_d,+}U_{1,d,j}\right)|x_{d,j+1}\rangle\langle x_{d,j}| + \left(t_{x_d,-} + i\,t'_{x_d,-} + U_{2,d,j}\right)|x_{d,j}\rangle\langle x_{d,j+1}|, \tag{5.F.1}$$

Parameter	value
$t_{x,+}$	1
$t'_{x,+}$	0
$t_{x,-}$	0.8
$t'_{x,-}$	0
$t_{y,+}$	0
$t'_{y,+}$	0
$t_{y,-}$	0
$t'_{y,-}$	1

Tabel 5.2: Parameters used for simulating Hamiltonian Eq. (5.F.1).

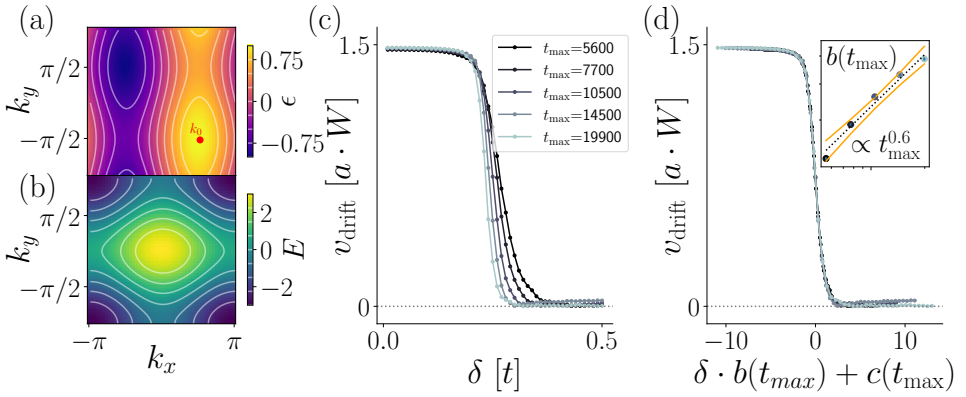

Figuur 5.F.1: Finite-time scaling of two-dimensional non-Hermitian model Eq. (5.F.1) with parameters 5.2. (a)-(b) The Brillouin zone of (a) the imaginary part of the energy ϵ and (b) the real part of the energy. (c) The unscaled localization transition of v_{drift} as a function of disorder. Random disorder terms $U_{i,d,j}$ with $i \in \{0,1,2\}$, $d \in \{x,y\}$ and j the site number (5.F.1) are sampled from distributions that all have a standard deviation of $\delta_0 = \delta_1 = \delta_2 \equiv \delta$. (d) The rescaled curves of (c). Inset: scaling of the sharpness of the transition. Plot details in App. 5.A.

where the sum runs over all the lattice sites j and the spatial dimensions d of a N-dimensional system with $L/a = \frac{1}{a}\sum_d^N L_d$ sites, with a the lattice constant. x_d corresponds to the spatial coordinate in dimension d, and $U_{n,d,j}$ are random disorder terms sampled from a distribution $\delta_{n,d}$. We choose $N = 2$.

The parameters we use in simulating this model are found in Table 5.2, and yield the spectrum shown in Fig. 5.F.1 (a)-(b). Wave packets are initialized at the center of the periodically wrapped lattice ($x_0 = [0,0]$), with a width one tenth of the width of the lattice ($\sigma = L/10$) and with the same initial velocity ($k_x = \pi/2, k_y = 0$) for all simulations.

We fit the function $a\tanh(b\delta + c)$ to the localization transition of v_{drift} as a function of δ, and extract $b(t_{\text{max}})$. $b(t_{\text{max}})$ scales as $t_{\text{max}}^{0.63\pm0.05}$ [Fig. 5.F.1 (d)], which differs from the 1D critical exponents presented in the main text [Table 5.1]. It is not possible from

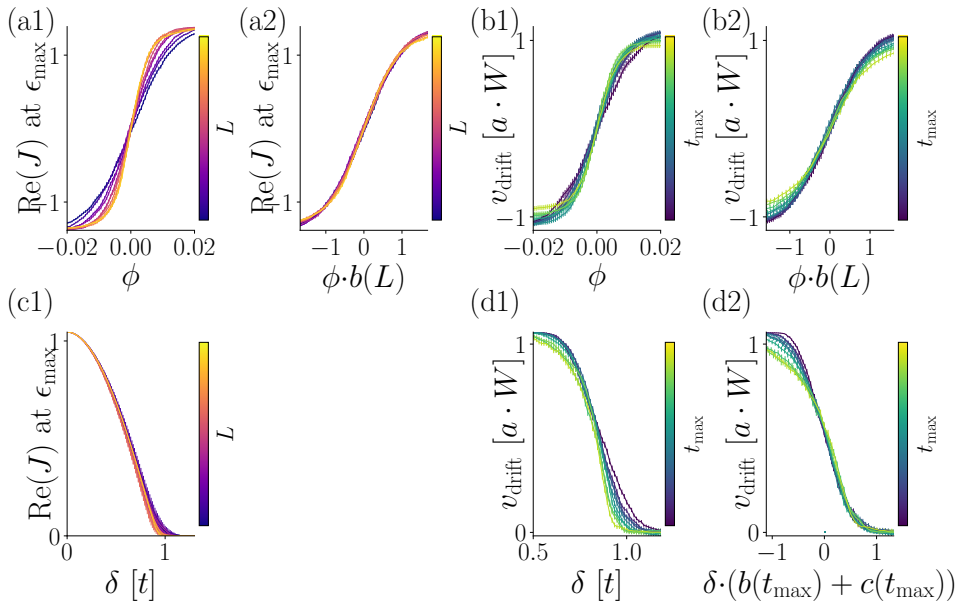

Figuur 5.G.1: Unscaled (a1,b1,c1,d1) and rescaled (a2,b2,d2) Re(J) at the point of maximal amplification $\epsilon_{\max}$ and v_{drift} at the transition point, as a function of ϕ the tilt angle of the spectrum or as a function of disorder δ. For the Hatano-Nelson Hamiltonian (5.2.1), random disorder terms $U_{i,j}$ with $i \in \{0,1,2\}$ and j the site number are sampled from distributions with standard deviation δ_i. We set $\delta_0 = \delta_1 = \delta_2 \equiv \delta$. For the Hamiltonian H_8 (5.3.1), random disorder terms $U_{i,j}$ with $i \in \{0,1,2,3,4\}$ and j the site number are sampled from distributions with standard deviation δ_i. We set $\delta_0 = \delta_1 = \delta_2 = \delta_3 = \delta_4 \equiv \delta$. (a1)-(b2) Results for the H_8 model Eq. (5.3.1) used in Fig. 5.2.1. (c1)-(d2) Results for the H_{HN} model Eq. (5.2.1) used in Fig. 5.3.1. Plot details in App. 5.A.

these results to say whether the critical exponent of non-Hermitian systems is dimension-dependent or not.

5.G. UNSCALED RESULTS

The results for Re(J) at $\epsilon_{\max}$ and v_{drift} shown in Fig. 5.2.1 and Fig. 5.3.1 are rescaled by the scaling variables b (and c in the case of v_{drift}). Fig. 5.G.1 contains the unscaled data used to obtain Fig. 5.2.1 and Fig. 5.3.1, as well as the rescaled data for comparison.

We do not show rescaling of the Re(J) at $\epsilon_{\max}$ curves of Fig. 5.G.1 (c1), since they do not exhibit scaling.

BIBLIOGRAFIE

[1] P. W. Anderson, *Absence of diffusion in certain random lattices,* Phys. Rev. **109**, 1492 (1958).

[2] F. Evers and A. D. Mirlin, *Anderson transitions,* Rev. Mod. Phys. **80**, 1355 (2008).

[3] N. Hatano and D. R. Nelson, *Localization transitions in non-hermitian quantum mechanics,* Phys. Rev. Lett. **77**, 570 (1996).

[4] P. W. Brouwer, P. G. Silvestrov, and C. W. J. Beenakker, *Theory of directed localization in one dimension,* Phys. Rev. B **56**, R4333 (1997).

[5] K. Kawabata and S. Ryu, *Nonunitary scaling theory of non-hermitian localization,* Phys. Rev. Lett. **126**, 166801 (2021).

[6] H. Spring, V. Konye, F. A. Gerritsma, I. C. Fulga, and A. R. Akhmerov, *Phase transitions of wave packet dynamics in disordered non-Hermitian systems,* (2023).

[7] K. Kawabata, M. Sato, and K. Shiozaki, *Higher-order non-hermitian skin effect,* Phys. Rev. B **102**, 205118 (2020).

[8] H. Sahoo, R. Vijay, and S. Mujumdar, *Anomalous transport regime in non-hermitian, anderson-localizing hybrid systems,* (2022).

[9] P. Zhu, X.-Q. Sun, T. L. Hughes, and G. Bahl, *Higher rank chirality and non-hermitian skin effect in a topolectrical circuit,* (2022).

[10] M. Wu, Q. Zhao, L. Kang, M. Weng, Z. Chi, R. Peng, J. Liu, D. H. Werner, Y. Meng, and J. Zhou, *Evidencing non-bloch dynamics in temporal topolectrical circuits,* (2022).

[11] Q. Lin, T. Li, L. Xiao, K. Wang, W. Yi, and P. Xue, *Observation of non-hermitian topological anderson insulator in quantum dynamics,* Nat. Commun. **13** (2022), 10.1038/s41467-022-30938-9.

[12] S. O. Peatáin, T. Dixon, P. J. Meeson, J. Williams, S. Kafanov, and Y. A. Pashkin, *The effect of parameter variations on the performance of the josephson travelling wave parametric amplifiers,* (2021).

[13] S. Weidemann, M. Kremer, S. Longhi, and A. Szameit, *Non-hermitian anderson transport,* (2020).

[14] T. Jiang, A. Fang, Z.-Q. Zhang, and C. T. Chan, *Anomalous anderson localization behavior in gain-loss balanced non-hermitian systems,* Nanophotonics **10**, 443 (2021).

[15] F. Noronha, J. A. S. Lourenço, and T. Macrì, *Robust quantum boomerang effect in non-hermitian systems,* Phys. Rev. B **106**, 104310 (2022).

[16] N. J. Higham, *Functions of Matrices: Theory and Computation* (Society for Industrial and Applied Mathematics, Philadelphia, PA, USA, 2008).

[17] M. L. Liou, *A Novel Method of Evaluating Transient Response,* Proc. IEEE **54**, 20 (1966).

[18] C. Moler and C. Van Loan, *Nineteen Dubious Ways to Compute the Exponential of a Matrix, Twenty-Five Years Later,* SIAM Rev. **45**, 3 (2003).

ACKNOWLEDGMENTS

To my supervisor Anton Akhmerov, it has been an honor and a privilege to work closely with you, and certainly I am a better researcher thanks to everything I have learned from you. Thank you to Dániel Varjas and Cosma Fulga. It was a pleasure to collaborate with you, and your help and guidance have been instrumental in all of the works included in this thesis. A big thank you to Viktor Könye, it was super nice working with you. Thank you Kostas Vilkelis for the tireless work you've done curating parallel computing in the group. Thank you to both Antonio Manesco and Mert Bozkurt for their willingness to discuss my projects and offer helpful advice. Thank you Boris Varbanov, Ivan Kulesh, Juan Torres, and Johanna Zijderveld for the coffee breaks. With commiseration and humor, you have made my PhD journey a most enjoyable one. An extra thank you to Johanna for helping to translate the summary of the thesis. To my husband Christian Prosko, you have always unconditionally supported me and inspired me to be a better person. I look forward to every day of our lives together. Obviously I can never thank you enough. I also want to thank our family for their support.